Modified Layered Titanates for Enhanced Photochemical and Photoelectrochemical Water Splitting

by

Tuğçe Üstünel

A Dissertation Submitted to the
Graduate School of Sciences and Engineering
in Partial Fulfillment of the Requirements for
the Degree of

Master of Science

in

Materials Science and Engineering

KOÇ ÜNİVERSİTESİ

September 25, 2023

Modified Layered Titanates for Enhanced Photochemical and Photoelectrochemical Water Splitting

Koç University

Graduate School of Sciences and Engineering

This is to certify that I have examined this copy of a master's thesis by

Tuğçe Üstünel

and have found that it is complete and satisfactory in all respects,

and that any and all revisions required by the final

examining committee have been made.

Committee Members:

_____

Assoc. Prof. Sarp Kaya (Advisor)

_____

Dr. Esmail Doustkhah (Co-Advisor)

_____

Assoc. Prof. Uğur Ünal

_____

Prof. Savaş Sönmezoğlu

Date: September 25, 2023

Dedicated to my mom, dad, and sis

ABSTRACT

Modified Layered Titanates for Enhanced Photochemical and Photoelectrochemical Water Splitting

Tuğçe Üstünel

Master of Science in Materials Science and Engineering

September 2023

The search for sustainable green energy sources is becoming essential due to the rising global energy demands while making use of sunlight and water as benign resources show the most potential. A notable method is the use of the energy of the sun to split water into hydrogen and oxygen. Highlighting its critical role in meeting the world's energy demands as a promising energy carrier, hydrogen, with its zero carbon emissions. Solar-driven photocatalytic and photoelectrochemical water splitting offer a compelling method to produce hydrogen and oxygen.

Exfoliation and ion exchange methods were utilized to expose active sites in layered titanates, along with modifications like loading single atoms with photoactive species. The first part of this study involved exfoliating potassium lithium layered titanates (KTLO) and photo-deposition of single atom Sn onto the layer surfaces, as Sn atoms act as co-catalysts. The exfoliation is confirmed by using X-ray diffraction (XRD), showing the expansion of interlayer spaces. Exfoliated titanate showed a distinguished photocatalytic hydrogen evolution reaction (HER) from water and ammonia borane. Adding Sn single atoms to its surface significantly increases the photocatalytic activity, causing roughly a threefold increase in exfoliated titanate. It is also demonstrated that the optimal Sn loading is required for the best HER activity. A thorough investigation demonstrated by photoluminescence spectroscopy (PL) showed that exfoliated titanate showed an improved lifetime for charge carriers.

The second part of this study focused on the photocatalytic and photoelectrochemical activities of cetyltrimethylammonium bromide (CTAB) intercalated layered cesium titanate (CsTO). Interlayer spacing served as proof of successful intercalation confirmed by the X-ray diffraction. Interlayer space expansion of CsTO results in morphological changes and a larger surface area, characterized by Scanning Electron Microscopy (SEM). Likely, the treatment with CTAB induced an ion exchange mechanism during the intercalation process, resulting in the removal of Cs^+ ions, and this phenomenon was

confirmed through X-ray Photoelectron Spectroscopy (XPS) analysis. As an n-type material, CTAB intercalated CsTO samples are promising candidates to utilize surface electrons for photocatalytic HER, and photogenerated holes are utilized for photoelectrochemical oxygen evolution reaction (OER). Carbon content between interlayers had an impact on charge carrier utilization and served as a conductive layer for photoelectrochemical OER. Consistent with the photocatalytic HER findings, the linear sweep voltammetry (LSV) experiments conducted for the OER revealed a similar trend, indicating enhanced activity with increased CTAB concentrations.

Overall, this study highlights the potential of modified layered titanate photocatalysts for effective water splitting driven by solar energy, with implications for HER and OER in the search for renewable energy sources.

ÖZETÇE

Gelişmiş Fotokimyasal ve Fotoelektrokimyasal Su Ayrıştırma için Modifiye Edilmiş Katmanlı Titanatlar

Tuğçe Üstünel

Malzeme Bilimi ve Mühendisliği, Yüksek Lisans

Eylül 2023

Artan küresel enerji talepleri nedeniyle sürdürülebilir yeşil enerji kaynakları arayışı zorunlu hale gelirken, zararsız kaynakların en fazla potansiyel gösterdiği güneş ışığı ve sudan faydalanılıyor. Dikkate değer bir yöntem, suyu hidrojen ve oksijene ayırmak için güneş enerjisinin kullanılmasıdır. Sıfır karbon emisyonuyla gelecek vaat eden bir enerji taşıyıcısı olan hidrojen olarak dünyanın enerji taleplerini karşılamadaki kritik rolünü vurguluyor. Güneş enerjisiyle çalışan fotokatalitik ve fotoelektrokimyasal su ayrıştırma, hidrojen ve oksijen üretmek için ilgi çekici bir yöntem sunuyor.

Katmanlı titanatlardaki aktif bölgeleri açığa çıkarmak için eksfoliyasyon ve iyon değiştirme yöntemlerinin yanı sıra tek atomların fotoaktif türlerle yüklenmesi gibi modifikasyonlar kullanıldı. Bu çalışmanın ilk kısmı, potasyum lityum katmanlı titanatların (KTLO) eksfoliye edilmesini ve Sn atomlarının yardımcı katalizör görevi görmesi nedeniyle tek atomlu Sn'nin katman yüzeyleri üzerinde foto-birikimini içeriyordu. Eksfoliyasyon, katmanlar arası boşlukların genişlemesini gösteren X-ışını kırınımı (XRD) kullanılarak doğrulanır. Eksfoliye edilmiş titanat, su ve amonyak borandan ayırt edici bir fotokatalitik hidrojen evrimi reaksiyonu (HER) gösterdi. Yüzeyine Sn tekli atomlarının eklenmesi, fotokatalitik aktiviteyi önemli ölçüde artırır; bu, eksfoliye edilmiş titanatta fotoaktivitenin kabaca üç kat artışına sebep olur. Ayrıca en iyi HER aktivitesi için optimal Sn yüklemesinin gerekli olduğu da gösterilmiştir. Fotolüminesans spektroskopisi (PL) ile gösterilen kapsamlı bir araştırma, ekfsoliye edilmiş titanatın yük taşıyıcıları için daha iyi bir kullanım ömrü gösterdiğini gösterdi.

Bu çalışmanın ikinci kısmı, setiltrimetilamonyum bromür (CTAB) ara katmanlı sezyum titanatın (CsTO) fotokatalitik ve fotoelektrokimyasal aktivitelerine odaklandı. Katmanlar arası aralık, X-ışını kırınımıyla doğrulanan başarılı ara katmanın kanıtı olarak kullanıldı. CsTO'nun katmanlar arası mesafenin genişlemesi, morfolojik değişikliklere ve Taramalı Elektron Mikroskobu (SEM) ile karakterize edilen daha geniş bir yüzey alanına

neden olur. Muhtemelen CTAB ile işleme, interkalasyon işlemi sırasında bir iyon değiştirme mekanizmasını tetikler, bu da Cs^+ iyonlarının yer değiştirmesiyle sonuçlandı ve bu fenomen, X-ışını Fotoelektron Spektroskopisi (XPS) analiziyle doğrulandı. N-tipi bir malzeme olarak CTAB arakatkılı CsTO numuneleri, fotokatalitik HER için yüzey elektronlarını kullanma konusunda umut verici adaylardır ve fotoelektrokimyasal oksijen evrimi reaksiyonu (OER) için fotojenere delikler kullanılır. Ara katmanlar arasındaki karbon içeriğinin yük taşıyıcı kullanımı üzerinde etkisi vardı ve fotoelektrokimyasal OER için iletken bir katman görevi görüyordu. Fotokatalitik HER bulgularıyla tutarlı olarak, OER için gerçekleştirilen doğrusal tarama voltametrisi (LSV) deneyleri, artan CTAB konsantrasyonlarıyla artan aktiviteye işaret eden benzer bir eğilim ortaya çıkardı.

Genel olarak bu çalışma, yenilenebilir enerji kaynakları arayışında HER ve OER için çıkarımlarla birlikte, güneş enerjisiyle etkili su ayrıştırma için değiştirilmiş katmanlı titanat fotokatalizörlerin potansiyelini vurgulamaktadır.

ACKNOWLEDGEMENTS

I find myself torn between happiness for the privilege of having spent these transformative years in this beautiful laboratory and the sadness of finishing this chapter of my academic journey. It is inevitable to express the depth of my gratitude for every moment I have experienced here.

First and foremost, I want to express my heartfelt thanks to my dear advisor, Assoc. Prof. Sarp Kaya. His constant support, mentorship, and guidance have been instrumental in my growth, both as a scientist and as an individual. Each step I took under his supervision has left an indelible mark on my academic path, and I am confident that the knowledge and skills I have acquired will serve as a compass in my future endeavors. I am profoundly grateful for the person I have become during these two years, and words cannot adequately convey my appreciation.

I also would like to thank the dear committee members, Assoc. Prof. Uğur Ünal and Prof. Savaş Sönmezoğlu for their invaluable time and consideration of my work.

My journey in the SarpKayaLab has been enriched by the amity and support of the group members. I extend my thanks to each one of them for always being there to lend a helping hand. Special gratitude goes to Dr. Timuçin Balkan and Saeede Tafazoli for their invaluable assistance, especially in the GC measurements. Without their support, I could not have overcome the challenges I encountered. I must also express my deep appreciation to my dear friend, Emir Ardalı, for being a constant source of companionship and support throughout my master's studies. The memories we created, both inside and outside the lab, are treasured, and the times we spent have meant so much to me. To Öykü Alagöz and Amin Mohammadpour, I offer my heartfelt thanks for their precious help and support, being cherished friendships. To everyone in the lab, I could not have embarked on this journey without you, and I hold your contributions in high regard.

My gratitude extends to my dear family, Sakine, Ahmet, and Şenay. I have always strived to be worthy of the boundless love and support they have given me throughout my life, following the path paved by my dear sister. I am proud and grateful to have them as my family, and I pledge to honor their legacy through my future endeavors continually. Thank you for being my unwavering pillars of strength. On a lighter note, I must acknowledge Leo, my sister's cat, for the quiet companionship of being there and just sitting next to me but supporting me mentally during some of the moments of this thesis writing.

TABLE OF CONTENTS

List of Figures xi

Abbreviations xiv

Chapter 1: Introduction 1

1.1 Solar Energy Conversion 1

1.2 Photochemical Water Splitting 2

1.2.1 Photocatalytic Hydrogen Evolution Reaction (HER) by Water Splitting 3

1.2.2 Photocatalytic Hydrogen Evolution Reaction (HER) by Ammonia Borane (AB) Decomposition 4

1.3 Photoelectrochemical Water Splitting 5

1.3.1 Photoelectrochemical Oxygen Evolution Reaction (OER) 6

1.4 TiO_2-Based Photocatalysts 7

1.5 Layered Titanates as Photocatalysts for HER and OER 8

Chapter 2: Experimental Methods 10

2.1 LT Photocatalyst Synthesis Processes 10

2.1.1 Solid-state Synthesis of KTLO and CsTO LT Photocatalysts 10

2.1.1.1 Ion-exchange and Exfoliation of KTLO Layered Titanates 10

2.1.2 Single Atom Sn Loading on Exfoliated LT by Photo-deposition 11

2.2 Synthesis of Heterojunction Structures with CTAB Intercalation 11

2.3 Thin Film Preparation of CTAB Intercalated Cesium Titanate 12

2.4 Photocatalytic Experimental Procedure 12

2.4.1 Photochemical Setup 12

2.4.2 Quantitative Measurement of Hydrogen by Gas Chromatography (GC) 13

2.5 Photoelectrochemical Experiments 14

2.5.1 Photoelectrochemical Setup 14

2.5.2 Electrochemical Impedance Spectroscopy (EIS) 14
2.5.3 Linear Sweep Voltammetry (LSV) 15
2.6 Structural Characterizations 15
2.6.1 X-Ray Diffraction 15
2.6.2 X-Ray Photoelectron Spectroscopy (XPS) 16
2.6.3 Raman Spectroscopy 17
2.6.4 Fourier Transform Infrared Spectroscopy (FTIR) 17
2.6.5 UV-Visible Spectroscopy 18
2.6.6 Photoluminescence Spectroscopy 18
2.6.7 Scanning Electron Microscopy (SEM) and Transmission Electron Microscopy (TEM) 19
Chapter 3: Photochemical Hydrogen Evolution Reaction by Single Atom Loaded Exfoliated Layered Titanate 21
3.1 Introduction 21
3.2 Experimental Procedure 23
3.3 Structural Characterizations 23
3.4 Results and Discussion 23
3.5 Conclusion 36
Chapter 4: Photochemical and Photoelectrochemical Activity of CTAB Intercalated Cesium Titanates 37
4.1 Introduction 37
4.2 Experimental Procedure 38
4.3 Results and Discussion 39
4.4 Conclusion 56
Chapter 5: Conclusion 57
Chapter 6: References 58
Chapter 7: Appendix 69
7.1 Appendix A: Supporting Information for Chapter 3. 69

LIST OF FIGURES

Figure 1.1. Schematic representation of photochemical water splitting via a photocatalyst. 3

Figure 1.2. Surface/bulk charge recombination mechanism during photocatalytic water splitting. 4

Figure 1.3. Graphical representation of a tandem-junction photoanode and photocathode photoelectrochemical cell for water splitting. 6

Figure 1.4. Crystal structures of TiO_2 rutile, brookite, and anatase with their crystal systems are tetragonal, orthorhombic, and tetragonal, respectively. 7

Figure 2.1. Schematic illustration of a basic gas chromatograph. 13

Figure 2.2. Randles circuit model. 15

Figure 2.3. The delay between waves scattered from adjacent lattice planes occurs when it is an integer multiple of wavelength, according to Bragg's Law. 16

Figure 2.4. Schematic representations of SEM (left) and TEM (right). 20

Figure 3.1. Representation scheme of exfoliation of KTLO and single atom Sn loading on exf-HTO. 23

Figure 3.2. Crystal structures of KTLO and HTO from the edge view (020) plane. (a) XRD patterns (b) and Raman spectra (c) of KTLO, HTO, and exf-HTO. 25

Figure 3.3. UV–vis spectra recorded in a diffuse reflectance mode (a), Tauc plot from UV–vis spectra using Kubelka–Munk conversion (b), emission spectra (c), and time-resolved PL decay profile (d) of KTLO, HTO, and exf-HTO. 26

Figure 3.4. SEM images of KTLO (a), HTO (b), exf-HTO (c, d), and TEM images of KTLO (e), HTO (f), exf-HTO with a lateral width size distribution (g), AFM image of exf-HTO with a height profile (h), HRTEM with low and high magnification (i, j), HRSTEM with a lateral view and (200) planes according to the d value (0.193 nm) (k), and cross-sectional HRTEM of exf-HTO showing layer edges and 0.715 nm thickness (l). 28

Figure 3.5. Ti 2p (a), O 1s (b), and VB (c) XPS spectra of KTLO, HTO, and exf-HTO, respectively. The alignment of the band edges based on VB edges determined by XPS and bandgap energies estimated by Tauc analysis (d). 29

Figure 3.6. SEM image (a), TEM images (b, c), electron image (d), elemental mapping of O Kα1 (e), Sn Lα1 (f), and Ti Kα1 (g) of Sn/exf-HTO. 30

Figure 3.7. XRD pattern (a), Raman spectra (b), UV-vis spectra and Tauc plots (c), steady-state PL emission and time-resolved PL decay profile (d), Ti 2p-O 1s (e), Sn 3d (f), and VB (g) XPS spectra of exf-HTO and Sn/exf-HTO. The change in the alignment of the band edges is shown in (h). 31

Figure 3.8. Solar-driven photocatalytic H_2 evolution reaction from water containing methanol on Sn/exf-HTO loaded with different concentrations of Sn (a), photocatalytic activity comparison of Sn/exf-HTO (20 ppm) with other corresponding versions of LTs and the commercial TiO_2 (P25) and Sn-loaded P25 (b). 34

Figure 3.9. Comparison of Sn/exf-HTO photocatalytic activity in AB dehydrogenation reaction under illumination and dark conditions through different Sn loading amounts (a), comparing AB dehydrogenation reaction rate of different TiO_2-based photocatalysts with exf-HTO and Sn/exf-HTO (b). 35

Figure 4.1. XRD spectra comparison of pristine cesium titanate and intercalated versions with different concentrations of CTAB (a), comparison of after carbonization samples (b), and the impact of carbonization temperature on CTAB1-CsTO and CTAB2-CsTO (c). 40

Figure 4.2. UV-Vis spectra of corresponding samples with comparisons by their CTAB concentration (a), carbonized forms with their carbonization temperature comparison (b), and their Tauc plots derived with Kubelka-Munk conversion (c) and (d), respectively. 42

Figure 4.3. Raman spectra of the corresponding samples CTAB intercalated (a) and comparison of different carbonization temperatures (b). 44

Figure 4.4. FTIR spectra comparisons indicating CTAB presence with different concentrations of CTAB (a), and thermal treatment temperature effect on CTAB intercalated samples (b). 45

Figure 4.5. Time-resolved photoluminescence emission spectra (a), (b) and lifetime decays (c) and (d) of following samples. 47

Figure 4.6. XPS spectra by comparison of pristine CsTO with CTAB intercalated and temperature effects for Ti 2p (a, b), O 1s (b, c), Cs 3d (c, d), Br 3d (g, h), N 1s (i, j), and C 1s (k, l). 49

Figure 4.7. SEM images of pristine CsTO with different magnifications (a, b, c), CTAB1-CsTO (d), CTAB1-CsTO-600 (e), CTAB1-CsTO-700 (f), CTAB2-CsTO (g), CTAB2-CsTO-600 (h), and CTAB2-CsTO-700 (i). 50

Figure 4.8. Photocatalytic activity comparison for hydrogen evolution by water splitting of CsTO and CTAB-intercalated samples (a) and after the thermal treatment at different temperatures (b). 52

Figure 4.9. LSV measurements for CTAB-CsTO samples in 0.1 M Na_2SO_4 (pH=7) solution under the front (a), (b), and back (c), (d) illumination..... 53

Figure 4.10. EIS Measurement of pristine CsTO and CTAB treated samples (a), and after heat treatment at different temperatures (b) at 1.8 VRHE in 0.1 M Na_2SO_4 at pH=7, Randle's model used, and it is shown as an inset. 54

ABBREVIATIONS

CV	Cyclic Voltammetry
FTIR	Fourier Transform Infrared
HER	Hydrogen Evolution Reaction
LT	Layered Titanate
LSV	Linear Sweep Voltammetry
UV-Vis	Ultraviolet-Visible
OER	Oxygen Evolution Reaction
PEC	Photoelectrochemical
GC	Gas Chromatography
PV	Photovoltaic
OER	Oxygen Evolution Reaction
HR-TEM	High-Resolution Transmission Electron Microscopy
XRD	X-Ray Diffraction
CTAB	Cetyltrimethylammonium bromide
ITO	Indium Tin Oxide
SEM	Scanning Electron Microscopy
TCD	Thermal Conductivity Detector
FID	Flame Ionization Detector
PL	Photoluminescence
STH	Solar to Hydrogen
EIS	Electrochemical Impedance Spectroscopy
XPS	X-Ray Photoelectron Spectroscopy

Chapter 1:
INTRODUCTION

1.1 Solar Energy Conversion

The rapidly developing energy needs in the world should be met with renewable resources and sustainable energy conversion. Searching for renewable and ecologically benign energy sources to replace conventional fossil fuels is vital, given the world's fast-rising energy demand and environmental concerns[1]. While future challenges involve the consumption of fossil fuels, which contribute to the greenhouse effect and global warming, a clean, renewable, affordable, and sustainable energy source is needed to replace fossil fuels and meet the growing energy demand. Solar energy is a promising, free, unrestricted, unpolluting, decentralized, and unending natural resource that can effectively address these issues[2]. Indeed, the most abundant renewable energy source, sunlight, can power the planet's whole population more than beyond. Thus, a sustainable and efficient method of producing renewable energy is converting solar energy to chemical energy[3], [4].

Hydrogen has been widely marked as a viable energy carrier for sustainable energy systems recently due to its lack of CO_2 emission and the benefits of not producing pollution[1]. Since it aligns with clean energy and green development, reducing toxic gas emissions, hydrogen is essential for addressing global energy crises and environmental pollution as a safe and promising alternative to fossil fuels[5]. Ultraviolet (UV) rays (λ<400 nm), visible light (400-800 nm), and infrared rays (λ>800 nm) are the three primary components of sunlight (AM1.5G). UV rays make up 4%, visible light 53%, and infrared 43% of the total solar energy. With higher wavelengths, solar light's theoretical maximum efficiency rises, reaching high quantum efficiencies (QE) at wavelengths between 400 and 800 nm. Visible light must also be captured for solar energy to be converted into hydrogen for a better solar-to-hydrogen (STH) conversion[6].

Lightweight hydrogen can be stored and transported among the alternative fuels because it has a higher gravimetric energy density of 120 kJ/g than gasoline, and when it is used in fuel cells to produce electricity, water is produced as a clean by-product[7].

Since hydrogen is a low-carbon, high-energy-density, and readily transportable energy carrier, it may be released by direct combustion or hydrogen fuel cells[8].

Given that fuels account for more than 70% of current energy usage, there is a pressing need to convert solar energy directly into fuels, particularly liquid fuels that are easy to transport and store. Splitting water into hydrogen and oxygen has long been assumed to be a method of storing solar energy[9]. If one is concerned with energy and environmental concerns about the hydrogen source in terms of production, hydrogen can be provided from water utilizing natural sources such as sunlight. Thus, solar hydrogen generation from water has been advocated, which includes a couple of approaches, such as hydroelectric power production, improvement of biomass, and photochemical or photoelectrochemical water splitting[10]. One of the most promising methods of converting solar energy into hydrogen is through solar-driven water splitting, and its technologies fall into three categories: photocatalysis, photoelectrochemical (PEC) cells, and photovoltaic-assisted electrolysis (PV-E)[3].

1.2 Photochemical Water Splitting

Considerable interest has been paid to photocatalytic overall water splitting to generate hydrogen and oxygen as a potential source of renewable energy[11]. A conventional Gibbs free energy change (ΔG^o) of 237 kJ/mol characterizes the overall water-splitting reaction as an energetically uphill and endothermic reaction[12]. The overall and half-reactions of water splitting in acidic media are shown below.

$2H_2O + 4h^+ \rightarrow O_2 + 4H^+$	(Oxygen Evolution Reaction, OER)
$4H^+ + 4e^- \rightarrow 2H_2$	(Hydrogen Evolution Reaction, HER)
$2H_2O \rightarrow 2H_2 + O_2$	(Overall Reaction, ΔG^o=237 kJ/mol)

Water splitting via a photocatalyst scheme is shown in Figure 1.1. Three main steps are typically involved in a photocatalytic water-splitting reaction to produce electrons and holes; photocatalysts must first be photoexcited. Once this has occurred, the electrons and holes produced are separated and transferred to the surface of the photocatalysts. Finally, the electrons and holes produced are captured by the reaction sites on the reduction and

oxidation co-catalysts and used in catalytic reactions for the reduction and oxidation of water[13].

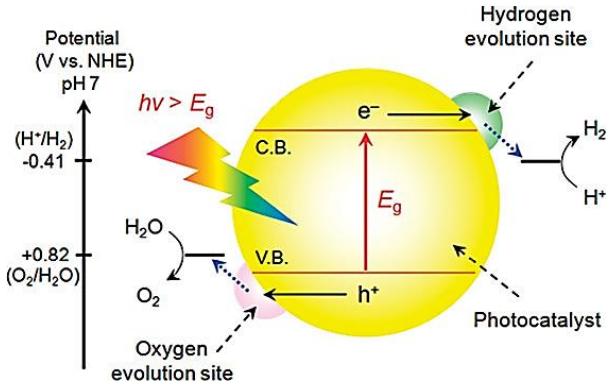

Figure 1.1. Schematic representation of photochemical water splitting via a photocatalyst[11].

A single photocatalyst can split water into hydrogen and oxygen by one-step water splitting, while a two-step excitation process is called Z-scheme and allows connecting two semiconductors with reversible redox shuttles. The Z-scheme water splitting is intended to be a similar system to natural photosynthesis. The photocatalyst reduces H^+ by electrons in the conduction band and oxidizes reductive mediators by valence-band holes, producing H_2 and oxidative mediators. Also, on the other photocatalyst side, holes oxidize water to produce O_2, while electrons return as-oxidized mediator species to a reduced state. This completes water splitting with a full cycle of redox mediators. This method provides overall water splitting on a broader range of visible light and lower Gibbs free energy changes[6], [8], [11].

1.2.1 Photocatalytic Hydrogen Evolution Reaction (HER) by Water Splitting

Hydrogen is the most basic type of solar fuel, and it can be produced from water by utilizing light absorber semiconductor photocatalysts and converting it to electrical charges, leading to surface redox reactions[14]. The photocatalytic hydrogen generation reaction mechanism consists of three main stages. First, when the semiconductor absorbs photons with higher energy than the bandgap of the semiconductor, electrons in the valence band excite to the conduction band and simultaneously generate holes in the valence band. Then, the induced electron-hole pairs separate and transfer to the surface

of the material. Those electrons in the conduction band reduce the H^+ to hydrogen while the holes oxides water into oxygen[15].

The quantity of excited electrons at the water/photocatalyst contact that can reduce water determines the overall amount of H_2 produced. The effectiveness of the photocatalytic reaction for water splitting is significantly influenced by the charge recombination and separation/migration processes that take place inside the semiconductor photocatalyst after the electron/hole pairs are formed. The number of e/h^+ couples is decreased by charge recombination by producing phonons or light emissions, which is a deactivation process that comprises both surface and bulk recombination. Therefore, efficient charge separation and fast charge carrier transport are crucial for photocatalytic hydrogen evolution by water splitting while preventing any bulk/surface charge recombination which is shown in Figure 1.2[16].

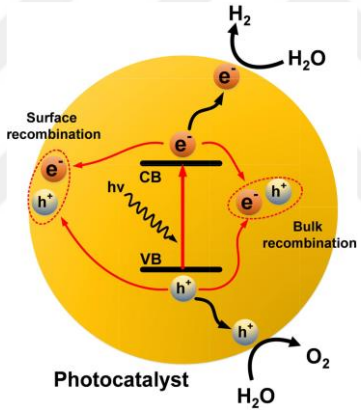

Figure 1.2. Surface/bulk charge recombination mechanism during photocatalytic water splitting [17].

1.2.2 Photocatalytic Hydrogen Evolution Reaction (HER) by Ammonia Borane (AB) Decomposition

Utilizing semiconductor photocatalysts has become a popular approach for light-driven hydrogen evolution reactions over the last decade[18]. While several molecular hydride complexes can be employed for chemical hydrogen storage, the hydrogen capacities of the materials limit their applicability. Among several materials, ammonia borane (NH_3BH_3, AB) has received special attention due to its benefits over other

materials, such as low molecular weight (30.87 g/mol), high hydrogen content (19.6 wt.%)[19], good solubility and high stability in water or aqueous phase, and non-toxic property which make ammonia borane a promising material[18]. The focus of the research has shifted to releasing hydrogen from the ammonia borane in a controlled and efficient way. So far, the methods of dehydrogenation of AB to produce hydrogen cover pyrolysis, methanolysis, and hydrolysis[20].

1.3 Photoelectrochemical Water Splitting

Photo-electrocatalysis (PEC) of water uses solar energy to efficiently provide the 1.23 V thermodynamic potential needed to split water, which is a clean and sustainable approach to manufacturing hydrogen. This is a different method of energy collecting and storing that allows solar energy to be stored as chemical energy in hydrogen[7]. High-efficiency and low-cost photoelectrochemical water splitting utilizing TiO_2 as a semiconducting material was first introduced by Fujishima and Honda in 1972. The fundamental idea of the PEC water splitting is the conversion of solar energy into hydrogen through the application of an external bias to photovoltaic materials submerged in an electrolyte that comprises a redox pair, one of which is made of a semiconductor, exposed to light, and capable of absorbing light[21].

Solar-to-hydrogen (STH) is more effective at starting the PEC water-splitting reaction, but several solar photovoltaic devices, such as solar cells, are needed to supply the necessary voltage for electrocatalytic water splitting. Also, strong photocatalytic activity for both oxygen evolution reaction (OER) and hydrogen evolution reaction cannot be achieved during PEC water splitting, but a high level of OER and HER activities can be acquired by carefully choosing PEC water splitting photocathodes and photoanodes[22].

Under photon illumination, a semiconducting electrode with the proper bandgap to match the sun spectrum produces electron-hole pairs. With an n-type semiconductor serving as the working electrode, holes at the surface of the semiconductor react with OH^- to produce O_2, while electrons are transferred to the counter electrode, where they reduce H^+ to produce hydrogen. As opposed to this, when a p-type semiconductor serves as the working electrode, hydrogen is produced, while oxygen is produced at the counter electrode. Therefore, an n-type semiconductor generates an anodic photocurrent by

transferring holes to the electrolyte, whereas a p-type semiconductor generates a cathodic photocurrent by transferring electrons to the electrolyte[23].

An experimental demonstration by Yoneyama et al. in 1975 showed that a p-GaP/n-TiO_2 tandem combination could produce hydrogen and oxygen without using an outside bias. In 1976, Nozik demonstrated that a tandem-junction architecture with a p-type photocathode and an n-type photoanode might outperform a single photoelectrode in terms of STH conversion efficiency[24]. The graphical representation of a tandem photoelectrochemical cell is shown in Figure 1.2.

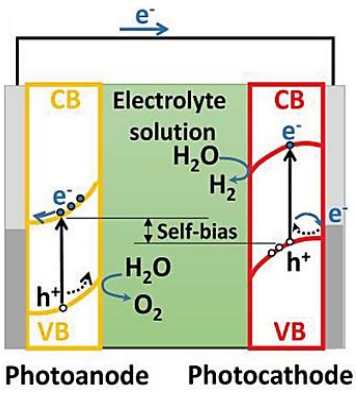

Figure 1.3. Graphical representation of a tandem-junction photoanode and photocathode photoelectrochemical cell for water splitting[25].

1.3.1 Photoelectrochemical Oxygen Evolution Reaction (OER)

Considering the oxygen atom in water is bonded to protons, the generation of oxygen gas from water oxidation requires both proton removal and electron donation. The reaction mechanism of the oxygen evolution reaction is substantially more complex than the reaction mechanism of the hydrogen evolution reaction due to the rearrangement of two oxygen atoms from two water molecules and the multiple electron contributions necessary for the oxidation of water[26].

It is thought that decorating OER catalysts is a potential way to increase charge utilization efficiency for the difficult surface charge utilization process. An appropriate PEC catalyst is crucial for increasing the oxygen evolution reaction and reducing the overpotential. Moreover, oxygen evolution reaction catalysts are capable of effectively

accelerating photogenerated hole transfer, bringing active sites, overcoming photo-corrosion, and all of which enhance water oxidation activity. Up till now, practically all photoanode investigations have utilized one or more OER catalysts to enhance the catalytic activity, which is critical in establishing the PEC conversion efficiency for water oxidation[27], [28].

1.4 TiO_2-Based Photocatalysts

For the use of photocatalysts in solar water splitting, semiconductor materials with superior chemical, physical, and electrical properties have been thoroughly studied[29]. The maintenance of electron-hole separation and the prevention of backward reactions are challenging tasks for photocatalytic water splitting. For a photocatalyst, processes of electron-hole production and separation are influenced by crystallinity and surface characteristics; moreover, lifetime and mobility are increased with fewer surface defects[30].

One of the first materials identified as a photochemical water-splitting catalyst was TiO_2, also known as P25, commercially. Rutile, anatase, and brookite are the three structural types it forms as crystalline. The band gap for the rutile phase is 3.0 eV, and for the anatase phase is 3.15 eV, and it varied slightly because all modifications contain TiO_6 octahedra that are joined by two (rutile), three (brookite), or four (anatase) joint edges and shared corners[16].

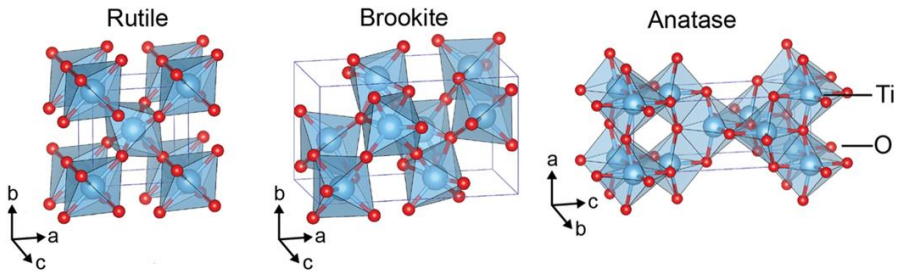

Figure 1.4. Crystal structures of TiO_2 rutile, brookite, and anatase with their crystal systems are tetragonal, orthorhombic, and tetragonal, respectively[31].

The photocatalytic effectiveness of TiO_2 is influenced by morphology and microstructure. Photochemical performance has been enhanced by developments in surface modification, structure optimization, doping, and composite fabrication.

Performance optimization requires a thorough understanding of structure-property linkages, light-matter interactions, and photocatalyst-pollutant interactions. For the purpose of comprehending the process and providing experimental directions for the synthesis of high-performance photocatalysts, accurate characterization of crystal and electronic structures is crucial[32].

1.5 Layered Titanates as Photocatalysts for HER and OER

Layered materials and intercalated compounds of them have been thoroughly studied from both fundamental scientific viewpoints on the synthesis, structure, composition, and characterization as well as from the views of their practical applications in the fields of environment, energy, electronics, and photonics[33]. Layered titanates, which are composed of infinite double layers of edge-shared TiO_6 octahedral accommodating exchangeable alkali cations and water molecules in the interlayer space, can also be thought of as clay-related inorganic solids[34]. They are getting the greatest attention because they frequently show intriguing photocatalytic characteristics. Under UV irradiation, layered titanates have demonstrated promising performance in which overall water splitting into hydrogen and oxygen is accomplished[35].

Due to their crystal structure, layered metal oxides are potential candidates for water-splitting reactions because they have unique charge separation sites. These layered materials have counter-ion layers and stacks of charged sheets that serve as water reduction and oxidation sites. Alkali metal titanate compounds, such as $K_2Ti_4O_9$, are known for their ability to exfoliate into single-phase titanate nanosheets, which makes them excellent for overall water-splitting photocatalysts or sacrificial hydrogen and oxygen evolution reactions[36].

On the other hand, the utilization of layered titanates and their nanosheet structures are some of the most promising candidates for photocatalytic water splitting, in particular, hydrogen evolution reaction[37]. For material performance and new purposes, hybridization with guest species and the creation of layered alkali titanates have been thoroughly studied. Through intercalation, exfoliation, and restacking, the functionalization of these titanates that have been transformed into protonated forms has been investigated. By using organo-ammonium ions or dilute acidic solutions to exfoliate layered alkali titanates, which create a layer-by-layer assembly structure, titanate

nanosheets can be created[38]. Thus, layered alkali metal titanates, which are a class of layered materials and semiconductors at the same time with their tunable properties, have the ability to ion-exchange and exfoliate [39]. Those properties and crystal structures of layered titanates make them promising candidates for a wide range of applications.

The experimental methods used in the synthesis of materials, structural characterizations and photocatalytic tests methods were explained in Chapter 2.

Chapter 3 focused on the examination of single-atom Sn-loaded exfoliated titanates through structural and photochemical characterizations. This investigation aimed to understand their performance in the hydrogen evolution reaction.

In Chapter 4, cesium layered titanate intercalated with CTAB was studied. Their performance in the photocatalytic HER and photoelectrochemical OER were investigated.

Chapter 2:
EXPERIMENTAL METHODS

2.1 LT Photocatalyst Synthesis Processes

2.1.1 Solid-State Synthesis of KTLO and CsTO LT Photocatalysts

Layered potassium lithium titanate, $K_{0.8}Ti_{1.73}Li_{0.27}O_4$, (abbreviated as KTLO) was prepared by solid-state reaction method using a molar ratio of TiO_2, K_2CO_3, and Li_2CO_3, 4.1:6.0:0.7, respectively. The starting chemicals and three drops of ethanol were ground in an agate mortar with a pestle for two hours, and the powder mixture was calcined in a muffle furnace at 600°C for 20 h. After the first calcination, the mixture was cooled to room temperature. The sample was mixed for another two hours and placed in the muffle furnace for the second calcination at 600 °C for 20 h.

Layered cesium titanate (donated as CsTO hereafter) was also synthesized with a similar method using a solid-state reaction. The starting materials of TiO_2 and Cs_2CO_3, with a molar ratio of 3:1, were ground in the agate mortar for one hour, and it was calcined in a muffle furnace at 800ºC for 20h.

2.1.1.1 Ion-exchange and Exfoliation of KTLO Layered Titanates

The obtained KTLO (0.5 g) from the previous step was dispersed in 0.1 M HCl solution (100 mL) and stirred at room temperature. For the protonated layered titanate (HTO), the solution was stirred for one day at 600 rpm and separated by centrifuge, washed three times with ethanol (30 mL), and dried at room temperature. For the exf-HTO (exfoliated layered titanate), the dispersion was stirred at a lower speed (400 rpm) for three days, and then, the supernatant was separated by centrifugation, and a fresh solution of 0.1 M HCl (100 mL) was added to the centrifuged powder and stirred again under the same conditions at room temperature for 11 days. Afterward, the dispersion was centrifuged and dried in a freeze-dryer for 24 h. The purpose of using a freeze-dryer is to keep the exfoliated layers in an assembly form and prevent restacking the layers during the drying process.

2.1.2 Single Atom Sn Loading on Exfoliated LT by Photo-deposition

Over the past ten years, single-atom catalysis has emerged as a leader in electrocatalysis, heterogeneous catalysis, and, most recently, photocatalysis. In photocatalytic reactions, illumination produces excited mobile charge carriers in a semiconductor. These charge carriers subsequently move to the semiconductor surface and interact with redox species that are already present in the surrounding environment. Undoubtedly, the surface-to-volume ratio is highest in a single-atom condition; moreover, single atoms can allow for both exceptional reactivity and novel reaction routes[40].

In the photochemical process of photo-deposition of earth-abundant co-catalysts, semiconductor photocatalysts are illuminated by light to produce charge carriers. When these charge carriers interact with the precursors, earth-abundant co-catalysts are created and deposited on the semiconductor surface. There are two classes for deposition by illumination: oxidative photo-deposition using photoinduced holes, such as photo-deposition of transition metals, and reductive photo-deposition using photogenerated electrons, such as photo-deposition of cobalt or nickel[41].

In this study, adsorption of Sn on exf-HTO was done by adding 10 mg of exf-HTO to the different concentrations (5, 10, 15, 20, 40, 50, 60 ppm) of 20 mL $SnCl_2.2H2O$ solution in a test tube and mixing the solution in the dark for three hours and then under the illumination of a solar simulator for one hour. As the exfoliated layers have a negative charge (compensated with H^+), cationic species can bind the layers via the electrostatic self-assembly process. The mixture was centrifuged and dried in a vacuum oven for 24 h. After the photocatalytic performance tests were done, Sn/exf-HTO was recycled via centrifugation and drying in the vacuum oven for 24 h as the resulting Sn/exf-HTO-rec sample.

2.2 Synthesis of Heterojunction Structures with CTAB Intercalation

The as-prepared cesium titanate was mentioned in section 2.1.1. was treated in cetyltrimethylammonium bromide (CTAB) solution, which is prepared in different concentrations as 0.2 M and 0.25 M. 1 g of CsTO was added to the CTAB solution separately and treated on a stirrer at 800 rpm for three days, then centrifuged at 2000 rpm by following washing with distilled water and the precipitate was dried in a vacuum oven at room temperature. Intercalated samples are named according to their CTAB

concentrations, such as CTAB1-CsTO for 0.2 M CTAB solution treatment with CsTO, CTAB2-CsTO for 0.25 M CTAB solution treatment with CsTO.

Thermal treatment in an inert atmosphere with nitrogen gas flow was used for the carbonization process. Prepared samples of CTAB intercalated CsTO were treated at 600ºC for 5 hours (with the rate 2ºC/min) under continuous N_2 flow in a quartz tube using quartz wool for a homogeneous treatment. After thermal treatment, samples were named with their temperatures, such as CTAB1-CsTO-600, for the treatment of CTAB1-CsTO sample at 600ºC.

2.3 Thin Film Preparation of CTAB Intercalated Cesium Titanate

6 mg of prepared intercalated powder samples of CsTO were dispersed in 5 mL of methanol solution in an ultrasonic bath for 25 minutes. Solutions were coated on the pre-heated indium tin oxide (ITO) surface by the drop-casting method. Coated ITO thin film samples were left on a heater at 50ºC to dry for 10 minutes.

2.4 Photocatalytic Experimental Procedure

2.4.1 Photochemical Setup

Photocatalytic activity measurements were performed using an LCS-100 solar simulator with 1.0 Sun AM 1.5G output from a 100 W xenon lamp.

For performing the photocatalytic hydrogen production reaction from ammonia borane, powder samples of KTLO, HTO, exf-HTO, and Sn/exf-HTO were dispersed in 4.5 mL of distilled water in a Pyrex test tube purged with N_2 for 30 min. Before sealing with a rubber septum properly, 0.5 mL of 40 mM NH_3BH_3 was added.

For the H_2 evolution reaction from water, powder samples (5 mg) were dispersed separately in 5 mL of distilled water (20% V/V methanol) in a Pyrex test tube which was sealed properly and purged with N_2 for 30 min. The test tube was illuminated via the solar simulator while stirring constantly. The amount of hydrogen produced was measured with the gas chromatograph, directly taking injections from the headspace of the Pyrex tube using a gastight syringe.

Photocatalytic hydrogen evolution reaction tests from water by using CTAB-CsTO catalysts were done by dispersing 20 mg of catalyst in 15 mL of distilled water (20% V/V

methanol as a hole scavenger) in a Pyrex test tube with a side-cooling jacket was sealed and connected to the GC directly to prevent any leakage of hydrogen gas. The test tube was illuminated via the solar simulator with a 300 W Xenon lamp at a 10 cm distance while stirring constantly. The amount of produced hydrogen was measured with the GC.

2.4.2 Quantitative Measurement of Hydrogen by Gas Chromatography (GC)

The quantification of hydrogen was done by a gas chromatograph (7820A, GC-System, Agilent) equipped with a thermal conductivity detector (TCD) and flame ionization detector (FID) with nitrogen as the carrier gas.

The gas chromatography (GC) technique is used to identify and quantify the components in a mixture that has different compounds. The general working principle of a GC consists of the sample's flow through the column as the different components separate from each other according to the interaction with the stationary phase[42]. The data output of GC is called a chromatogram, which plots retention time on the x-axis and detector response on the y-axis.

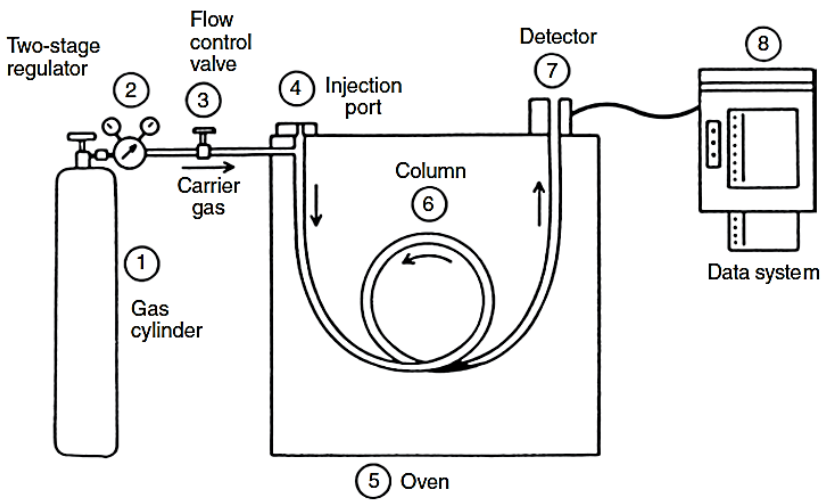

Figure 2.1. Schematic illustration of a basic gas chromatograph[42].

The thermal conductivity detector determines the difference between the thermal conductivity of the compounds and the carrier gas caused by the presence of the eluted substances[43]. The sensing element in a conventional TCD is either a heated metal wire or a thermistor, and the carrier gas passes through a heated cavity that houses it. The heat loss from the sensor when a carrier gas is flowing through the cavity depends on both the

thermal conductivity of the carrier gas and the temperature difference between the sensor and cavity. The thermal conductivity of the carrier gas mixture changes as sample vapor-containing carrier gas enters the cavity, changing the sensor temperature[44].

To be able to calculate the amount of hydrogen that is produced, calibration measurements were done. Certain percentages of hydrogen gas mixed with argon gas from 0% to 20% and sent directly to the GC. Peak areas for hydrogen were calculated, and a calibration curve was created according to those data. All the calculations for the produced amount of hydrogen were determined accordingly.

2.5 Photoelectrochemical Experiments

2.5.1 Photoelectrochemical Setup

PEC experiments were performed using an LCS-100 solar simulator with 1.0 Sun AM 1.5G output from a 100 W xenon lamp and an electrochemical quartz cell. The three-electrode system was used, including the working electrode, the counter electrode (platinum wire), and the reference electrode (silver/silver chloride, Ag/AgCl). A potentiostat (Biologic VPS300 and SP150) was used to conduct the photoelectrochemical performance tests. The Nernst equation was used to convert the potential to a reversible hydrogen electrode (RHE)[45]:

$$V_{RHE} = V_{Ag/AgCl} + 0.0592 \times pH + V^{o}_{Ag/AgCl} \qquad \text{Equation 2.1.}$$

2.5.2 Electrochemical Impedance Spectroscopy (EIS)

It is now well known that electrochemical impedance spectroscopy (EIS) is a potent tool for examining the mechanisms of electrochemical reactions, measuring the dielectric and transport properties of materials, learning more about the characteristics of electrodes, and analyzing passive surfaces[46]. EIS is a useful technique for examining the microstructure, characteristics, and chemical reaction mechanism of materials. It involves applying a small amplitude sinusoidal potential or current perturbation signal to the system, accepting the resulting response signal, and then converting it into an impedance spectrogram. By translating the internal dynamics and interfacial data of the sample into equivalent circuits and using the equivalent impedance parameters of the equivalent

circuits, EIS is able to assess the response rules and characteristics of the sample under alternating current (AC) electrical signals[47].

It is necessary to use an analogous circuit model, whose selection is based on the properties of the material and the mechanism of the reaction, in order to fully understand the material's electrochemical behavior. When using EIS, the traditional Randles model, R_s+Q_2/R_{ct}, is currently the most used which is shown in Figure 2.2. Impedance can be plotted as its imaginary and real parts, which is shown as the Nyquist plot. R_s is the resistance of the electrolyte; Q is the constant phase element (CPE) that corresponds to the capacitance between the electrolyte and the electrode; R_{ct} is the charge transfer resistance.

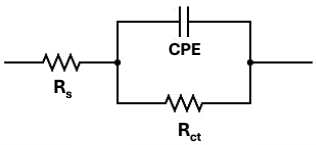

Figure 2.2. Randles circuit model.

2.5.3 Linear Sweep Voltammetry (LSV)

During a linear sweep voltammetry (LSV) scan, the electrode potential is changed continuously while the resulting current is monitored[48]. The experimental setup used is the same as other electrochemical techniques. Three-electrode system is used; the working electrode’s potential is adjusted in relation to a reference electrode, such as a saturated calomel electrode (SCE) or silver/silver chloride (AgCl).

2.6 Structural Characterizations

2.6.1 X-Ray Diffraction

A potent nondestructive method for characterizing crystalline materials is X-ray diffraction (XRD). It offers details on crystal texture, optimum orientations for crystals, and other structural factors like average grain size, crystallinity, and crystal defects. It also helps to understand the details of structures and phases[49]. The monochromatic electromagnetic waves that make up the X-ray photons can be thought of as random events that radiate outward in a spherical array from their point source. A high-voltage

generator, an X-ray source, a beam collimating system, and a detecting and recording system are all components of commercial X-ray diffraction equipment[50].

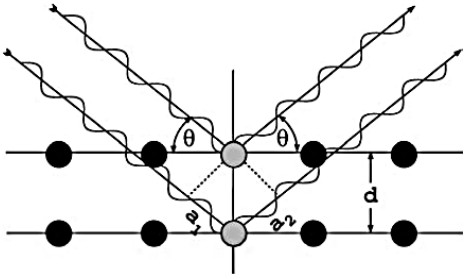

Figure 2.3. The delay between waves scattered from adjacent lattice planes occurs when it is an integer multiple of wavelength, according to Bragg's Law[51].

In the Bragg equation, $n\lambda = 2d \sin \theta$, which represents n as an integer number, theta (θ) shows the angle between the lattice planes, and d is the distance between the planes. When the wavelet scattered off the lower plane has a route that is a certain number of wavelengths longer than the one at the higher plane, Bragg reflection results[51]. In this study, XRD measurements were carried out by an X-ray diffractometer (Bruker D2 Phaser X-ray Diffractometer) with Cu Kα radiation with a 10 kV beam voltage and a 30 mA current.

XRD technique was employed to determine the crystalline structure and phase identifications of the layered titanates. It was also used to investigate the exfoliation and intercalation processes with interlayer distances of layered titanates by using Bragg’s law.

2.6.2 X-Ray Photoelectron Spectroscopy (XPS)

In fact, the X-ray photoelectron spectroscopy technique has a long history that can be traced to contemporary measurements in which either X-rays or gamma rays were used to excite photoelectrons from solids[52]. The two key features that make this technique effective as an analytical method are its surface sensitivity and its capacity to reveal chemical state information from the elements in the sample. All elements, with the exception of hydrogen and helium, can be detected by XPS, which is a surface-sensitive analytical technique in which X-ray bombard the surface of a material, and the kinetic energy of the emitted electrons is measured[53]. In this work, XPS measurements were

conducted using a Thermo K-alpha spectrometer system with Al Kα radiation (hυ = 1486.7 eV) as the excitation source. Binding energies for the XPS spectra were corrected by setting C 1s binding energy to 284.5 eV.

2.6.3 Raman Spectroscopy

Raman spectroscopy is an effective technique for characterizing materials since the information can be collected is rich from a Raman spectrum, the ability to obtain spectra for opaque solids, and the development of micro-Raman techniques that enable the characterization of small amounts or regions of the material[54]. Raman scattering involves a change in photon frequency, unlike absorption spectroscopy. Because of first-order elastic interactions with electrons, phonons, and impurities, the majority of the light that strikes the surface of a semiconductor is reflected, transmitted, absorbed, or scattered Rayleigh [55]. There are two forms of light scattering that occur when a molecule is exposed to monochromatic light: inelastic and elastic. A photon's frequency, wavelength, or energy are unaffected by elastic scattering, nor are any of these. The other, inelastic scattering, causes a change in photon frequency as a result of activating or deactivating molecular vibrations, and the photon may either gain or lose energy in the process[56]. In the study, Raman spectroscopy measurements were done by using Renishaw in Via Raman Microscope with the 633 nm excitation laser source.

In this study, Raman measurements were conducted to determine bond vibration or stretching modes through Raman scattering in the layered titanates interlayer or surface structure. It is also used to determine changes in vibrational modes of Ti-O or Cs-O.

2.6.4 Fourier Transform Infrared Spectroscopy (FTIR)

Fourier Transform Infrared (FTIR) spectroscopy examines the vibrations of molecules, and functional groups can be connected to distinctive infrared absorption bands that correspond to their internal fundamental vibrations. If the molecule's dipole moment changes as it is vibrating, a normal mode of vibration is infrared active (that is, it absorbs the incident infrared light). As a result, infrared typically cannot detect symmetric vibrations. All vibrations that are symmetrical with regard to a molecule's center of symmetry are specifically inactive in the infrared when the molecule has a center of symmetry. On the other hand, all molecules' asymmetric vibrations can be

observed[57]. A Thermofisher Scientific Nicolet iS10 FTIR Spectrometer was used in this study.

FTIR measurements were used to determine functional groups of CTAB molecule bending or stretching vibrations, such as C-H stretching modes, to investigate CTAB presence in the structure before and after the thermal treatments.

2.6.5 UV-Visible Spectroscopy

A quick analytical method for determining light's absorbance or transmittance is Ultraviolet (UV) visible spectroscopy. The practical range for UV-vis spectroscopy ranges from 200-800 nm; infrared is beyond 800 nm, while vacuum UV is below 200 nm. Transmission is the process by which light travels through media, reflects off both transparent and opaque surfaces, and is bent by crystals. In UV-vis spectrophotometers, a light source is directed through the sample, and a detector on the other side captures the light that is transmitted. Data graphs exhibit wavelength in nanometers (nm) on the x-axis and absorbance on the y-axis[58]. For the work in this study, UV–visible spectroscopy measurements were performed using a Shimadzu UV-3600 UV–vis-NIR spectrophotometer with the reflection mode. It was converted to the absorption spectra by Kubelka–Munk transformation.

In this study, UV-Vis spectroscopy measurements were conducted to determine how exfoliation or intercalation affects the light absorption processes of layered titanates. It was also used to estimate the optical bandgap energies of layered titanate before and after those modifications since it investigates electronic transitions between the valence band and the conduction band.

2.6.6 Photoluminescence Spectroscopy

The radiation that is released from an excited state to its ground state by absorbing light energy is known as photoluminescence (PL). It has been used to describe the energetic states and structural traits of surface-active sites in heterogeneous catalysts for adsorption, catalysis, and photocatalysis[59]. PL is an effective method for the investigation and characterization of materials and the dynamical processes taking place in the material. No single characterization method can thoroughly characterize all of a semiconductor's important features, although they are all valuable in determining certain

aspects relating to the material. In this respect, PL is valuable for assessing, among other things, optical emission efficiencies, material composition, impurity content, layer thicknesses, and quantum well thicknesses[60]. In this study, photoluminescence emission and lifetime measurements were performed using an Edinburgh Instruments FLS1000 spectrometer.

Time-resolved photoluminescence measurements were used to identify surface, interface, and impurity levels through emission spectrum features. Time-resolved photoluminescence decay measurements were employed to determine lifetimes in layered titanates and study radiative recombination at the bandgap edge.

2.6.7 Scanning Electron Microscopy (SEM) and Transmission Electron Microscopy (TEM)

In order to assess the structural characteristics and homogeneity of catalytic materials, scanning electron microscopy (SEM) examines their shape, texture, particle size, bulk elemental content, and uniformity at the micron scale. It is constructive for examining nanoparticle surface facets. By revealing bulk structural information using transmission electron microscopy (TEM), environmental characterization under catalytically relevant circumstances is made possible. With outstanding atomic number contrast and extremely high spatial resolution, high-pressure transmission electron microscopy (HAADF) imaging in AC-STEM is a potent characterization tool. The analysis of beam-sensitive samples has advanced, and HAADF imaging of catalysts in liquid or gaseous environments is discussed[61].

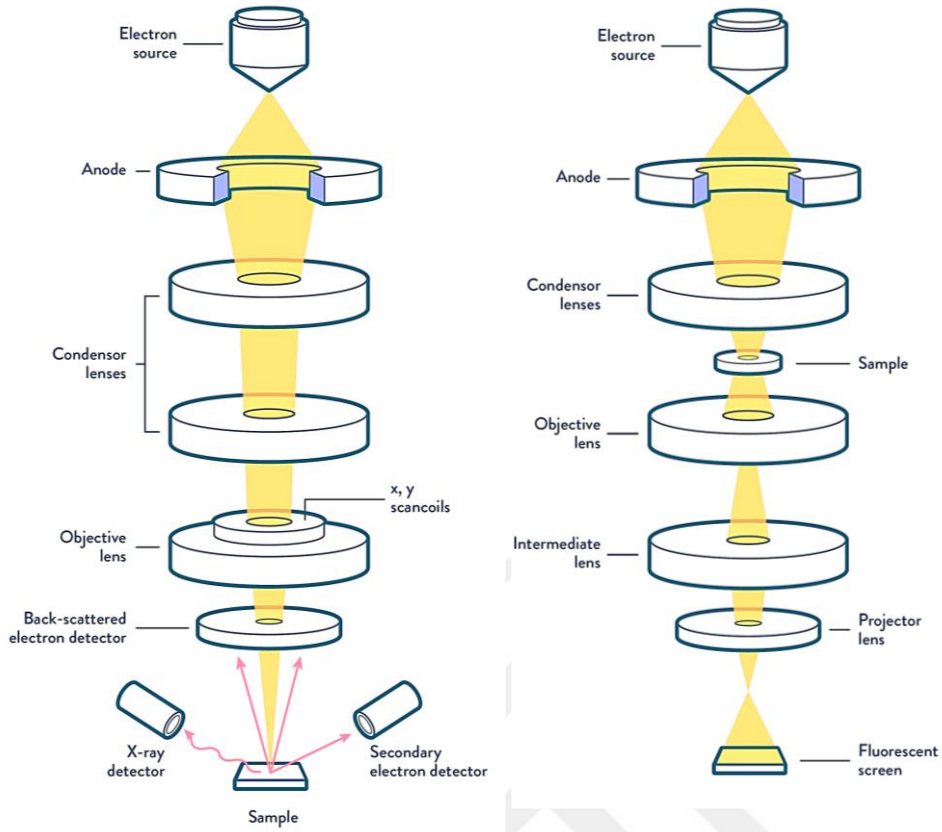

Figure 2.4. Schematic representations of SEM (left) and TEM (right)[62].

The TEM technique substitutes electrons for light and glass lenses for electron-magnetic ones. With a tiny aperture to keep out electrons traveling at large angles, a condenser lens concentrates the electrons into a uniform beam. Depending on the sample's thickness and transparency, the beam diffracts as it passes through it at normal incidence. The transmitted beams are brought into focus by the objective lens to create an image, which is then enlarged by the projector and intermediate lenses and projected onto a phosphor screen or an electron camera. By letting through only a portion of the transmitted or diffracted rays, the image contrast can be improved. By concentrating beams in the same direction onto the back focal plane of the objective lens, the electron diffraction pattern is produced[63].

Chapter 3:

PHOTOCHEMICAL HYDROGEN EVOLUTION REACTION BY SINGLE ATOM LOADED EXFOLIATED LAYERED TITANATE

3.1 Introduction

Replacing fossil fuels with green hydrogen (H_2) has been accelerated in the current decade as one of the indispensable decarbonizing alternatives to mitigate CO_2 emissions and harness climate change and its further consequences[64]. After photocatalytic water splitting[65], dehydrogenation of small molecules by photocatalysis has become one of the key approaches for green, sustainable H_2 production[66], [67]. The borane compounds (as a high-content H_2 reservoir)[68]–[71] are unique candidates for H_2 generation through a proper (photo)catalyst. Among the (photo)catalysts, layered materials are front liners in the catalysis toward H_2 production[72] due to their large theoretical surface area[73] and their game-changing chemistry (such as functional groups) and physics (such as electron-phonon interactions)[74], originating from their anisotropic structures[71], [75]. However, layered materials are usually in 3D bulk structures and need to be exfoliated since, in the pristine bulk form, the layers are stacked through weak interactions, and the interlayers are inactive[75].

Layered titanates (LTs) are of the most widely investigated layered materials as photocatalysts,[76]–[80] but scarcely show promising photocatalytic activity in H_2 generation applications under solar light irradiation due to their intrinsically large bandgaps in addition to the blockade of interlayers for any mass diffusion[78], [81]. Therefore, exfoliating the bulk crystal structure of LTs is found to be an applicable method to release the surface of the layers and further modifying with methods such as heterostructing[82]–[85] or doping[79], and single atom loading with a photoactive species to narrow the bandgap is inevitable for photocatalytic applications.

LTs consisting of TiO_6-interconnected layers can be found in different chemical compositions in which there is a strong electrostatic interaction among the layers. These LTs usually accompany alkali metal counterion and, consequently, distinctly differ in their features and activities[80], but their large bandgaps are a feature in common[77], [79]. However, exchanging these alkali metals with other species can generate a

significant change in the physicochemical activity of LTs[86]–[90]. Therefore, the investigations of the photocatalytic activities of cation-exchanged LTs may bring serendipity features that require to be undertaken.

The pioneering works around the exfoliation of LTs were first established by Sasaki et al. with organic ammoniums, where they reported the osmotic swelling and subsequent exfoliation[91]. Since then, some efforts have been made to modify the exfoliating method, including those without organic exfoliating agents. However, the structural conversion of LTs into a more stable phase (*e.g.*, rutile or anatase) under mild or strict conditions has been reported[92], [93]. Thus, the major challenge of LTs is their (simultaneous) exfoliation without crystal phase change and without using an organic agent[94]. Also, in a few successful cases, LTs have been exfoliated by some organic species such as alkylammonium salts; the intercalation of such species in the interlayers of LTs[95] causes exfoliation or a partial phase conversion[94] and, thus, makes the LTs impure or costly[79], [94], [95]. For this reason, the optical features, precisely the photocatalytic properties, of the exfoliated pure LTs are still underexplored.

Nowadays, loading a single atom on semiconductors plays an important role in improving photocatalytic activity[96], [97]. However, in the case of the LTs, single-atom loading can barely be found. One of the critical challenges in single-atom catalysis is to stabilize the chemical state of the single atom on a semiconductor through the adjacent heteroatoms. Moreover, the single-atom oxidation state alteration is another challenge that is drastically impacted by the crystal structure and chemical composition of the surface of the semiconductor[98]–[100].

Herein, we investigate the exfoliation of LT in dilute HCl water without any organic species and the roles of Sn^{2+} loading on the exfoliated LT nanostructures (exf-HTO) in photocatalytic ammonia borane (AB) dehydrogenation and hydrogen evolution reaction (HER) from water at room temperature. We demonstrate the single atom Sn-loaded exf-HTO (Sn/exf-HTO), in an optimal ratio, shows considerably higher photocatalytic activity than conventional TiO_2 photocatalysts, including P25 and Au nanoparticle-loaded P25.

3.2 *Experimental Procedure*

Potassium lithium layered titanates were synthesized as described in Section 2.1.1. The exfoliation of KTLO and single atom Sn loading on the exfoliated titanate procedure was described in Sections 2.1.1.1. and 2.1.2. To carry out the experiments, the setup used for photocatalytic activity tests was explained in Section 2.4.

3.3 *Structural Characterizations*

Structural characterizations of samples were explained in Section 2.6.

3.4 *Results and Discussion*

Usually, the protonation, cation exchange, and exfoliation of LTs are three crucial types of post-modifications that can be found around developing LTs for various applications. Here, we present a new facile method for the exfoliation of LTs along protonation through long-term slow agitation of LT in a dilute HCl solution into a few-layered HTO. A step further, it is succeeded in loading a single atom Sn and, subsequently, a schematic procedure for preparation of the single atom Sn-loaded exf-HTO is presented in Figure 3.1 and Figure 3.2a.

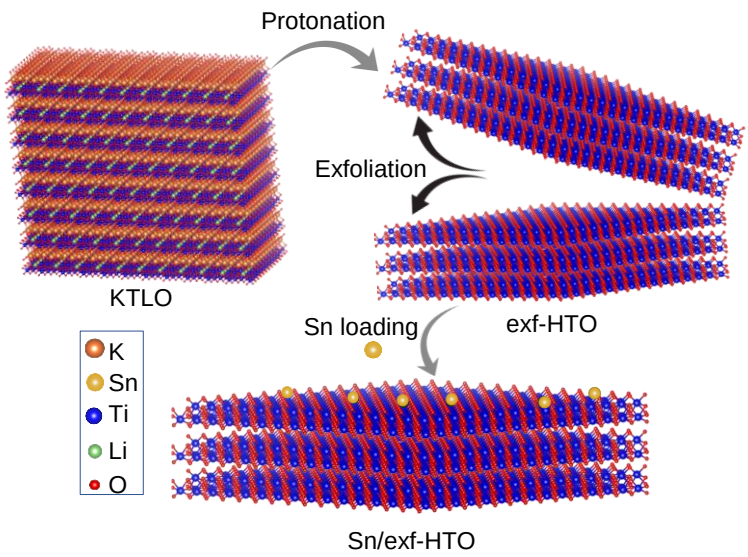

Figure 3.1. Representation scheme of exfoliation of KTLO and single atom Sn loading on exf-HTO.

The successful synthesis of layered titanate KTLO through the XRD pattern and used it for further protonation (HTO) and exfoliation (exf-HTO) was confirmed. In the case of KTLO, a peak at 11.4° corresponds to the (020) plane with a d value of ~0.8 nm, representing the interlayer space and the layer thickness (Figure 3.2a). A peak at 2θ = 29.1° also corresponds to the layered structure of the material, showing the (130) plane. Another characteristic peak at 47.4° corresponds to the crystalline lepidocrocite structure of layered titanate, showing the (200) plane. Once protonated, the first peak at a lower degree slightly shifts to a smaller angle (9.7° corresponds to a d value of ~ 0.9 nm), showing that the interlayer space has been expanded, for example, by intercalating water after exchanging the K^+ and Li^+ with H^+, so that around the d value undergoes 0.1 nm expansion with respect to KTLO (Figure 3.2b). As confirmed before[90], the protonated LT usually exhibits broader peaks compared to the pristine KTLO. Once the exfoliation is performed, the first characteristic peak of the layered structure has slightly shifted to higher angles with a significant decrease in the intensity compared to those for HTO and KTLO and has become broader, showing that the layers are remarkably exfoliated (Figure 3.2b). The peak at 29.1° after the treatment is also broadened, showing that the protonation and further exfoliation make the layers' assembly disorder (exfoliated) with less long-range order to be detectable by XRD as a sharp peak (this justification will be proved by TEM observation in the later section). Moreover, the same peak at 29.1° has less intensity in exf-HTO than HTO, further confirming the exfoliation. A similar XRD reflection is also reported for a LT, which is exfoliated by a bulky organic amine[101].

Raman spectra of the samples are shown in Figure 3.2.c. Accordingly, the peak at 887 cm^{-1} indicates the distorted TiO_6 with a short Ti-O bond[102], which may be more affected by the presence of K^+/Li^+, where after replacing it with H^+, the relevant peak almost disappears. The peaks at 279, 450, and 649 cm^{-1} are assigned to Ti-O-Ti stretching modes of TiO_6 octahedra units[101]. In conclusion, by comparing the Raman spectra of KTLO with the HTO and exf-HTO, the only change that can be observed is related to the interlayer surface chemistry, emerging as a peak at 887 cm^{-1}, while the main backbone has a similar structure.

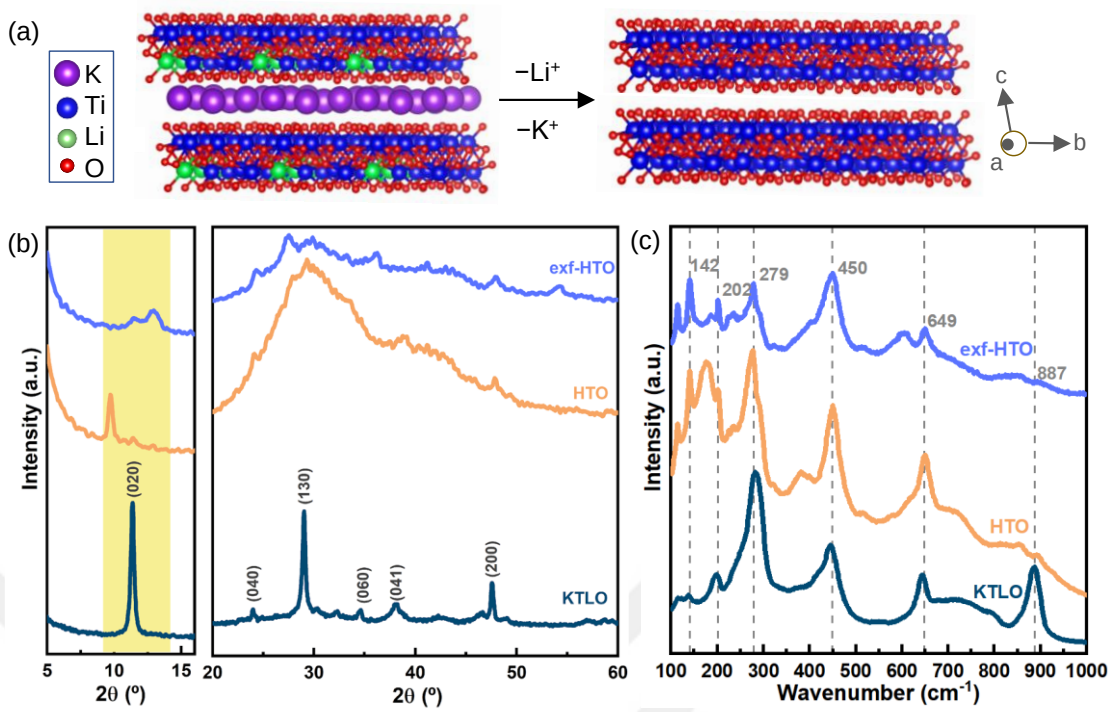

Figure 3.2. Crystal structures of KTLO and HTO from the edge view (020) plane. (a) XRD patterns (b) and Raman spectra (c) of KTLO, HTO, and exf-HTO.

UV-vis spectra and Tauc plots, which are used to determine light absorption properties and the bandgap of the photocatalysts, are presented in Figure 3.3a and Figure 3.3b, respectively. While KTLO and HTO absorbed light with a wavelength shorter than 350 nm, the absorption property of exf-HTO reaches 400 nm. Tauc plots clearly demonstrated a change of the bandgap upon protonation and exfoliation; 3.19 eV was estimated to be the bandgap of exf-HTO, while larger values, 3.52 and 3.79 eV were found for HTO and KTLO, respectively. A simple exfoliation method caused this remarkable change in the bandgap values and made this LT more sensitive to the light in the visible spectrum. The increased light absorption of the exf-HTO could be attributed to the introduction of new energy levels in the bandgap. Defects such as oxygen vacancies, titanium vacancies, and interstitials could be introduced on the surface or in bulk during exfoliation, which could generate energy levels inside the bandgap[86].

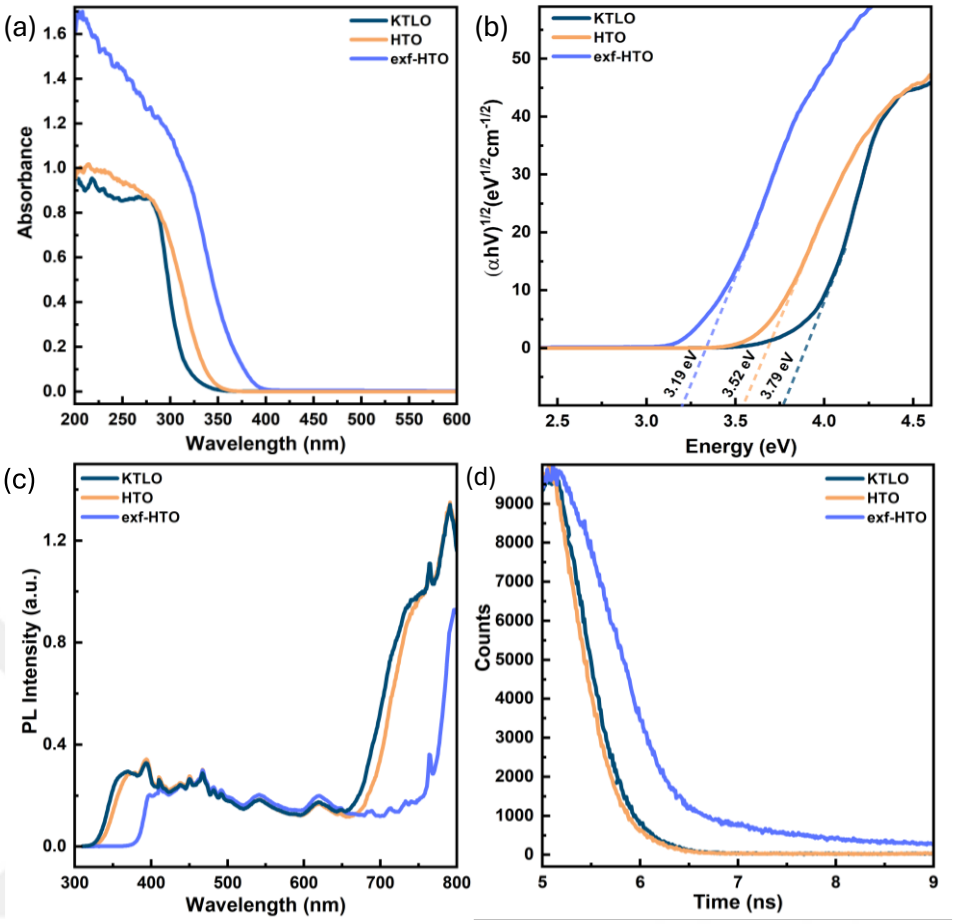

Figure 3.3. UV–vis spectra recorded in a diffuse reflectance mode (a), Tauc plot from UV–vis spectra using Kubelka–Munk conversion (b), emission spectra (c), and time-resolved PL decay profile (d) of KTLO, HTO, and exf-HTO.

Exfoliation had a significant impact on the utilization of the charge carriers and their lifetime. It is seen in Figure 3.2c that pure KTLO and HTO exhibit a broad peak in the region of 330-400 nm, having maxima at around 360 nm. The band edge emission and defect emission are two decay channels commonly suggested to describe the origin of the PL emission signals. Oxygen vacancy-mediated states resulting from the synthesis, protonation, and exfoliation could trap charge carriers and affect the emission profile. The PL spectra of exf-HTO show a red-shift of the peak maximum compared to that of KTLO and HTO, which can be attributed to the altered band structure in agreement with its UV–vis absorption characteristics. Figure 3.3d demonstrates the fluorescence emission decays at the wavelength where the peak maximum is investigated to determine the lifetime of

the charge carriers in samples. The recombination appears to be the slowest for the exf-HTO. The lifetimes were calculated by the deconvolution of the decay curves and the values obtained for KTLO, HTO, and exf-HTO are 1.08, 0.94, and 1.57 ns, respectively. The increased lifetime of the charge carriers in the exf-HTOs reveals that the exfoliation-induced modifications are playing a critical role.

It is demonstrated that the morphology, crystal structure, and thickness of the exfoliated layered titanate through several microscopic techniques, including SEM, TEM, and AFM. The observed morphologies in SEM and TEM (Figure 3.4a, e) images match with each other and indicate a uniform nanostructure shaping from a randomly oriented morphology of KTLO. The thickness of exf-HTO compared to the normally protonated HTO (up to 35 nm, judging from the SEM image in Figure 3.4b) shows that our method significantly exfoliates the titanate layers along with protonation. Furthermore, by measuring the thickness of the representative exf-HTO particle, ~8 nm, which can include the stacked from ~11 layers of LT, where the lateral size shows ~90 nm. The observed lateral size in AFM is also a close value to the obtained average lateral size value from the SEM image of exf-HTO (~75 nm, Figure 3.4g, see the inset), and the thickness is almost matching with the one observed by cross-section HRTEM (17 layers, see Figure 3.4l). The HR-TEM and HR-HAADF-STEM images of the exf-HTO show a single crystalline structure from the lateral dimension of the layer where the obtained d value from the observed facet is 0.715 nm, assignable to the (200) plane (Figure 3.4k). The edge view of exf-HTO also indicates a d value of 0.72 nm, which can be assigned to the obtained XRD peak at 12.3º, Figure 1b. Note that, due to the low long-range order of the exfoliated layers, the crystalline structure of the titanate layers can only be observed through the HR-HAADF-STEM and HR-TEM-captured images, where the XRD pattern is seldomly revealing this crystallinity due to the limited long-range order of the layers (Figure 3.1b). It is also captured an HRTEM image from the edge view of the exf-HTO showing the stacking of 17 layers where the layers are free of K^+ (Figure 3.1l) in comparison with a KTLO group (Figure A1.1); see the presence of K^+ in the HR-TEM image that is captured in the edges view of the layers.

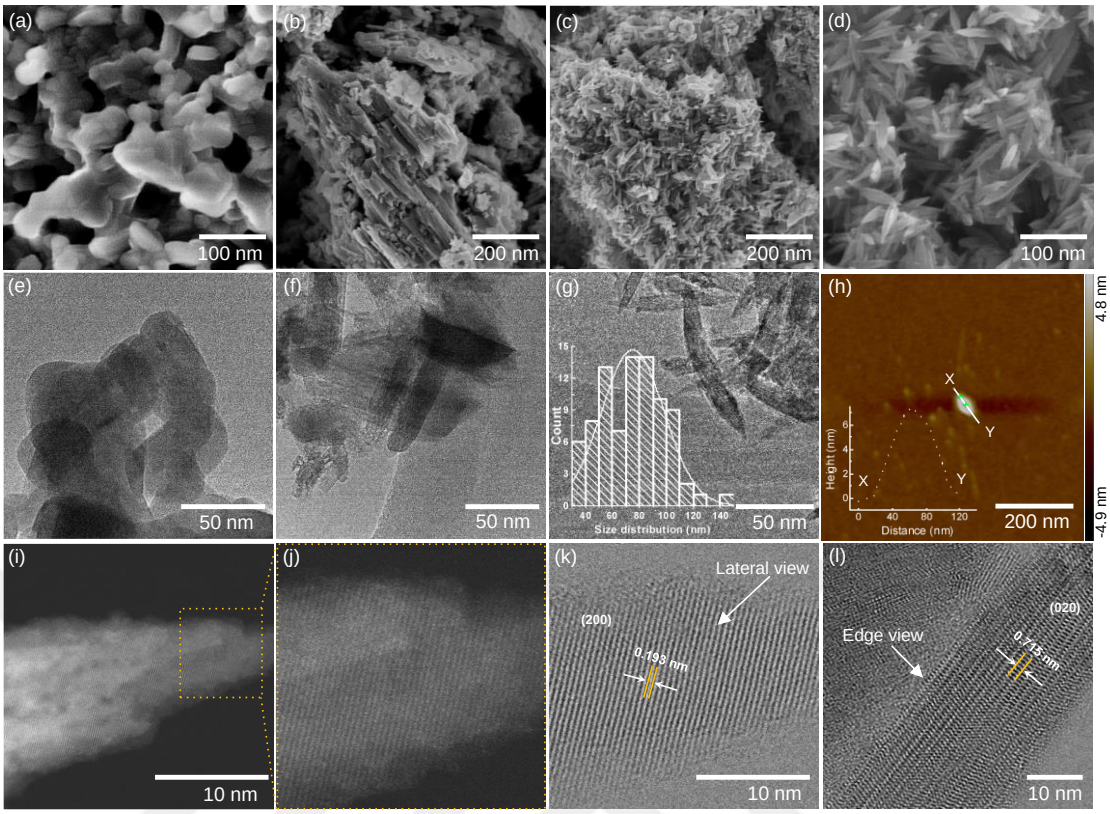

Figure 3.4. SEM images of KTLO (a), HTO (b), exf-HTO (c, d), and TEM images of KTLO (e), HTO (f), exf-HTO with a lateral width size distribution (g), AFM image of exf-HTO with a height profile (h), HRTEM with low and high magnification (i, j), HRSTEM with a lateral view and (200) planes according to the d value (0.193 nm) (k), and cross-sectional HRTEM of exf-HTO showing layer edges and 0.715 nm thickness (l).

XPS was used to investigate the surface composition and chemical state of photocatalysts. Ti 2p XPS spectra presented in Figure 3.5a exhibit peaks observed around 457 eV to 464 eV binding energies for Ti $2p_{3/2}$ and Ti $2p_{1/2}$, respectively. The Ti $2p_{3/2}$ peak shifted to higher binding energies from 457.9 eV (KTLO) to 458.8 eV (exf-HTO) as well as Ti $2p_{1/2}$ peak shifted from 463.7 eV (KTLO) to 464.5 eV (exf-HTO). HCl treatment results in K^+ and Li^+ ions at the interlayers of KTLO exchanged with H^+. When protonation and, eventually, exfoliation occur, the bond distance between Ti and O gets shorter with the H^+ ions presence since the electrostatic interplay between O and K^+/Li^+ ions is much stronger than that between O and H^+ ions[76]. The absence of the peaks in the high binding energy side of the spectra indicates that protonation and exfoliation treatments did not lead to the reduction of Ti. Similar shifts to high binding energies from

KTLO to exf-HTO were also observed in O 1s spectra, as demonstrated in Figure 3.5b. O 1s spectra were deconvoluted into three peaks. The main component represents oxide ions (Ti-O-Ti), high binding energy shoulder within ~531.1-532 eV, on the other hand, are assigned to hydroxyl groups (-OH) coordinated to the surfaces of the layers. Exfoliation treatment increases the number of -OH groups since more surface layers are susceptible to hydroxylation, and water adsorption is created (the component at the highest binding energy).

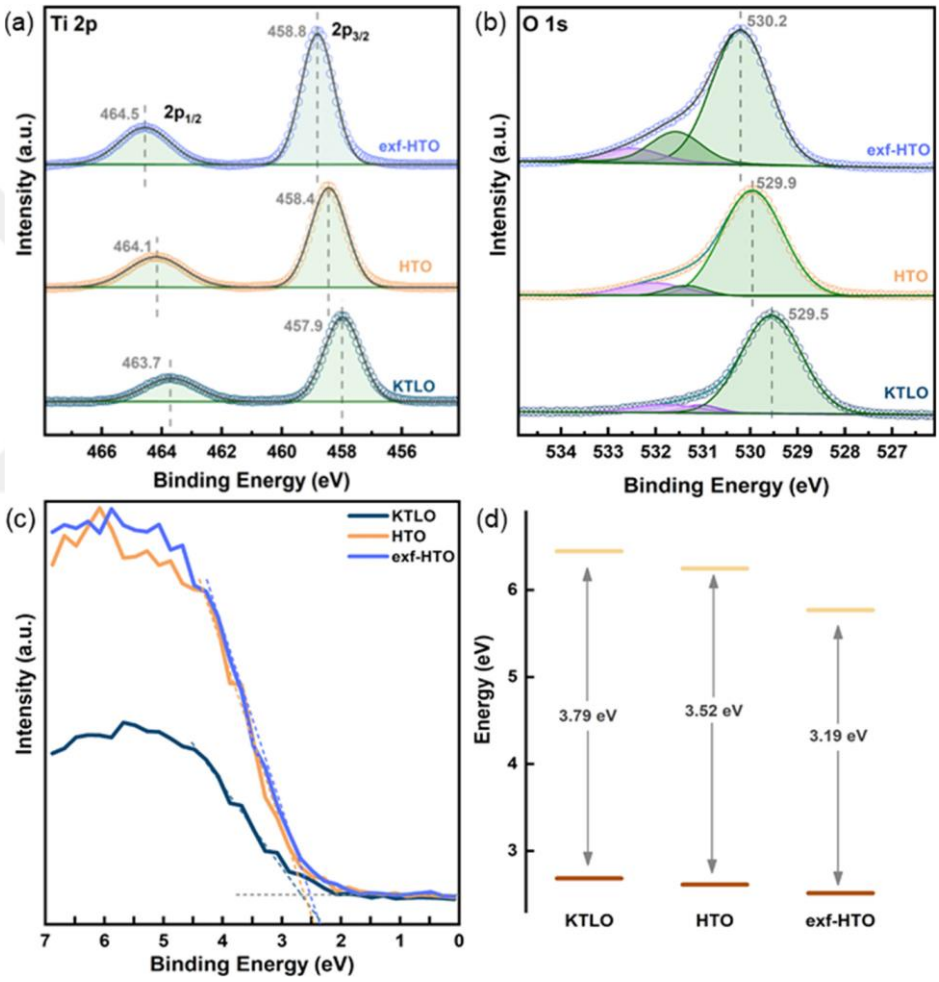

Figure 3.5. Ti 2p (a), O 1s (b), and VB (c) XPS spectra of KTLO, HTO, and exf-HTO, respectively. The alignment of the band edges based on VB edges determined by XPS and bandgap energies estimated by Tauc analysis (d).

Valence band (VB) XPS spectra presented in Figure 3.5c could provide energy positions of the occupied energy levels. A close inspection of the band edge position

reveals that the VB maximum moves down in energy upon exfoliation. This binding energy change matches with the energy shifts observed in core levels. A combination of bandgap energies estimated by Tauc analysis and VB maxima obtained in Figure 3.5c could be used to construct relative changes in the energy positions of KTLO, HTO, and exf-HTO. As summarized in Figure 3.5d, the gradual drop in the VB energy position and smaller bandgap energy significantly lowers the conduction band (CB) position.

It is further explored the morphology of the exfoliated layered titanates after Sn loading and confirmed that the Sn loading process has no destructive effect on the nanostructure of the exf-HTO (see Figure 3.6a, b, and c). The HR-STEM represents some light dots on the crystalline fringes of the LT, showing that the Sn species are in single-atom form and distributed on the surface. TEM-elemental mapping further confirms the thorough distribution of Sn uniformly along Ti and O on each particle (Figure 3.6e-g) without forming any Sn nanoparticles.

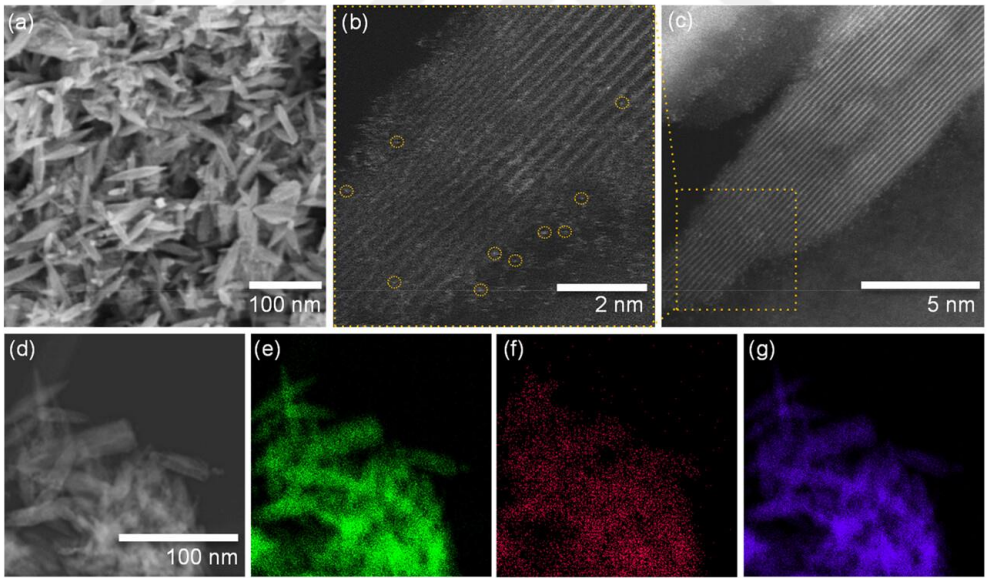

Figure 3.6. SEM image (a), TEM images (b, c), electron image (d), elemental mapping of O Kα1 (e), Sn Lα1 (f), and Ti Kα1 (g) of Sn/exf-HTO.

Despite Sn single atoms being well distributed on the surface of LTs, the loading process has significantly changed the XRD pattern (Figure 3.7a). A broad background feature located around 30° similar to the one observed for HTO reappeared, and all the

diffraction features remained buried under this background. No significant change in Raman spectral features has been observed (Figure 3.7b). This structural change could indicate that the long-range order has been lost upon Sn loading; however, the local structure and the coordination of the atoms remain intact. Sn single atoms not affecting vibrational features could be explained by their low loading. The reverse effect of the Sn loading is also evident in optical spectra. UV-vis spectra and respective Tauc analysis reveal band re-opening and bandgap energies shift from 3.19 to 3.41 eV (Figure 3.7c). Interestingly, steady-state PL intensity decreases within 400-600 nm (Figure 3.7d), suggesting that the recombination emission process has lost its dominance. Generally, the crystallinity and defect densities play a vital role in carrier extraction; however, the possible influence of the Sn loaded on the surface must undoubtedly be considered. Reduced PL intensity suggests that single-atom Sn layers could achieve better carrier extraction. Time-resolved PL decay measurements performed (Figure 3.7d) help us better understand the carrier decay behavior[103]. Further decreased PL decay lifetimes from 1.57 to 0.97 ns point out that the efficiency of the charge carrier extraction could be increased by a single atom Sn layer.

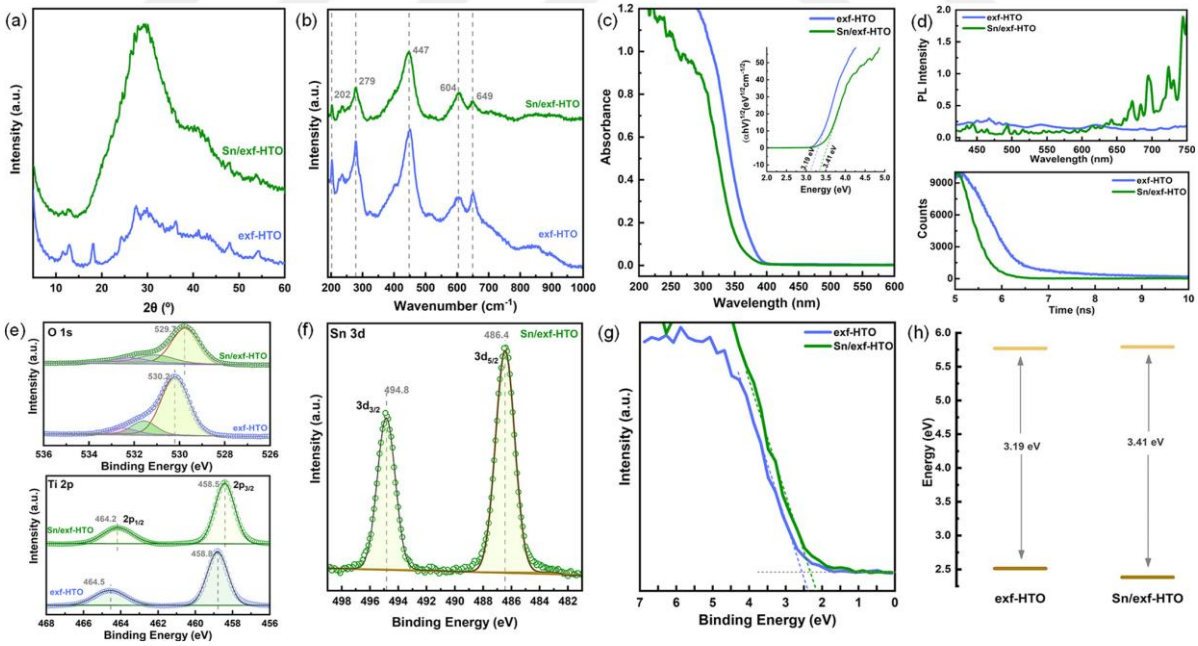

Figure 3.7. XRD pattern (a), Raman spectra (b), UV-vis spectra and Tauc plots (c), steady-state PL emission and time-resolved PL decay profile (d), Ti 2p-O 1s (e), Sn 3d

(f), and VB (g) XPS spectra of exf-HTO and Sn/exf-HTO. The change in the alignment of the band edges is shown in (h).

Ti 2p and O 1s XPS main peak positions shifted to lower binding energies after Sn loading (Figure 3.7e). This binding energy shift seems to be related to the partial restacking of the layers as in the HTO structure. Sn single atoms remain on the surfaces of the layers. O 1s spectral deconvolution indicates that the peak previously assigned to H_2O hydrogen bonded to surface OH groups has a lower intensity due to lowered exposed surface layers. Sn 3d XPS spectrum (Figure 3.7f) contains $3d_{5/2}$ and $3d_{3/2}$ spin-orbit components located at 486.4 and 494.8 eV, respectively, suggesting that Sn exists with 2^+ state on the surface[104]. Comparing the Sn 3d XPS spectra of Sn^{4+}-loaded exf-HTO with the one prepared here from Sn^{+2} (see Figure A1.2) further proves that the oxidation state of Sn in Sn/exf-HTO has remained +2. Sn with metallic character is not expected; no Sn (nano)particles were found under TEM observation, and the BE of metallic Sn does not overlap with the BE of the existing loaded Sn in Sn/exf-HTO[105]. Sn loading leads to a small shift in VB maxima (Figure 3.7g), which reestablishes the VB and CB edge positions (Figure 3.7f).

The photocatalytic activity of the Sn-loaded protonated exfoliated HTO (Sn/exf-HTO) was tested for hydrogen evolution reaction from water under solar light illumination. We also added MeOH (20 V/V%) to water for scavenging the photogenerated holes. First, the concentration of the treating solution of Sn for loading on exf-HTO was investigated. Accordingly, the exf-HTO was treated with different concentrations of Sn, and it found that when the Sn solution is 20 ppm, the photocatalytic activity is in optimal activity compared to other selected concentrations, including 10, 40, and 50 ppm. The Sn-loaded exf-HTO obtained by treating it with 20 ppm $SnCl_2$ solution produces ~3.5 $mmol.g^{-1}$ H_2 in 30 min of the illumination, while for the other concentrations, we observed lower values (Figure 3.8a). Loading lower than 20 ppm, Sn is expected to have lower photocatalytic activities, while for the higher concentrations (such as 50 ppm), it was surprising, and we investigated the reason for the decrease in photocatalytic activity by studying its structure and morphology with SEM, TEM, and HAADF-STEM, see Figure A1.3. According to our observation, the layers aggregate, although Sn concentration seems higher under HAADF-STEM, which points out that the

Sn is still in a single atom form but causes the aggregation of the particles and blockade of the direct light exposure to the active surface.

It is further compared the photocatalytic activity of the other titanates and a TiO_2 species with Sn/exf-HTO, in which Sn/exf-HTO has higher photocatalytic activity in H_2 evolution (3.56 mmol/g) under identical conditions. To prove that the exfoliation step has a significant impact on the photocatalytic H_2 evolution reaction, we compared exf-HTO with its corresponding HTO and found that the exf-HTO produces ~241 μmol g^{-1} more H_2 than the HTO in 30 min under the identical conditions. As a reference, we also evaluated the photocatalytic activity of KTLO to show that its activity is minor (Figure 3.8b) compared to the Sn/exf-HTO and the protonated ones. This low activity can be due to the fact that KTLO is still bulk layered material, and its activity is considerably poorer. Furthermore, along with the photocatalytic activity enhancement originating from protonation and exfoliation of the LT, loading Sn single atoms plays a significant role in the photocatalytic activity enhancement when we compare the KTLO, HTO, and exf-HTO with Sn/exf-HTO as a trajectory of post-modification (Figure 3.8b, see the inset). This improvement in the photocatalytic activity after Sn loading can be due to the faster charge carrier separation, as judged by the PL decay profiles comparison of Sn/exf-HTO and exf-HTO, see Figure 3.7d. To our surprise, the Sn/exf-HTO exhibits even better solar-driven photocatalytic H_2 evolution activity than the commercial TiO_2 (P25). The Sn-loaded TiO_2 (P25) under identical preparation conditions (see Figure 3.8) has a minor impact on the activity. This observation shows that the Sn species loaded on TiO_2 is not show the same mechanism of charge carrier photogeneration that occurs in the exf-HTO. Comparing the photocatalytic activity of Sn/exf-HTO with the previous reports for LTs also further proves the excellent photocatalytic activity improvement after Sn loading[36], [71], [77], [106].

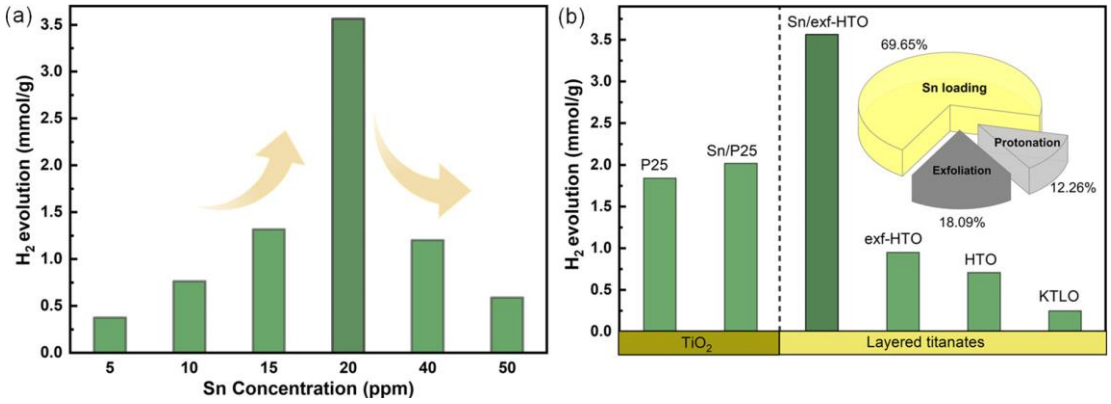

Figure 3.8. Solar-driven photocatalytic H_2 evolution reaction from water containing methanol on Sn/exf-HTO loaded with different concentrations of Sn (a), photocatalytic activity comparison of Sn/exf-HTO (20 ppm) with other corresponding versions of LTs and the commercial TiO_2 (P25) and Sn-loaded P25 (b).

We further evaluated the photocatalytic activity of the Sn/exf-HTO LT in AB dehydrogenation reaction at room temperature. AB can decompose into various forms, depending on the (photo)catalytic activity. However, each mole of AB usually converts to one mole of ammonium borate salt and three moles of H_2 as follows[107]:

$$NH_3BH_3 + 2H_2O \rightarrow 3H_2 + NH_4BO_2 \qquad \text{(eq. 1)}$$

Firstly, it is investigated whether Sn has any photocatalytic activity impact on AB dehydrogenation. Accordingly, when the reaction is carried out in the dark, the H_2 generation is minimal, while in the presence of solar light, the AB dehydrogenation completes within 10 min. We also studied the impact of Sn loading amount on photocatalytic AB dehydrogenation and likewise hydrogen evolution reaction; the 20 ppm $SnCl_2$-treated exf-HTO exhibited a superior photocatalytic activity compared to selected lower and higher Sn concentrations treated with exf-HTO (Figure 9a). Here, the photocatalytic activity of Sn loading on exf-HTO was compared with the Sn-loaded P25 (a commercial TiO_2), unexfoliated HTO, and bare HTO (Figure 9b). In all cases, the single atom Sn/exf-HTO revealed a superior activity than other Sn-loaded and unloaded titanates and TiO_2. It is also important to note that the Au/P25 also showed less activity than the Sn-loaded exf-HTO, which can be pointed as an alternative to noble metals that are believed to be promising cocatalysts for TiO_2-based materials[108]. Moreover, Au, as a noble metal cocatalyst, also possesses plasmonic activity that can enhance further but

fails to show higher photocatalytic activity than the Sn-loaded exfoliated HTO. It also studied the photocatalytic activity of the Sn/exf-HTO in the dehydrogenation of the AB through the illumination of monochromatized light to see the efficiency in the target photocatalytic reaction at various wavelengths. Accordingly, the photocatalytic activity of Sn/exf-HTO in the shorter wavelengths of the UV range is significantly higher, and a significant decrease in the photocatalytic activity occurs as it approaches the visible range. This observation matches well with the UV-Vis absorption spectra, see Figure A1.4.

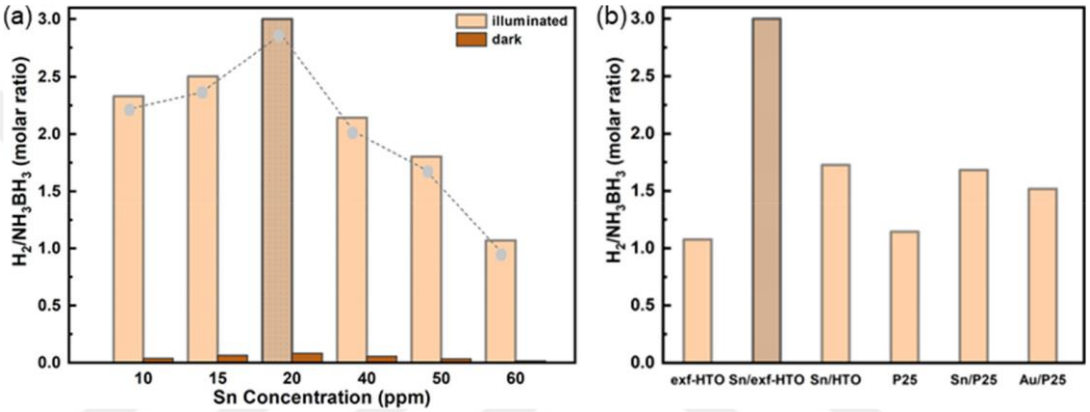

Figure 3.9. Comparison of Sn/exf-HTO photocatalytic activity in AB dehydrogenation reaction under illumination and dark conditions through different Sn loading amounts (a), comparing AB dehydrogenation reaction rate of different TiO_2-based photocatalysts with exf-HTO and Sn/exf-HTO (b).

The photocatalytic activity of the recovered sample from AB dehydrogenation also indicates a slight decrease (Figure A1.5), confirming that the photocatalyst is reusable. Sn 3d XPS spectra of the recovered Sn/exf-HTO (Figure A1.6) after photocatalytic AB dehydrogenation were investigated to monitor any possible reduction of Sn species since AB can sometimes reduce the metals during the reaction[109]. By comparing the Sn 3d XPS spectra of pristine and recovered Sn/exf-HTO, the oxidation state of the Sn had no sensible alteration during the photocatalytic AB dehydrogenation reaction. Furthermore, the XRD pattern and Raman spectral features of the Sn/exf-HTO-rec slightly differed from the Sn/exf-HTO, showing that the HTO structure is also sustainable and stable during the reaction process (Figure A1.7).

3.5 Conclusion

In summary, the layered titanate was successfully exfoliated via a facile additive-free method, which provided an enhanced photocatalytic activity by narrowing the bandgap and prolonging the photogenerated electron/hole lifetime. Sn loaded on exf-HTO was found in single atom form homogeneously distributed on the surface, and Sn seemed to be agglomerated when its loading was increased. A significant fraction of the enhancement of the photocatalytic activity toward hydrogen evolution and AB dehydrogenation reactions was due to the Sn single atom decoration on exf-HTOs. The oxidation state of Sn, the morphology, and the lepidocrocite structure of the exf-HTO was found to be sustainable during the photocatalytic reactions. Therefore, the single-atom Sn species can be proposed as an excellent candidate to trigger the photoactivity of the exfoliated layered titanates. At the same time, the other metals can be further explored from the perspective of the exfoliated layered titanates.

Chapter 4:

PHOTOCHEMICAL AND PHOTOELECTROCHEMICAL ACTIVITY OF CTAB INTERCALATED CESIUM TITANATES

4.1 Introduction

In a photoelectrochemical (PEC) water splitting system, sunlight is absorbed by the photoelectrode, which then immediately splits water into hydrogen and oxygen. Primary research being done on PEC water splitting now focuses on improving the stability and efficacy of photoactive materials[110]. However, no material has yet been discovered that simultaneously satisfies the efficiency and stability requirements for the industrial utilization of hydrogen technology despite consistent efforts and certain advances[111].

Illumination, the separation, and migration of photogenerated electrons and holes for the hydrogen evolution reaction and oxygen evolution reaction processes on photocatalyst surfaces are the three basic processes involved in photocatalytic water splitting[112]. Water's redox potentials must fall between the photocatalyst bandgaps, necessitating bandgaps greater than 1.23 eV[113]. The absorption of sunlight, the capture and recombination of excited electrons and holes, as well as surface reactivities all affect how well the photocatalysts work. A widely used concept to create high-performance photocatalysts is band engineering of semiconductors[114].

A viable photoanode for PEC water splitting is titanium dioxide because of its advantageous band-edge positions, potent optical absorption, and inexpensive cost. However, the efficiency of its solar to hydrogen is constrained by its large band gap energy and fast electron-hole recombination. The goal of the research is to improve the electrical structure, morphology, and absorption of visible light for efficient charge carrier separation and conveyance[115].

The interlayer chemistry, ion exchange or intercalation processes, and prospective uses in the creation of nanomaterials are drawing interest to layered titanates. They are desirable building blocks for artificial structures, hybrid multilayers, or microporous materials because they can go through exfoliation or delamination, creating single sheets with characteristic two-dimensional morphology[116]. The uses of layered titanates have received a great deal of attention in the field of photocatalysis because of their layered structure and benefits, such as simplicity in synthesis, low cost, and being

environmentally friendly. Cesium titanate is an example of a typical layered metal oxide semiconductor. Ion exchange reactions and proton intercalation can both replace the alkali metal cations intercalated between the sheets of condensed transition-metal oxide polyhedra with other cations[117]. Due to its open layered structure with the titanium oxide sheets that are spatially separated by cesium cations, the layered cesium titanate represents a good starting material for further modifications regarding the incorporation of different species[77].

To achieve the goal of increasing the utilization efficiency of the incident light and photoconversion efficiency of layered titanates, creating heterostructures of layered titanates would make it easier to transfer and separate photo-generated electron holes. The effective dispersion of the surfactant capping agent on the surface of the produced photocatalyst is credited with the promising performance. The activity triggered with light illumination can be more effective by utilization of the CTAB-capped photocatalyst due to the hydrocarbon from its non-polar tail[118].

CTAB intercalation in cesium titanate improves photocatalytic and photoelectrochemical activities by improving charge separation and increasing surface area. This interlayer spacing allows for efficient migration of charge carriers, reducing recombination of the expanded surface area and providing more active sites[119]. The intercalation process creates a layered structure with alternating organic and inorganic layers, allowing charge carriers to migrate and diffuse more freely within the material[120]. CTAB intercalated cesium titanate heterostructures exhibit effective photoelectrochemical oxygen evolution and photocatalytic hydrogen evolution under illumination. The characteristics of the material may alter as a result of the carbonization of CTAB at high temperatures. The resulting layers containing carbon change the surface chemistry of titanate sheets, electrical conductivity, and optical characteristics. The variation in carbonization temperature affects the properties of these heterostructures, including surface area and active site distribution.

4.2 Experimental Procedure

The synthesis of cesium titanates was described in Section 2.1.1, and the intercalation of CTAB into CsTO and the carbonization processes were explained in Section 2.2. The thin film preparation of the samples was described in Section 2.3. Photocatalytic setup

was explained in Section 2.4.1. Photoelectrochemical experiments were described in Section 2.5. 0.1 M Na_2SO_4 was used as the electrolyte at pH=7 and purged with nitrogen for 20 minutes beforehand. Structural characterizations of the samples were explained in Section 2.6.

4.3 Results and Discussion

The XRD spectra presented in Figure 4.1a illustrate the discernible influence of CTAB intercalation within the layers of cesium titanate, as evidenced by the intensified peak observed at an angle of 2θ=10.1º. This augmentation in peak intensity is attributed to the expansion of the interlayer spacing[121]. It is evident that the added cationic surfactant was intercalated between the titanate layers, given that the interlayer spacing of the titanate in the samples was dependent on the length of the long alkyl chain of the added surfactant[122]. The as-synthesized cesium titanate, prepared with a molar ratio of Cs:Ti as 1:3, predominantly consists of the orthorhombic phase of $Cs_2Ti_6O_{13}$ (PDF card number: 00-038-0170). Furthermore, the characteristic peaks corresponding to CTAB remain unchanged across samples exhibiting distinct concentrations of CTAB. In Figure 4.1b, the impact of carbonization at 600ºC on CTAB-intercalated cesium titanate samples (CTAB-CsTO) is shown. Notably, the distinctive peaks indicative of the cesium titanate phase remain unaltered following the carbonization process. After high-temperature treatment, a substantial portion of the CTAB molecules undergo a transformation, resulting in the formation of a carbonaceous layer. Particularly in the sample containing a higher concentration of CTAB (0.25 M), discernible changes are observed, with the disappearance of peaks at 2θ =17.1º, 21.4º, and 24º. In Figure 4.1c, the additional impact of varying carbonization temperatures is elucidated. At a carbonization temperature of 700°C, the peaks attributed to CTAB exhibit considerable attenuation and near disappearance. This phenomenon can be attributed to the progressive thermal degradation of CTAB molecules, potentially leading to the breakdown of their long-chain structures[123]. This transformation contributes to changes in the interlayer spacing as carbonaceous layers become more prevalent with higher carbonization temperatures.

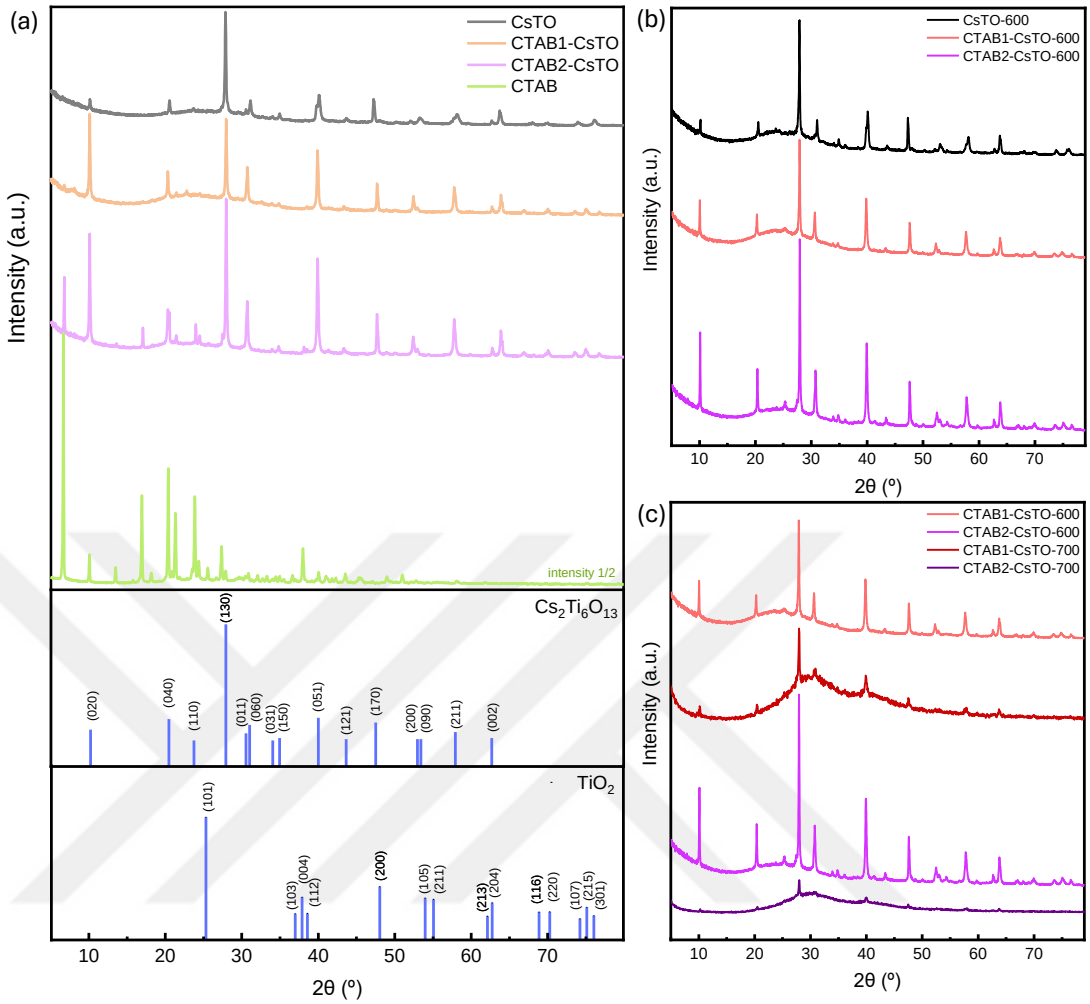

Figure 4.1. XRD spectra comparison of pristine cesium titanate and intercalated versions with different concentrations of CTAB (a), comparison of after carbonization samples (b), and the impact of carbonization temperature on CTAB1-CsTO and CTAB2-CsTO (c).

The UV-Vis absorption spectra with a diffuse reflectance mode of the respective samples, with their Tauc plots obtained through Kubelka-Munk transformation for bandgap energy determination[124], are shown in Figure 4.2. It is observed that pristine cesium titanate and CTAB-treated samples absorption edges. Notably, with the increment in the quantity of CTAB, the absorbance edge exhibits a discernible flattening (Figure 4.2a). This observed trend indicates the presence of a relatively confined size distribution of particles dispersed, indicative of the effects induced by the addition of CTAB[125].

UV-Vis absorption peaks red-shifted as a result of CTAB intercalation, principally because of changes to the electronic structure brought on by interactions with titanate layers. Between the layers, CTAB could change the energy levels in the titanate layer, which can affect the electrical band structure. Particularly at CTAB-titanate surfaces, these interactions can modify surface states and change the light absorption characteristics. The total energy needed for electronic transitions is reduced as a result of these modifications since the bandgap energies are shifting to lower energy by intercalation and thermal treatment. It is also observed that the pristine CsTO exhibits absorption at 343 nm and a wide bandgap of 3.5 eV, which is consistent with the previous works[124]. It is notable that semiconductors possessing wide bandgaps, such as layered titanates with comparable characteristics, often exhibit limited photocatalytic activity[126]. The prominent absorption peak of CTAB2-CsTO-700 at approximately 400 nm signifies the most efficient light absorption among the other samples that correspond to better photochemical and photoelectrochemical activity, and this noteworthy feature provides a crucial explanation for the photocatalytic activity results discussed in the following sections. The fact that anatase TiO_2 has a wide band-gap semiconductor (3.2 eV) and is only functional at UV wavelengths of about 385 nm is widely known[127]. The CTAB effect can be thought of as being made up of separate layers of intercalated cations on TiO_6 octahedrons. The band gap of CTAB-intercalated samples (CTAB1-CsTO and CTAB2-CsTO) is even wider (3.5 eV) than anatase, which can be explained by the quantum size effect[128].

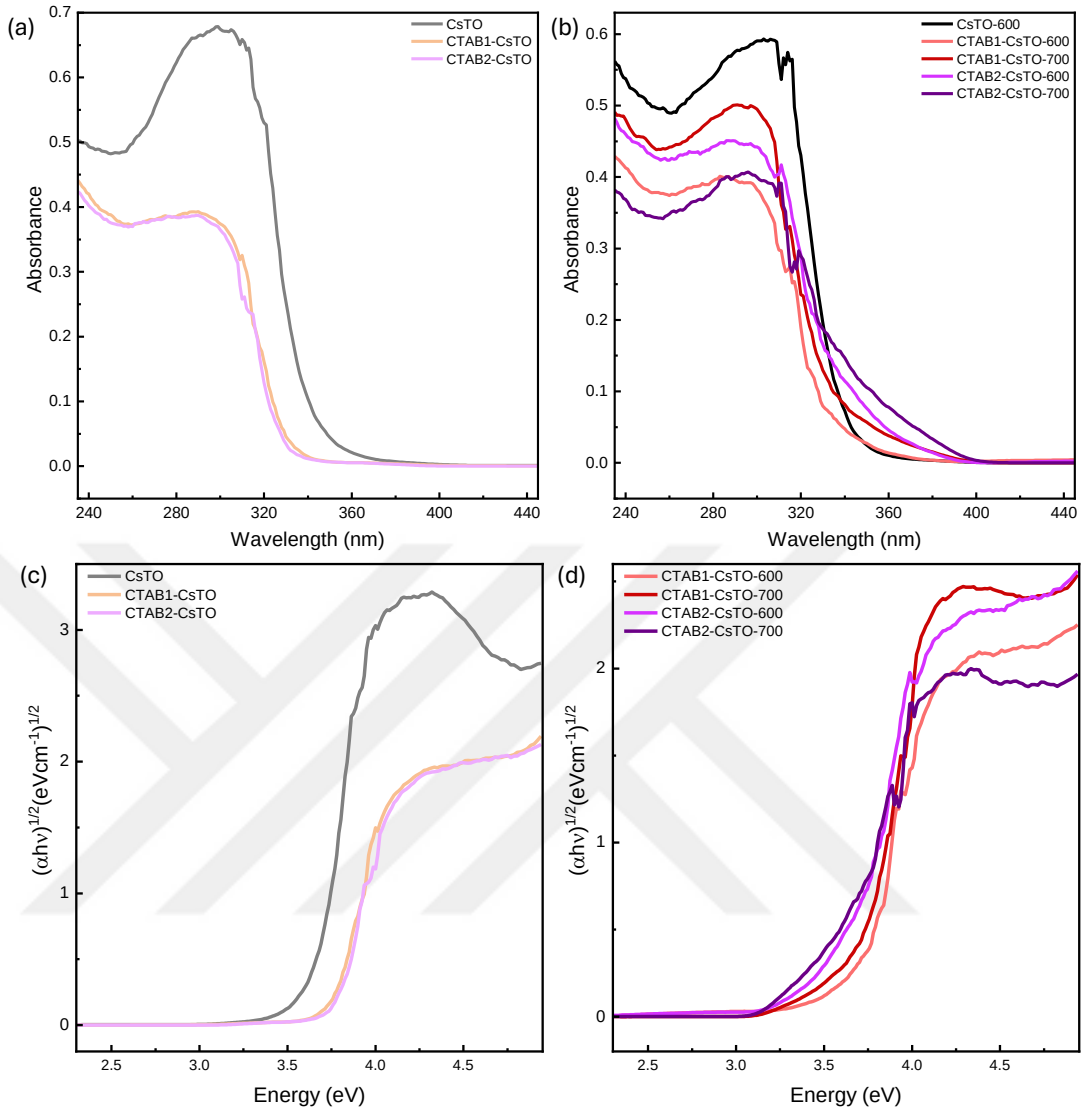

Figure 4.2. UV-Vis spectra of corresponding samples with comparisons by their CTAB concentration (a), carbonized forms with their carbonization temperature comparison (b), and their Tauc plots derived with Kubelka-Munk conversion (c) and (d), respectively.

The Raman spectra corresponding to the specified samples are presented in Figure 4.3. Ti-O lattice vibrations and Ti-O-Ti bonds were found with Raman shifts of 275 and 441 cm^{-1}, respectively. Corresponding peaks at 638 and 690 cm^{-1} for rutile A_{1g}, antisymmetric bending vibration of Ti-O-Ti, and Ti-O-H, respectively[129]. Interestingly, the intercalation of CTAB within the interlayers of the layered titanate elicits small changes in the prominent peaks discernable within the Raman spectra. Due

to Cs-O stretching originating from cesium titanate network, the peaks at 914-919 cm^{-1} were preserved[130]. In particular, the peak caused by the stretching vibrations of the short Ti-O bonds (Figure 4.3a) interfering with the interlayer gaps marginally shifts slightly from 916 cm^{-1} for CsTO to 919 cm^{-1} with the introduction of CTAB into the structure, indicating a minor adjustment to the Cs-O(Ti) interactions [131]. In the layered structure of CsTO, a distinct Raman signal appears at 276 cm^{-1}, showing the presence of Ti-O bonds[132]. This discovery further shows that the TiO_2 anatase phase can emerge when the CTAB-CsTO samples are treated at a temperature of 700ºC.

After the carbonization process (Figure 4.3b), the anatase phase of TiO_2 was observed according to the Raman spectra; a Raman shift at 143 cm^{-1} and 515 cm^{-1} as Raman active modes for TiO_2 and is due to the dominant E_{1g} and A_{1g} vibrational mode in anatase TiO_2[133], [134]. Moreover, a distinct carbonization procedure applied to the CTAB1-CsTO and CTAB2-CsTO samples at 700ºC shows a pronounced TiO_2 anatase phase peak at 143 cm^{-1} as well as 638 cm^{-1}[135]. This outcome suggests that at this elevated temperature, the dominant phase transformation involves the conversion of the TiO_2 anatase phase, superseding the formation of a carbonaceous layer originating from CTAB[136]. It is consistent with the other works that 600ºC and beyond temperatures, such as 700ºC, influence the anatase phase transformation occurring with the high intensity of the peak at 143 cm^{-1} [137]. Contrary to the distinct peaks seen in the CTAB1-CsTO and CTAB2-CsTO samples, thermally treated pristine CsTO samples at 600°C and 700°C (referred to as CsTO-600 and CsTO-700, respectively) lack pronounced peaks corresponding to TiO_2 at 143 cm^{-1}. This suggests that the intercalation of CTAB within the interlayers affects the formation of TiO_2 bonds and causes variations in the surface Ti content. These consequences will be discussed in more detail in the section with XPS results, which will offer additional context.

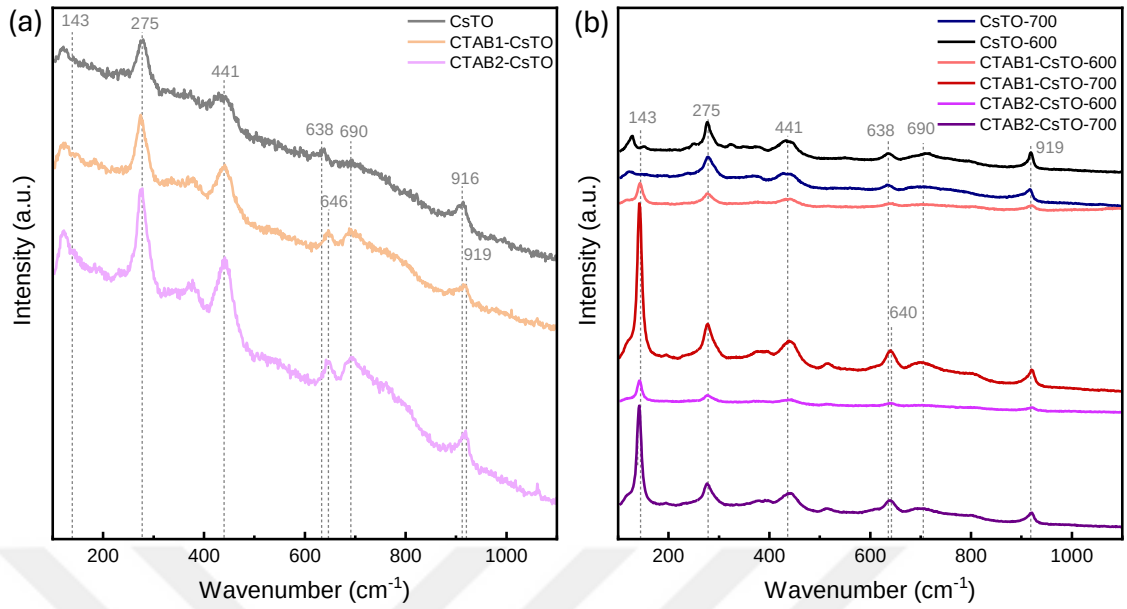

Figure 4.3. Raman spectra of the corresponding samples CTAB intercalated (a) and comparison of different carbonization temperatures (b).

FTIR spectra of the following samples are shown in Figure 4.4. Broad infrared bands at 1628 and 3370-3600 cm^{-1} point to the existence of H_3O^+ ions or H_2O molecules in the interlayer space and/or surface[138]. Also, n-alkylamine peaks are evident within the FTIR spectra of n-alkylamine-intercalated titanate nanocomposites. Specifically, IR bands attributed to $-CH_2$ bending at 1470 cm^{-1}, as well as sp^3-hybridized C–H bond stretching vibrations spanning the range of 2855–2955 cm^{-1}, are consistently observed[139]. The peak at 721 cm^{-1} is attributed to O–Ti–O bending vibrations and Ti–O stretching of TiO_6 octahedral groups[140], while 910 cm^{-1} is related to the Cs-O bonding[141]. It is also shown that CTAB presence with the C-H stretching modes in the range 2800–3000 cm^{-1} are the dominant features in the FTIR spectra resulting from CTAB. The symmetric (d+) and antisymmetric (d-) CH_2 stretches provide the two prominent peaks at 2921 and 2850 cm^{-1}[142]. After the carbonization process of both CTAB1-CsTO and CTAB2-CsTO samples (Figure 4.4b), the main peaks of CTAB are absent due to its composition beyond ~200ºC[143] and becoming a carbon content structure. In Figure 4.4c, a peak at 1394 cm^{-1} was observed with a higher temperature of carbonization, which is attributed to $-CH_3$ surface bending vibrations[144]. The main finding from the FTIR analysis is that CTAB is clearly present in the CTAB1-CsTO and

CTAB2-CsTO samples, as shown by recognizable peaks. Importantly, these peaks gradually disappear after heat treatment, suggesting that CTAB may be subject to thermal degradation or it is only its non-polar tail. This degradation is a sign that these elements have been incorporated into the layered titanate's interlayers, where they no longer exist in their original CTAB form.

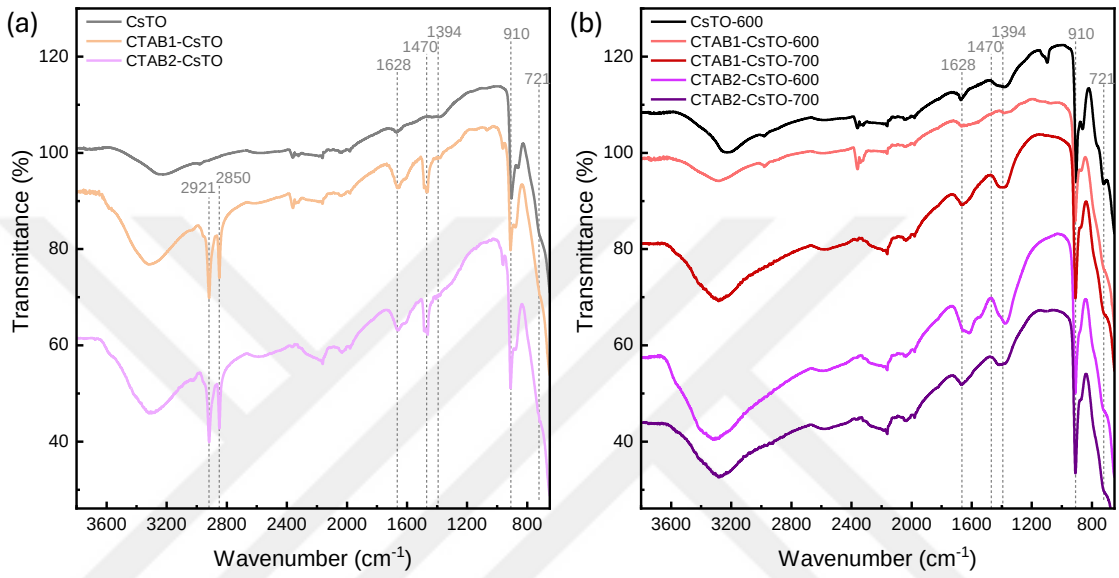

Figure 4.4. FTIR spectra comparisons indicating CTAB presence with different concentrations of CTAB (a), and thermal treatment temperature effect on CTAB intercalated samples (b).

Time-resolved photoluminescence emission spectra of the samples were recorded at the excitation wavelength 290 nm, shown in Figure 4.5a. Generally, it had been assumed that the charge transfer transition between metal and oxygen ions was what caused the luminescence of transition-metal oxoacids like titanates to occur[80]. Emission spectra with a maximum peak at 403 nm were observed for CsTO and also for CTAB1-CsTO and CTAB2-CsTO but with a decrease in intensity. Oxygen defects in the crystal structure can be formed in CTAB1-CsTO-700, and it has the lowest intensity around 400 nm. It is observed that after the carbonization process, peak intensity is decreased significantly for CTAB1-CsTO and CTAB2-CsTO compared to pristine CsTO. After the CTAB decomposition, nearby nanoparticles agglomerated, which enhanced the defect states and caused quenched intensity to be seen[125]. The intercalation of CTAB

with the layered titanate nanosheets suppressed the PL intensity of CsTO since the maximum PL intensity of CsTO was decreased from its initial intensity after CTAB treatment. A decrease in photoluminescence peak intensity may denote fewer photons emitting at a particular wavelength. Such a drop may be caused by changes in recombination dynamics, which are shown in Figure 4.5c and Figure 4.5d since modifications can change the electronic structure, carrier mobility, or recombination rates of the material. Additionally, PL measurements are sensitive to the features of the surface of materials, and peak intensities may be influenced by surface conditions. Therefore, a decline can be an indication of surface changes, and possible changes in the surface states was mentioned with Raman spectroscopy results. The observed significant difference of the PL intensities of CTAB-intercalated samples can be attributed for a noticeably lower electron-hole recombination rate given that the CTAB-CsTO samples demonstrated UV light absorption consistent with bare CsTO. The highly effective electron transport of the intercalated layered titanate components, which caused the separation of the electrons and holes, is thought to be the cause of this phenomenon[145]. Figure 4.5d demonstrates the lifetime decay of the corresponding samples. The recombination of the charge carriers appears to be slowest for CTAB2-CsTO-600 and CTAB2-CsTO-700 samples, which have an influence on photocatalytic activity.

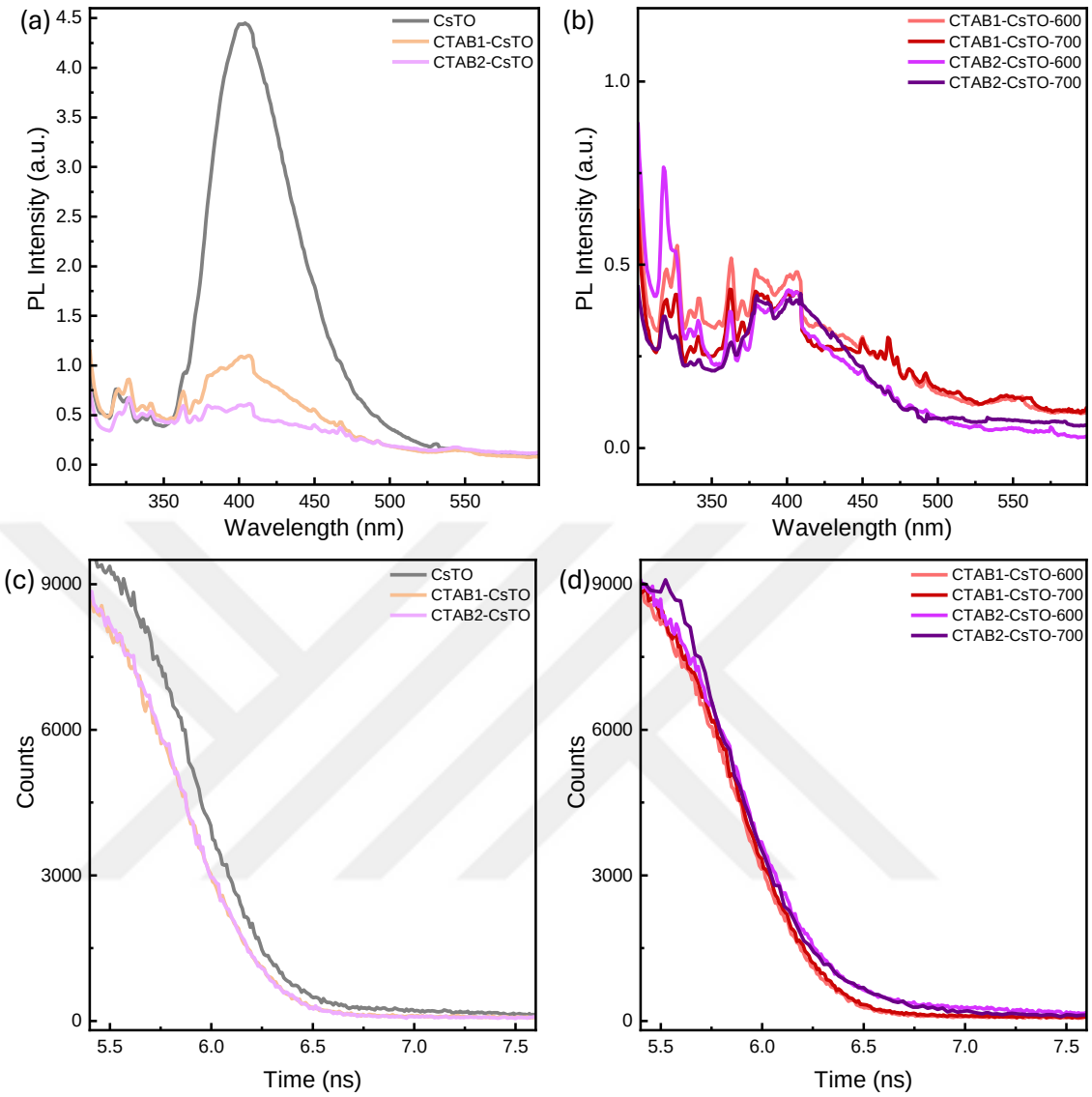

Figure 4.5. Time-resolved photoluminescence emission spectra (a), (b) and lifetime decays (c) and (d) of following samples.

XPS measurements were performed to investigate the surface characteristics of the respective samples. Figure 4.6a and Figure 4.6b display the Ti 2p spectra, revealing distinct peaks at approximately 458 eV and 464 eV for Ti $2p_{3/2}$ and Ti $2p_{1/2}$, respectively. Notably, the Ti $2p_{3/2}$ peak exhibits a tail around 457 eV in the case of CTAB2-CsTO-700 (Figure 4.6b), indicative of the presence of Ti^{3+} species[146]. This suggests that the heat treatment at 700ºC for the CTAB1-CsTO sample leads to the reduction of titanium at the surface. The formation of oxygen vacancies on the surface can be caused by Ti^{3+} ions on

the surface as a result of the reduction of titanium. Surface oxygen vacancies can serve as active adsorption sites which is crucial in preventing the recombination of electron-hole pairs. This can improve the charge carrier separation and increase the photocatalytic activity. In the O 1s spectra, the primary peak at 530 eV is attributed to Ti-O-Ti bonding [147], while a slight shoulder at approximately 531 eV is often associated with the presence of surface-adsorbed hydroxyl groups, probably originating from water during the intercalation procedure or humidity. Figure 4.6e and Figure 4.6f depict peaks at around 738 eV and 724 eV for Cs $3d_{3/2}$ and Cs $3d_{1/2}$, respectively. It is noteworthy that both peaks exhibit a slight shift towards lower binding energies after CTAB intercalation into CsTO. This shift can be attributed to the incorporation of the CTAB cationic tail into the layers of the pristine titanate. In the pristine structure, Cs^+ ions reside within the interlayers of CsTO and can be easily removed or exchanged by processes such as liquid exfoliation or intercalation treatment. As the cationic tail of CTAB penetrates the layers, it can effectively remove Cs^+ ions from the structure. Consequently, the intensity of the Cs 3d peaks decreases after CTAB intercalation, as observed in Figure 4.6e. The Br 3d spectra, as shown in Figure 4.6g, exhibit a peak only for CTAB1-CsTO and CTAB2-CsTO samples. This peak is indicative of the anion part of CTAB. Significantly, this anionic component is no longer detected in the Br 3d spectra following heat treatment (Figure 4.6h), indicating that it does not remain within the structure after the heat treatment. For the same reasons, N 1s spectra also show similar results in Figure 4.6i. The observed peak around 402 eV is attributed to the nitrogen coming from the amine group (C-N) in the CTAB structure in CTAB1-CsTO and CTAB2-CsTO samples[148]. After the thermal treatment, in Figure 4.6j, the corresponding peak was not observed. In the C 1s spectra, in Figure 4.6k, the peak for CsTO was observed at 284.7 eV, which corresponds to C sp^2 – C sp^2 bonding. After the intercalation, the peak has shifted to higher binding energies around 285.9 eV for CTAB1-CsTO and CTAB2-CsTO attributed to C sp^2 - N bonding which is originating from the CTAB[149].

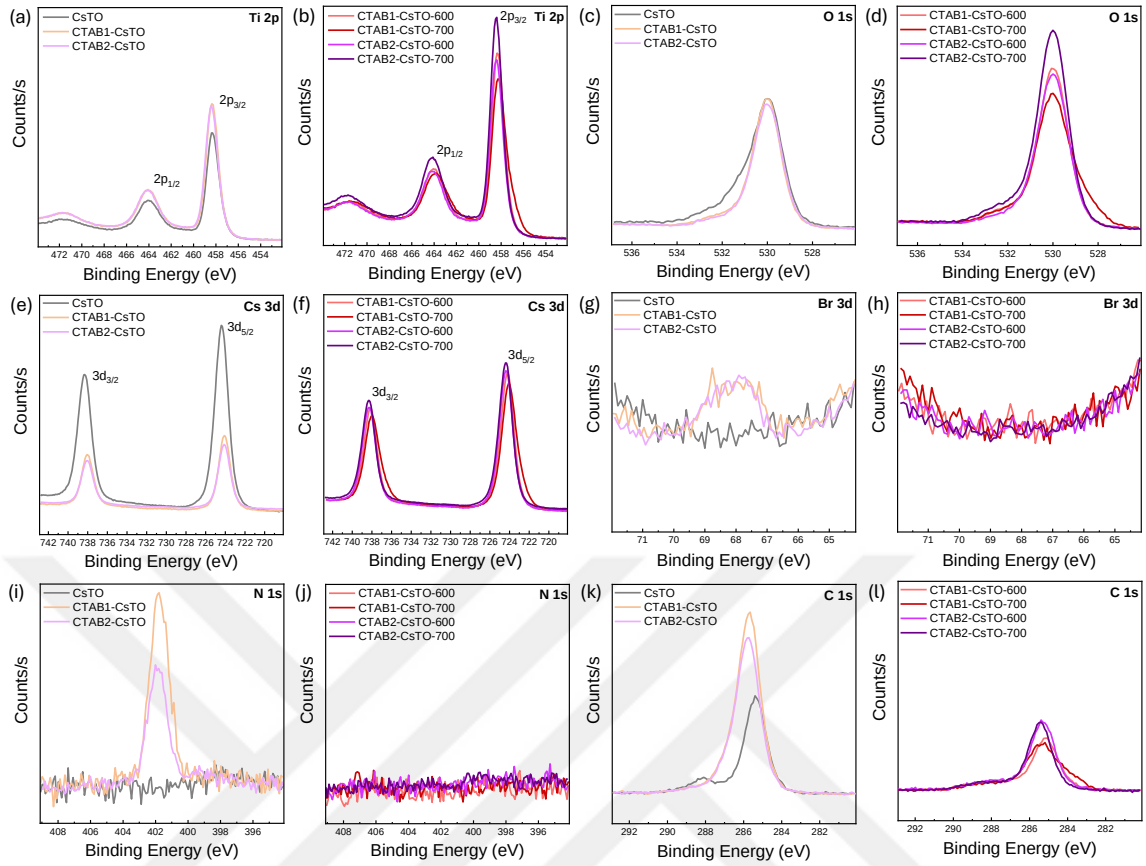

Figure 4.6. XPS spectra by comparison of pristine CsTO with CTAB intercalated and temperature effects for Ti 2p (a, b), O 1s (b, c), Cs 3d (c, d), Br 3d (g, h), N 1s (i, j), and C 1s (k, l).

Figure 4.7 presents scanning electron microscopy (SEM) images of the respective samples, revealing remarkable modifications in their morphology with the introduction of CTAB into the CsTO layers. The changes become particularly evident upon the introduction of CTAB into the layers of CsTO. The most notable changes are indicated in the form of reduced lateral dimensions and an expansion in surface area. The pristine CsTO initially exhibits a lateral size of nearly one micrometer. However, with the intercalation of CTAB, a substantial reduction in lateral size becomes apparent. Specifically, CTAB-treated samples, denoted as CTAB1-CsTO and CTAB2-CsTO, exhibit considerably fewer lateral dimensions, measuring approximately 400 nm, as exemplified in Figure 4.7d and Figure 4.7g. It is noteworthy that while the combined CTAB and heat treatments do not induce significant disruptions to the layered structure of CsTO, they cause substantial changes in lateral dimensions and the number of layers.

This transformation results in the development of smaller nanostructures. Such morphological modifications play a crucial role in enhancing photocatalytic activity. This enhancement can be attributed primarily to an increased active surface area facilitated by the expansion of interlayer distances and the partially exfoliated nature of the intercalated structures.

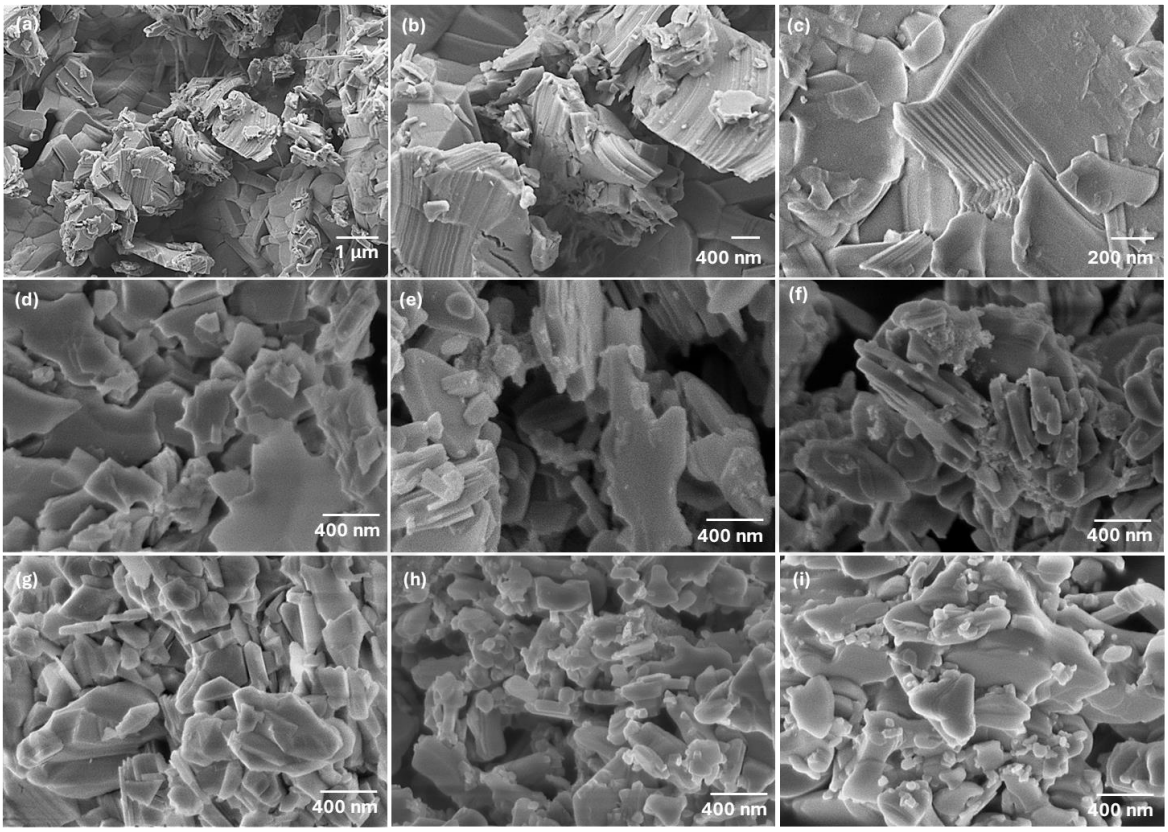

Figure 4.7. SEM images of pristine CsTO with different magnifications (a, b, c), CTAB1-CsTO (d), CTAB1-CsTO-600 (e), CTAB1-CsTO-700 (f), CTAB2-CsTO (g), CTAB2-CsTO-600 (h), and CTAB2-CsTO-700 (i).

The photocatalytic activity for the hydrogen evolution reaction was investigated for CTAB-intercalated samples, and the results are presented herein. In Figure 4.8a, it is evident that pristine CsTO exhibits weak photocatalytic activity with respect to hydrogen evolution via water splitting. However, as CTAB is intercalated into the CsTO structure, an increase in photocatalytic activity is observed. Notably, higher concentrations of

CTAB yield higher activity outcomes an elevated rate of hydrogen production. For instance, the CTAB1-CsTO sample shows the generation of approximately 3.2 micromoles of hydrogen, whereas the CTAB2-CsTO sample demonstrates 8.82 micromoles, nearly three times more hydrogen production compared to CTAB1-CsTO after six hours (Figure 4.8a). This correlation between CTAB concentration and photocatalytic activity can be attributed to the increment of the surface area, resulting in the creation of more active sites for the HER reaction to occur, which is consistent with previous results[150], [151]. Also, the light absorption characteristics of CTAB intercalated samples have changed to a better absorption range, which was shown with UV-Vis spectroscopy results in the previous section. Furthermore, the influence of heat treatment on photocatalytic activity is significant, resulting in hydrogen production levels of approximately 17.9 micromoles for CTAB1-CsTO-700 and 19.06 micromoles for CTAB2-CsTO-700 samples (Figure 4.8b). This effect may be attributed to a phase transition within the material, resulting in the transformation into anatase TiO_2 at 700°C, which aligns with findings obtained through Raman and XRD analyses. On the other hand, photoluminescence lifetime decay shows that the recombination of charge carriers is the slowest for CTAB2-CsTO-600 and CTAB2-CSTO-700 samples, which can explain the best activity observed. In Figure 4.8b, it was also presented that the activity increase is not only dependent on the thermal treatment with CsTO-600 and CsTO-700 samples since they did not show better activity than pristine CsTO.

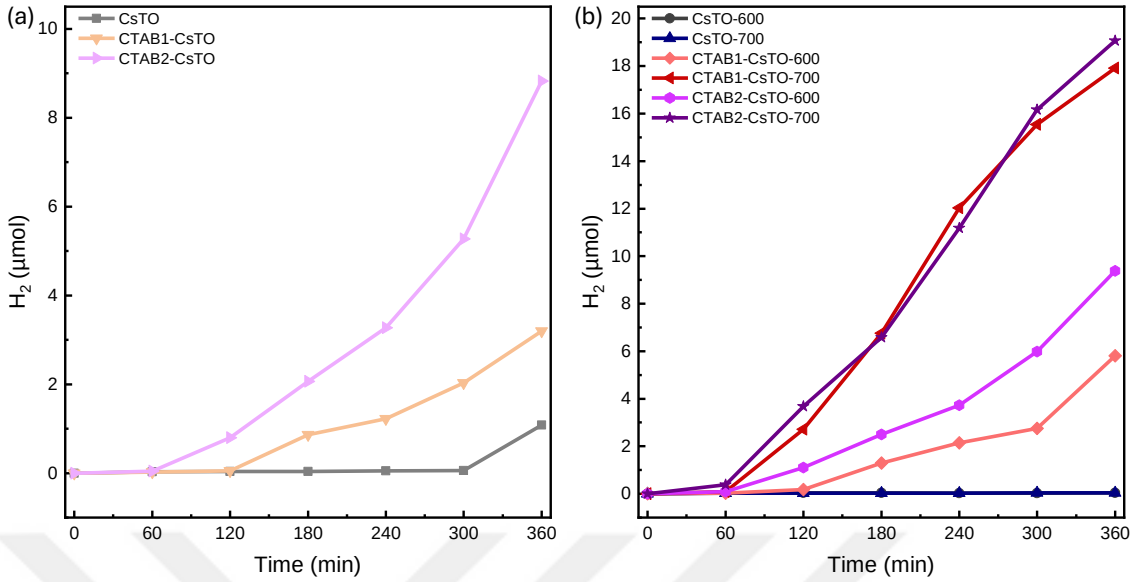

Figure 4.8. Photocatalytic activity comparison for hydrogen evolution by water splitting of CsTO and CTAB-intercalated samples (a) and after the thermal treatment at different temperatures (b).

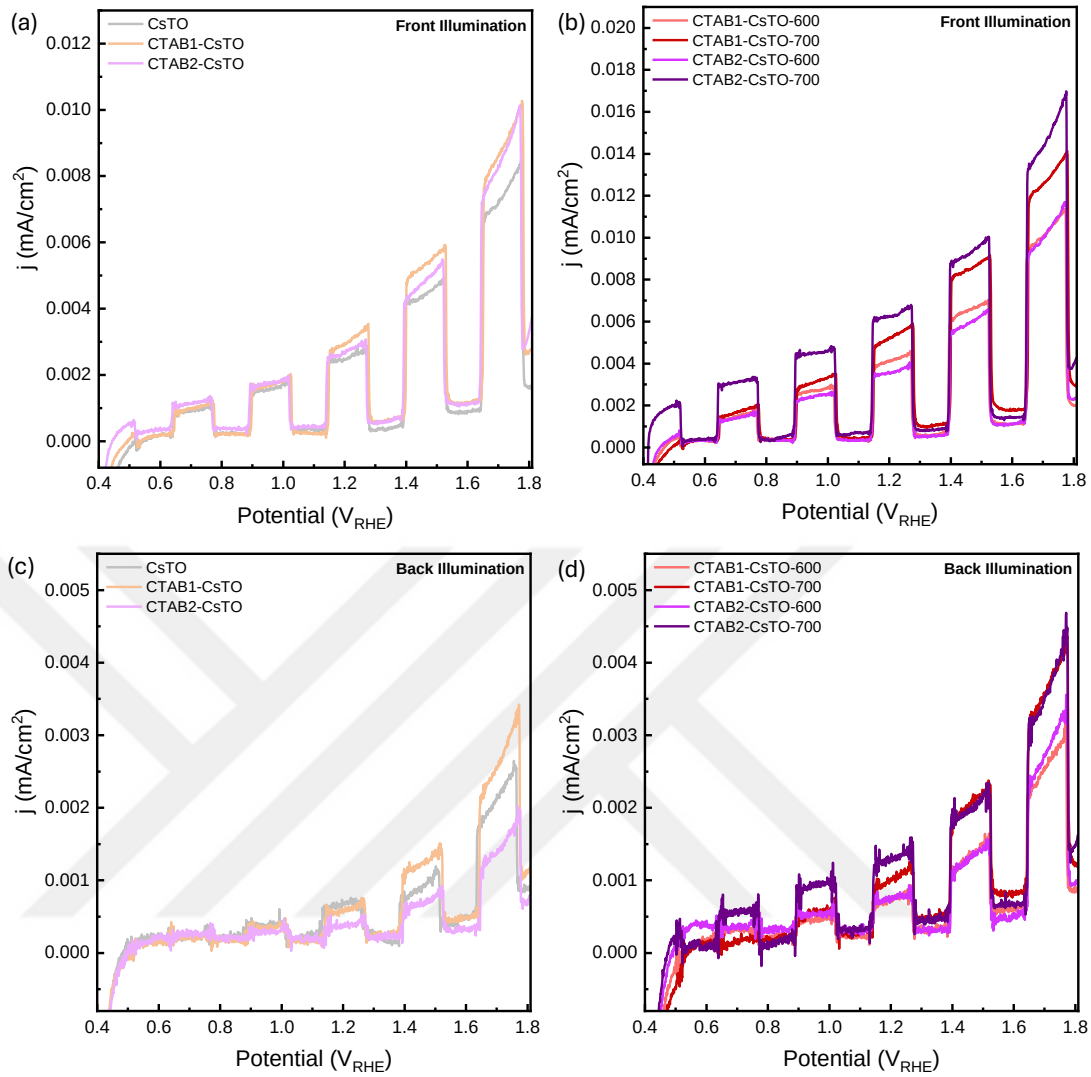

Figure 4.9. LSV measurements for CTAB-CsTO samples in 0.1 M Na_2SO_4 (pH=7) solution under the front (a), (b), and back (c), (d) illumination.

In Figure 4.9, the recorded LSV measurements reveal the photoelectrochemical activity for water oxidation within the CTAB intercalated CsTO samples. Remarkably, the trends observed in photocurrent align closely with the results obtained from the photocatalytic activity experiments, consistently signifying that the intercalation of CTAB species into the interlayer regions of CsTO improves its catalytic activity. Additionally, in the context of photoelectrochemical analyses, a carbonaceous layer formed from CTAB may establish an additional conductive layer. This is particularly evident in Figure 4.9b and Figure 4.9d, where it becomes apparent that the CTAB2-CsTO-700 sample exhibits the highest level of activity. This result is in agreement with

UV-Vis adsorption spectroscopy and PL lifetime decay results. The relatively low photocurrent density exhibited by the pristine CsTO sample can be attributed to its as-prepared layered structure. This arrangement tends to limit the incident light intensity reaching the active sites and consequently reduces the available surface area for catalytic reactions. Furthermore, it is plausible that the CsTO layers may undergo agglomeration on the electrode surface, further diminishing the effective surface area for the reaction. In terms of decreasing electron−hole recombination on the surface of titanate, the CTAB between the interlayer plays a significant role. With the introduction of CTAB into the CsTO structure, an increase in the interlayer distance of the pristine CsTO layers is observed. This is corroborated by the SEM images, which confirm an expansion in surface area. The observed effect of temperature on the photoelectrochemical measurements is similar to the trends observed in the photocatalytic results, reinforcing the influence of temperature on the overall catalytic behavior.

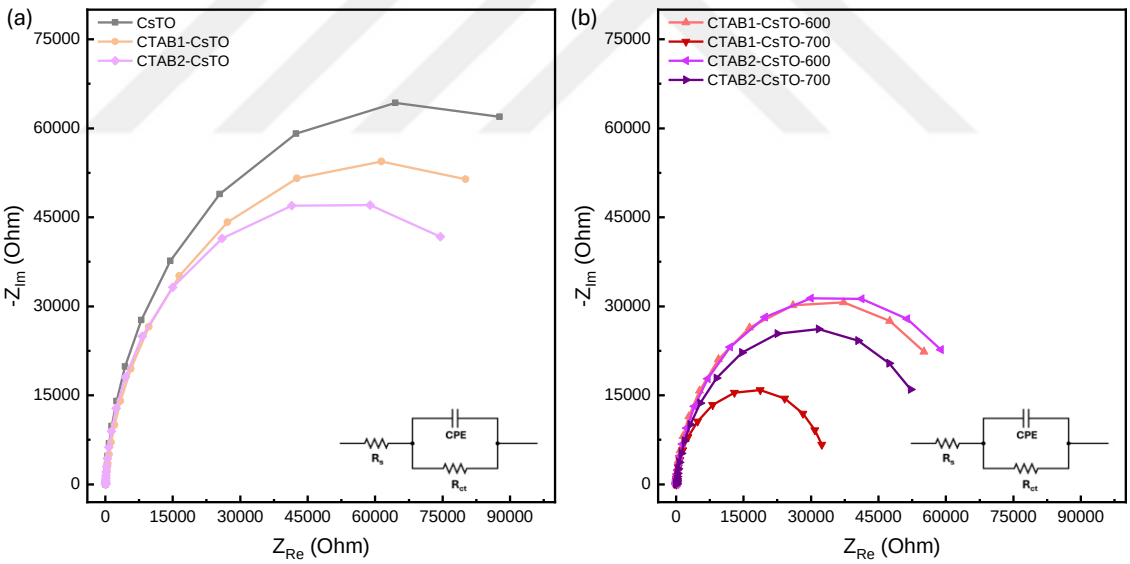

Figure 4.10. EIS Measurement of pristine CsTO and CTAB treated samples (a), and after heat treatment at different temperatures (b) at 1.8 VRHE in 0.1 M Na_2SO_4 at pH=7, Randle's model used, and it is shown as an inset.

The Nyquist plot corresponds to EIS measurements, as shown in Figure 4.10. Electrochemical impedance spectroscopy measurements were done to understand the

capacitive behavior of the samples, and it is plotted as its imaginary and real parts, which is attributed as the Nyquist plot. Fitting was done by using Randle's model with a constant phase element, and it is shown in Figure 4.10b as an inset. R_s is the resistance of the electrolyte; the constant phase element corresponds to the capacitance between the electrolyte and the electrode, and R_{ct} is the charge transfer resistance. Instead of an ideal capacitor, CPE was used in this model due to the inhomogeneity surface of the prepared photoelectrodes, electrode porosity, or the roughness of the surface.

The EIS results show almost the same trend as LSV measurement results. While pristine CsTO shows 138227 Ω charge transfer resistance, CTAB intercalation is decreasing the R_{ct} values to 122255 Ω and 100891 Ω for CTAB1-CsTO and CTAB2-CsTO, respectively. Heat treatment at 600ºC and 700ºC decreases R_{ct} further. CTAB1-CsTO-700 has the smallest R_{ct} value, 34276 Ω. CTAB2-CsTO-700 R_{ct} is 59190 Ω. The outcomes of the EIS closely match those of the LSV measurements. The R_{ct} of pristine CsTO is 138227 Ω. However, R_{ct} values are considerably decreased as a result of CTAB intercalation, with values of 122255 Ω and 100891 Ω for CTAB1-CsTO and CTAB2-CsTO, respectively. The R_{ct} for both samples is further decreased by further heat treatment at 600ºC and 700ºC. Surprisingly, CTAB1-CsTO-700 has the lowest R_{ct} value, which is 34276 Ω, whereas CTAB2-CsTO-700 has a little higher R_{ct} value, which is 59190 Ω. Notably, since the CTAB1-CsTO-700 sample has the lowest R_{ct} among other samples, it stands out as having a unique electrochemical behavior even if the CTAB2-CsTO-700 sample produces the maximum photocurrent.

4.4 Conclusion

In this chapter, the photocatalytic and photoelectrochemical activities of cetyltrimethylammonium bromide (CTAB) intercalated layered cesium titanate (CsTO) were investigated through structural and photochemical characterizations. The interlayer spacing between CsTO layers expands by the presence of an alkyl chain of CTAB, which results in CsTO results in morphological changes and a larger surface area. The treatment induced an ion exchange mechanism, removing Cs^+ ions as CTAB penetrates the layers. The introduction of CTAB enhanced the photocatalytic performance for hydrogen evolution reactions by approximately three times more than pristine CsTO. Furthermore, changing the annealing temperature increased the quantity of generated hydrogen due to surface modifications. High carbon content species impact charge carrier processes and serve as a conductive layer for photoelectrochemical performances. Thermal treatment caused structure modifications and titanium reduction on the surface. The LSV measurements carried out with photoanode films for the OER indicated a similar pattern, indicating improved activity with higher CTAB concentrations, which is consistent with the photocatalytic HER results. A comprehensive understanding of the surface charge carrier dynamics can be carried out for the corresponding samples through the application of wider electrochemical tests.

Chapter 5:
CONCLUSION

With an emphasis on alterations involving the addition of single Sn atoms by photo-deposition with photoactive properties, it was used exfoliation and ion exchange techniques in the first part of this research to unleash the potential of layered titanates. It was established the exfoliation process, which resulted in an increased interlayer space within the titanate structure. The photocatalytic hydrogen evolution reaction, which exfoliated titanate excelled at, and its photocatalytic abilities were further increased by the addition of an optimal amount of Sn single atoms to its surface, leading to a significant improvement in performance over the original exfoliated titanate.

In the second part of this study, the photocatalytic and photoelectrochemical properties of layered cesium titanate (CsTO) intercalated with cetyltrimethylammonium bromide (CTAB) was examined. The addition of CTAB changed the interlayer spacing of CsTO, giving the substance morphological changes and an increased surface area. The CTAB intercalation caused an ion exchange process, which led to the evacuation of Cs^+ ions from the layer structure. In comparison to pristine CsTO, improvements in photocatalytic efficiency for hydrogen generation were observed for CTAB-intercalated samples. Additionally, different annealing temperatures affected how much hydrogen was produced as a result of surface alterations. Carbon-rich species affected charge carrier processes and improved photoelectrochemical performance. Additionally, structural changes were brought about by heat treatment, along with a reduction in titanium at the surface.

Layered titanates with different cations and structures were investigated in this study for mainly photochemical applications but also photoelectrochemical mechanisms. It is discernible that their morphology and electronic structures can be tuned efficiently. The possibility of exploring surface charge carrier dynamics of layered titanates further, as was investigated in these chapters, can be emphasized. Future investigations might focus on using a wider variety of electrochemical experiments to clarify the complex mechanisms driving charge transport. For the design and improvement of intercalated layered titanates, not only in the context of photocatalytic hydrogen generation but also in a variety of other applications that profit from improved material performance, this better knowledge offers enormous promise.

Chapter 6:

REFERENCES

[1] J. Zhang, Q. Zhang, and X. Feng, “Support and Interface Effects in Water-Splitting Electrocatalysts,” *Adv. Mater.*, vol. 31, no. 31, p. 1808167, 2019, doi: 10.1002/adma.201808167.

[2] X. Li, J. Yu, J. Low, Y. Fang, J. Xiao, and X. Chen, “Engineering heterogeneous semiconductors for solar water splitting,” *J. Mater. Chem. A*, vol. 3, no. 6, pp. 2485–2534, 2015, doi: 10.1039/C4TA04461D.

[3] S. Chen, T. Takata, and K. Domen, “Particulate photocatalysts for overall water splitting,” *Nat. Rev. Mater.*, vol. 2, no. 10, Art. no. 10, Aug. 2017, doi: 10.1038/natrevmats.2017.50.

[4] I. Roger, M. A. Shipman, and M. D. Symes, “Earth-abundant catalysts for electrochemical and photoelectrochemical water splitting,” *Nat. Rev. Chem.*, vol. 1, no. 1, Art. no. 1, Jan. 2017, doi: 10.1038/s41570-016-0003.

[5] Q. Zhu, Z. Xu, B. Qiu, M. Xing, and J. Zhang, “Emerging Cocatalysts on g-C3N4 for Photocatalytic Hydrogen Evolution,” *Small*, vol. 17, no. 40, p. 2101070, 2021, doi: 10.1002/smll.202101070.

[6] T. Hisatomi, J. Kubota, and K. Domen, “Recent advances in semiconductors for photocatalytic and photoelectrochemical water splitting,” *Chem. Soc. Rev.*, vol. 43, no. 22, pp. 7520–7535, Oct. 2014, doi: 10.1039/C3CS60378D.

[7] P. Chatterjee *et al.*, “Photovoltaic/photo-electrocatalysis integration for green hydrogen: A review,” *Energy Convers. Manag.*, vol. 261, p. 115648, Jun. 2022, doi: 10.1016/j.enconman.2022.115648.

[8] Z. Wang, C. Li, and K. Domen, “Recent developments in heterogeneous photocatalysts for solar-driven overall water splitting,” *Chem. Soc. Rev.*, vol. 48, no. 7, pp. 2109–2125, 2019, doi: 10.1039/C8CS00542G.

[9] F. E. Osterloh and B. A. Parkinson, “Recent developments in solar water-splitting photocatalysis,” *MRS Bull.*, vol. 36, no. 1, pp. 17–22, Jan. 2011, doi: 10.1557/mrs.2010.5.

[10] A. Kudo and Y. Miseki, “Heterogeneous photocatalyst materials for water splitting,” *Chem. Soc. Rev.*, vol. 38, no. 1, pp. 253–278, Dec. 2008, doi: 10.1039/B800489G.

[11] K. Maeda and K. Domen, “Photocatalytic Water Splitting: Recent Progress and Future Challenges,” *J. Phys. Chem. Lett.*, vol. 1, no. 18, pp. 2655–2661, Sep. 2010, doi: 10.1021/jz1007966.

[12] K. Maeda, “Photocatalytic water splitting using semiconductor particles: History and recent developments,” *J. Photochem. Photobiol. C Photochem. Rev.*, vol. 12, no. 4, pp. 237–268, Dec. 2011, doi: 10.1016/j.jphotochemrev.2011.07.001.

[13] R. Li and C. Li, “Chapter One - Photocatalytic Water Splitting on Semiconductor-Based Photocatalysts,” in *Advances in Catalysis*, C. Song, Ed., Academic Press, 2017, pp. 1–57. doi: 10.1016/bs.acat.2017.09.001.

[14] J. Kosco *et al.*, “Enhanced photocatalytic hydrogen evolution from organic semiconductor heterojunction nanoparticles,” *Nat. Mater.*, vol. 19, no. 5, Art. no. 5, May 2020, doi: 10.1038/s41563-019-0591-1.

[15] W. Zhao *et al.*, “Recent advances in photocatalytic hydrogen evolution with high-performance catalysts without precious metals,” *Renew. Sustain. Energy Rev.*, vol. 132, p. 110040, Oct. 2020, doi: 10.1016/j.rser.2020.110040.

[16] A. A. Ismail and D. W. Bahnemann, “Photochemical splitting of water for hydrogen production by photocatalysis: A review,” *Sol. Energy Mater. Sol. Cells*, vol. 128, pp. 85–101, Sep. 2014, doi: 10.1016/j.solmat.2014.04.037.
[17] S. Rajak, N.-N. Vu, P. Kaur, A. Duong, and P. Nguyen-Tri, “Recent progress on the design and development of diaminotriazine based molecular catalysts for light-driven hydrogen production,” *Coord. Chem. Rev.*, vol. 456, p. 214375, Apr. 2022, doi: 10.1016/j.ccr.2021.214375.
[18] C.-Y. Peng, L. Kang, S. Cao, Y. Chen, Z.-S. Lin, and W.-F. Fu, “Nanostructured Ni2P as a Robust Catalyst for the Hydrolytic Dehydrogenation of Ammonia–Borane,” *Angew. Chem.*, vol. 127, no. 52, pp. 15951–15955, 2015, doi: 10.1002/ange.201508113.
[19] V. I. Simagina *et al.*, “TiO2-based photocatalysts for controllable hydrogen evolution from ammonia borane,” *Catal. Today*, vol. 379, pp. 149–158, Nov. 2021, doi: 10.1016/j.cattod.2020.04.070.
[20] P. Xu, W. Lu, J. Zhang, and L. Zhang, “Efficient Hydrolysis of Ammonia Borane for Hydrogen Evolution Catalyzed by Plasmonic Ag@Pd Core–Shell Nanocubes,” *ACS Sustain. Chem. Eng.*, vol. 8, no. 33, pp. 12366–12377, Aug. 2020, doi: 10.1021/acssuschemeng.0c02276.
[21] J. Joy, J. Mathew, and S. C. George, “Nanomaterials for photoelectrochemical water splitting – review,” *Int. J. Hydrog. Energy*, vol. 43, no. 10, pp. 4804–4817, Mar. 2018, doi: 10.1016/j.ijhydene.2018.01.099.
[22] M. A. Marwat *et al.*, “Advanced Catalysts for Photoelectrochemical Water Splitting,” *ACS Appl. Energy Mater.*, vol. 4, no. 11, pp. 12007–12031, Nov. 2021, doi: 10.1021/acsaem.1c02548.
[23] E. Samuel, B. Joshi, M.-W. Kim, M. T. Swihart, and S. S. Yoon, “Morphology engineering of photoelectrodes for efficient photoelectrochemical water splitting,” *Nano Energy*, vol. 72, p. 104648, Jun. 2020, doi: 10.1016/j.nanoen.2020.104648.
[24] J. W. Ager, M. R. Shaner, K. A. Walczak, I. D. Sharp, and S. Ardo, “Experimental demonstrations of spontaneous, solar-driven photoelectrochemical water splitting,” *Energy Environ. Sci.*, vol. 8, no. 10, pp. 2811–2824, 2015, doi: 10.1039/C5EE00457H.
[25] L. Jin, H. Zhao, Z. M. Wang, and F. Rosei, “Quantum Dots-Based Photoelectrochemical Hydrogen Evolution from Water Splitting,” *Adv. Energy Mater.*, vol. 11, no. 12, p. 2003233, 2021, doi: 10.1002/aenm.202003233.
[26] J. Qi, W. Zhang, and R. Cao, “Solar-to-Hydrogen Energy Conversion Based on Water Splitting,” *Adv. Energy Mater.*, vol. 8, no. 5, p. 1701620, 2018, doi: 10.1002/aenm.201701620.
[27] G. Liu *et al.*, “Promoting Active Species Generation by Plasmon-Induced Hot-Electron Excitation for Efficient Electrocatalytic Oxygen Evolution,” *J. Am. Chem. Soc.*, vol. 138, no. 29, pp. 9128–9136, Jul. 2016, doi: 10.1021/jacs.6b05190.
[28] G. Dong, L. Yan, and Y. Bi, “Advanced oxygen evolution reaction catalysts for solar-driven photoelectrochemical water splitting,” *J. Mater. Chem. A*, vol. 11, no. 8, pp. 3888–3903, Feb. 2023, doi: 10.1039/D2TA09479G.
[29] P. Zhang, L. Yu, and X. W. (David) Lou, “Construction of Heterostructured Fe2O3-TiO2 Microdumbbells for Photoelectrochemical Water Oxidation,” *Angew. Chem.*, vol. 130, no. 46, pp. 15296–15300, 2018, doi: 10.1002/ange.201808104.

[30] C. Acar, I. Dincer, and C. Zamfirescu, “A review on selected heterogeneous photocatalysts for hydrogen production,” *Int. J. Energy Res.*, vol. 38, no. 15, pp. 1903–1920, 2014, doi: 10.1002/er.3211.
[31] J. E. S. Haggerty *et al.*, “High-fraction brookite films from amorphous precursors,” *Sci. Rep.*, vol. 7, no. 1, Art. no. 1, Nov. 2017, doi: 10.1038/s41598-017-15364-y.
[32] C. Luo, X. Ren, Z. Dai, Y. Zhang, X. Qi, and C. Pan, “Present Perspectives of Advanced Characterization Techniques in TiO2-Based Photocatalysts,” *ACS Appl. Mater. Interfaces*, vol. 9, no. 28, pp. 23265–23286, Jul. 2017, doi: 10.1021/acsami.7b00496.
[33] M. Ogawa, M. Morita, S. Igarashi, and S. Sato, “A green synthesis of a layered titanate, potassium lithium titanate; lower temperature solid-state reaction and improved materials performance,” *J. Solid State Chem.*, vol. 206, pp. 9–13, Oct. 2013, doi: 10.1016/j.jssc.2013.07.020.
[34] T.-H. Kim, I.-T. Hong, J.-Y. Lee, J.-H. Kang, and J.-M. Oh, “Layered Nanomaterials for Environmental Remediation Applications,” *Energy Environ. Focus*, vol. 3, no. 1, pp. 23–36, Mar. 2014, doi: 10.1166/eef.2014.1087.
[35] X. Sun *et al.*, “Photocatalytic Hydrogen Production over Chromium Doped Layered Perovskite Sr2TiO4,” *Inorg. Chem.*, vol. 54, no. 15, pp. 7445–7453, Aug. 2015, doi: 10.1021/acs.inorgchem.5b01042.
[36] W. Soontornchaiyakul, T. Fujimura, N. Yano, Y. Kataoka, and R. Sasai, “Photocatalytic Hydrogen Evolution over Exfoliated Rh-Doped Titanate Nanosheets,” *ACS Omega*, vol. 5, no. 17, pp. 9929–9936, May 2020, doi: 10.1021/acsomega.0c00204.
[37] L. Cui *et al.*, “Confined Synthesis: From Layered Titanate to Highly Efficient and Durable Mesoporous Cu/TiO2 Hydrogen Evolution Photocatalysts,” *ACS Appl. Energy Mater.*, vol. 4, no. 4, pp. 4050–4058, Apr. 2021, doi: 10.1021/acsaem.1c00407.
[38] T. K. Saothayanun, T. T. Sirinakorn, and M. Ogawa, “Layered alkali titanates (A2TinO2n+1): possible uses for energy/environment issues,” *Front. Energy*, vol. 15, no. 3, pp. 631–655, Sep. 2021, doi: 10.1007/s11708-021-0776-6.
[39] T. (Tip) Sirinakorn, T. (Ko) Saothayanun, D. (Ammy) Sruamsiri, and M. Ogawa, “Post-synthetic particle size reduction of a layered cesium titanate (Cs2Ti5O11) for the improvement of photocatalytic H2 production,” *J. Phys. Chem. Solids*, vol. 163, p. 110541, Apr. 2022, doi: 10.1016/j.jpcs.2021.110541.
[40] Z. Wu *et al.*, “Optimized Pt Single Atom Harvesting on TiO2 Nanotubes—Towards a Most Efficient Photocatalyst,” *Small*, vol. 18, no. 2, p. 2104892, 2022, doi: 10.1002/smll.202104892.
[41] H. Zhao, Q. Mao, L. Jian, Y. Dong, and Y. Zhu, “Photodeposition of earth-abundant cocatalysts in photocatalytic water splitting: Methods, functions, and mechanisms,” *Chin. J. Catal.*, vol. 43, no. 7, pp. 1774–1804, Jul. 2022, doi: 10.1016/S1872-2067(22)64105-6.
[42] H. M. McNair, J. M. Miller, and N. H. Snow, “Basic Gas Chromatography”.
[43] *Detectors in Gas Chromatography*. Elsevier, 2011.
[44] C. F. Poole, “GAS CHROMATOGRAPHY | Detectors,” in *Encyclopedia of Analytical Science (Second Edition)*, P. Worsfold, A. Townshend, and C. Poole, Eds., Oxford: Elsevier, 2005, pp. 95–105. doi: 10.1016/B0-12-369397-7/00222-3.
[45] E. Usman, M. Barzgar Vishlaghi, A. Kahraman, N. Solati, and S. Kaya, “Modifying the Electron-Trapping Process at the BiVO4 Surface States via the

TiO2 Overlayer for Enhanced Water Oxidation," *ACS Appl. Mater. Interfaces*, vol. 13, no. 50, pp. 60602–60611, Dec. 2021, doi: 10.1021/acsami.1c16847.

[46] D. D. Macdonald, "Reflections on the history of electrochemical impedance spectroscopy," *Electrochimica Acta*, vol. 51, no. 8, pp. 1376–1388, Jan. 2006, doi: 10.1016/j.electacta.2005.02.107.

[47] Q. Han, Y. Yang, J. Zhang, and B. Dong, "Electrochemical characterization of chloride ion transport in rubber concrete," *J. Build. Eng.*, vol. 73, p. 106658, Aug. 2023, doi: 10.1016/j.jobe.2023.106658.

[48] M. Labib, E. H. Sargent, and S. O. Kelley, "Electrochemical Methods for the Analysis of Clinically Relevant Biomolecules," *Chem. Rev.*, vol. 116, no. 16, pp. 9001–9090, Aug. 2016, doi: 10.1021/acs.chemrev.6b00220.

[49] A. A. Bunaciu, E. gabriela Udriştioiu, and H. Y. Aboul-Enein, "X-Ray Diffraction: Instrumentation and Applications," *Crit. Rev. Anal. Chem.*, vol. 45, no. 4, pp. 289–299, Oct. 2015, doi: 10.1080/10408347.2014.949616.

[50] L. D. Whittig and W. R. Allardice, "X-Ray Diffraction Techniques," in *Methods of Soil Analysis*, John Wiley & Sons, Ltd, 1986, pp. 331–362. doi: 10.2136/sssabookser5.1.2ed.c12.

[51] H. Stanjek and W. Häusler, "Basics of X-ray Diffraction," *Hyperfine Interact.*, vol. 154, no. 1, pp. 107–119, Jun. 2004, doi: 10.1023/B:HYPE.0000032028.60546.38.

[52] C. S. Fadley, "X-ray photoelectron spectroscopy: Progress and perspectives," *J. Electron Spectrosc. Relat. Phenom.*, vol. 178–179, pp. 2–32, May 2010, doi: 10.1016/j.elspec.2010.01.006.

[53] F. A. Stevie and C. L. Donley, "Introduction to x-ray photoelectron spectroscopy," *J. Vac. Sci. Technol. A*, vol. 38, no. 6, p. 063204, Sep. 2020, doi: 10.1116/6.0000412.

[54] S. P. Mulvaney and C. D. Keating, "Raman Spectroscopy," *Anal. Chem.*, vol. 72, no. 12, pp. 145–158, Jun. 2000, doi: 10.1021/a10000155.

[55] S. Perkowitz, *Optical characterization of semiconductors: infrared, Raman, and photoluminescence spectroscopy*. in Techniques of physics, no. 14. London ; San Diego: Academic Press, 1993.

[56] R. S. Das and Y. K. Agrawal, "Raman spectroscopy: Recent advancements, techniques and applications," *Vib. Spectrosc.*, vol. 57, no. 2, pp. 163–176, Nov. 2011, doi: 10.1016/j.vibspec.2011.08.003.

[57] C. Berthomieu and R. Hienerwadel, "Fourier transform infrared (FTIR) spectroscopy," *Photosynth. Res.*, vol. 101, no. 2, pp. 157–170, Sep. 2009, doi: 10.1007/s11120-009-9439-x.

[58] F. S. Rocha, A. J. Gomes, C. N. Lunardi, S. Kaliaguine, and G. S. Patience, "Experimental methods in chemical engineering: Ultraviolet visible spectroscopy—UV-Vis," *Can. J. Chem. Eng.*, vol. 96, no. 12, pp. 2512–2517, 2018, doi: 10.1002/cjce.23344.

[59] Q. Li, M. Anpo, and X. Wang, "Application of photoluminescence spectroscopy to elucidate photocatalytic reactions at the molecular level," *Res. Chem. Intermed.*, vol. 46, no. 10, pp. 4325–4344, Oct. 2020, doi: 10.1007/s11164-020-04209-5.

[60] G. D. Gilliland, "Photoluminescence spectroscopy of crystalline semiconductors," *Mater. Sci. Eng. R Rep.*, vol. 18, no. 3, pp. 99–399, Mar. 1997, doi: 10.1016/S0927-796X(97)80003-4.

[61] I. E. Wachs and M. A. Bañares, Eds., *Springer Handbook of Advanced Catalyst Characterization*. in Springer Handbooks. Cham: Springer International Publishing, 2023. doi: 10.1007/978-3-031-07125-6.

[62] "SEM vs TEM," *Analysis & Separations from Technology Networks*. http://www.technologynetworks.com/analysis/articles/sem-vs-tem-331262 (accessed Aug. 11, 2023).
[63] J. M. Zuo and J. C. H. Spence, *Advanced Transmission Electron Microscopy*. New York, NY: Springer New York, 2017. doi: 10.1007/978-1-4939-6607-3.
[64] G. Luderer *et al.*, "Impact of declining renewable energy costs on electrification in low-emission scenarios," *Nat. Energy*, vol. 7, no. 1, Art. no. 1, Jan. 2022, doi: 10.1038/s41560-021-00937-z.
[65] A. Fujishima and K. Honda, "Electrochemical photolysis of water at a semiconductor electrode," *Nature*, vol. 238, no. 5358, pp. 37–38, 1972, doi: 10.1038/238037a0.
[66] F. Fu *et al.*, "Highly selective and sharp volcano-type synergistic Ni2Pt@ZIF-8-catalyzed hydrogen evolution from ammonia borane hydrolysis," *J. Am. Chem. Soc.*, vol. 140, no. 31, pp. 10034–10042, 2018, doi: 10.1021/jacs.8b06511.
[67] X. Liu *et al.*, "Self-powered H2 production with bifunctional hydrazine as sole consumable," *Nat. Commun.*, vol. 9, no. 1, p. 4365, 2018, doi: 10.1038/s41467-018-06815-9.
[68] Y. Lin *et al.*, "Boosted reactivity of ammonia borane dehydrogenation over Ni/Ni2P heterostructure," *J. Phys. Chem. Lett.*, vol. 10, no. 5, pp. 1048–1054, 2019, doi: 10.1021/acs.jpclett.9b00122.
[69] Y. Shang and R. Chen, "Semiempirical hydrogen generation model using concentrated sodium borohydride solution," *Energy Fuels*, vol. 20, no. 5, pp. 2149–2154, 2006, doi: 10.1021/ef050380f.
[70] Y. Wang and X. Liu, "Catalytic hydrolysis of sodium borohydride for hydrogen production using Magnetic recyclable CoFe2O4-modified transition-metal nanoparticles," *ACS Appl. Nano Mater.*, vol. 4, no. 10, pp. 11312–11320, 2021, doi: 10.1021/acsanm.1c03067.
[71] E. Doustkhah *et al.*, "Templated synthesis of atomically-thin Ag nanocrystal catalysts in the interstitial space of a layered silicate," *Chem. Commun.*, vol. 54, no. 35, pp. 4402-4405, 2018, doi: 10.1039/C8CC00275D.
[72] Q. Zhu, Y. Qu, D. Liu, K. W. Ng, and H. Pan, "Two-dimensional layered materials: high-efficient electrocatalysts for hydrogen evolution reaction," *ACS Appl. Nano Mater.*, vol. 3, no. 7, pp. 6270–6296, 2020, doi: 10.1021/acsanm.0c01331.
[73] Y. Ai, W. Li, and D. Zhao, "2D mesoporous materials," *Natl. Sci. Rev.*, vol. 9, no. 5, 2021, doi: 10.1093/nsr/nwab108.
[74] A. Splendiani *et al.*, "Emerging photoluminescence in monolayer MoS2," *Nano Lett.*, vol. 10, no. 4, pp. 1271–1275, 2010, doi: 10.1021/nl903868w.
[75] W. Li, X. Qian, and J. Li, "Phase transitions in 2D materials," *Nat. Rev. Mater.*, vol. 6, no. 9, pp. 829–846, 2021, doi: 10.1038/s41578-021-00304-0.
[76] K. Saito *et al.*, "Lepidocrocite-Type Layered Titanate Nanoparticles as Photocatalysts for H_2 Production," *ACS Appl. Nano Mater.*, vol. 5, no. 7, pp. 9053–9062, Jul. 2022, doi: 10.1021/acsanm.2c01353.
[77] M. Pilarski, R. Marschall, S. Gross, and M. Wark, "Layered cesium copper titanate for photocatalytic hydrogen production," *Appl. Catal. B Environ.*, vol. 227, pp. 349–355, Jul. 2018, doi: 10.1016/j.apcatb.2018.01.039.
[78] M. Matsuoka, Y. Ide, and M. Ogawa, "Temperature-dependent photocatalytic hydrogen evolution activity from water on a dye-sensitized layered titanate," *Phys.*

Chem. Chem. Phys., vol. 16, no. 8, pp. 3520-3522, 2014, doi: 10.1039/C3CP55213F.

[79] G. Liu *et al.*, "Band-to-Band Visible-Light Photon Excitation and Photoactivity Induced by Homogeneous Nitrogen Doping in Layered Titanates," *Chem. Mater.*, vol. 21, no. 7, pp. 1266–1274, Apr. 2009, doi: 10.1021/cm802986r.

[80] A. Kudo and T. Kondo, "Photoluminescent and photocatalytic properties of layered caesium titanates, Cs2TinO2n+1 (n=2, 5, 6)," *J. Mater. Chem.*, vol. 7, no. 5, pp. 777–780, 1997, doi: 10.1039/a606297k.

[81] Y. Ide, Y. Nakasato, and M. Ogawa, "Molecular recognitive photocatalysis driven by the selective adsorption on layered titanates," *J. Am. Chem. Soc.*, vol. 132, no. 10, pp. 3601–3604, 2010, doi: 10.1021/ja910591v.

[82] T. W. Kim *et al.*, "Mesoporous Iron Oxide-Layered Titanate Nanohybrids: Soft-Chemical Synthesis, Characterization, and Photocatalyst Application," *J. Phys. Chem. C*, vol. 112, no. 38, pp. 14853–14862, Sep. 2008, doi: 10.1021/jp805488h.

[83] Y. Ide, W. Shirae, T. Takei, D. Mani, and J. Henzie, "Merging cation exchange and photocatalytic charge separation efficiency in an anatase/K2Ti4O9 nanobelt heterostructure for metal ions fixation," *Inorg. Chem.*, vol. 57, no. 10, pp. 6045–6050, 2018, doi: 10.1021/acs.inorgchem.8b00538.

[84] K. Saito, S. Tominaka, S. Yoshihara, K. Ohara, Y. Sugahara, and Y. Ide, "Room-temperature rutile TiO2 nanoparticle formation on protonated layered titanate for high-performance heterojunction creation," *ACS Appl. Mater. Interfaces*, vol. 9, no. 29, pp. 24538–24544, 2017, doi: 10.1021/acsami.7b04051.

[85] A. K. Yousef, M. Sanad, M. M. Rashad, A.-A. Y. El-Sayed, and Y. Ide, "Facile synthesis of layered titanate/rutile heterojunction photocatalysts," *Bull. Chem. Soc. Jpn.*, vol. 92, no. 11, pp. 1801–1806, 2019, doi: 10.1246/bcsj.20190180.

[86] T. Gao, H. Fjellvåg, and P. Norby, "Defect chemistry of a zinc-doped lepidocrocite titanate CsxTi2−x/2Znx/2O4 (x = 0.7) and its protonic Form," *Chem. Mater.*, vol. 21, no. 15, pp. 3503–3513, 2009, doi: 10.1021/cm901329g.

[87] S. Kang *et al.*, "Ordering of a nanoconfined water network around zinc ions induces high proton conductivity in layered titanate," *Chem. Mater.*, vol. 34, no. 9, pp. 3967–3975, 2022, doi: 10.1021/acs.chemmater.1c04421.

[88] S. Ida *et al.*, "Photoluminescence spectral change in layered titanate oxide Intercalated with hydrated Eu3+," *J. Phys. Chem. B*, vol. 110, no. 47, pp. 23881–23887, 2006, doi: 10.1021/jp063412o.

[89] A. Riss, T. Berger, H. Grothe, J. Bernardi, O. Diwald, and E. Knözinger, "Chemical Control of Photoexcited States in Titanate Nanostructures," *Nano Lett.*, vol. 7, no. 2, pp. 433–438, Feb. 2007, doi: 10.1021/nl062699y.

[90] S. Kang *et al.*, "Hydronium Ions Stabilized in a Titanate-Layered Structure with High Ionic Conductivity: Application to Aqueous Proton Batteries," *Chem. Mater.*, vol. 32, no. 21, pp. 9458–9469, Nov. 2020, doi: 10.1021/acs.chemmater.0c03658.

[91] T. Sasaki and M. Watanabe, "Osmotic Swelling to Exfoliation. Exceptionally High Degrees of Hydration of a Layered Titanate," *J. Am. Chem. Soc.*, vol. 120, no. 19, pp. 4682–4689, May 1998, doi: 10.1021/ja974262l.

[92] D. Mani *et al.*, "A rutile TiO2 nanobundle as a precursor of an efficient visible-light photocatalyst embedded with Fe2O3," *Inorg. Chem. Front.*, vol. 8, no. 19, pp. 4423-4430, 2021, doi: 10.1039/D1QI00565K.

[93] M. Esmat *et al.*, "Conversion of a 2D lepidocrocite-type layered titanate into Its 1D nanowire form with enhancement of cation exchange and photocatalytic

performance," *Inorg. Chem.*, vol. 58, no. 12, pp. 7989–7996, 2019, doi: 10.1021/acs.inorgchem.9b00722.

[94] P. Wen, Y. Ishikawa, H. Itoh, and Q. Feng, "Topotactic transformation reaction from Layered titanate nanosheets into anatase nanocrystals," *J. Phys. Chem. C*, vol. 113, no. 47, pp. 20275–20280, 2009, doi: 10.1021/jp908181e.

[95] N. Miyamoto, K. Kuroda, and M. Ogawa, "Exfoliation and film preparation of a layered titanate, Na2Ti3O7, and intercalation of pseudoisocyanine dye," *J. Mater. Chem.*, vol. 14, no. 2, pp. 165-170, 2004, doi: 10.1039/B308800F.

[96] B. Singh *et al.*, "Single-Atom (Iron-Based) Catalysts: Synthesis and Applications," *Chem. Rev.*, vol. 121, no. 21, pp. 13620–13697, Nov. 2021, doi: 10.1021/acs.chemrev.1c00158.

[97] M. B. Gawande, K. Ariga, and Y. Yamauchi, "Single-Atom Catalysts," *Small*, vol. 17, no. 16, p. 2101584, 2021, doi: 10.1002/smll.202101584.

[98] E. Cui *et al.*, "An advanced plasmonic photocatalyst containing silver(0) single atoms for selective borylation of aryl iodides," *Appl. Catal. B Environ.*, vol. 299, p. 120674, 2021, doi: 10.1016/j.apcatb.2021.120674.

[99] J. Liu, Y. Zou, D. Cruz, A. Savateev, M. Antonietti, and G. Vilé, "Ligand–Metal Charge Transfer Induced via Adjustment of Textural Properties Controls the Performance of Single-Atom Catalysts during Photocatalytic Degradation," *ACS Appl. Mater. Interfaces*, vol. 13, no. 22, pp. 25858–25867, 2021, doi: 10.1021/acsami.1c02243.

[100] V. Ruta, A. Sivo, L. Bonetti, M. A. Bajada, and G. Vilé, "Structural Effects of Metal Single-Atom Catalysts for Enhanced Photocatalytic Degradation of Gemfibrozil," *ACS Appl. Nano Mater.*, vol. 5, no. 10, pp. 14520–14528, 2022, doi: 10.1021/acsanm.2c02859.

[101] T. Sasaki, S. Nakano, S. Yamauchi, and M. Watanabe, "Fabrication of titanium dioxide thin flakes and their porous aggregate," *Chem. Mater.*, vol. 9, no. 2, pp. 602–608, 1997, doi: 10.1021/cm9604322.

[102] Y. Su, M. L. Balmer, and B. C. Bunker, "Raman Spectroscopic Studies of Silicotitanates," *J. Phys. Chem. B*, vol. 104, no. 34, pp. 8160–8169, Aug. 2000, doi: 10.1021/jp0018807.

[103] R. Godin, Y. Wang, M. A. Zwijnenburg, J. Tang, and J. R. Durrant, "Time-resolved spectroscopic investigation of charge trapping in carbon nitrides photocatalysts for hydrogen generation," *J. Am. Chem. Soc.*, vol. 139, no. 14, pp. 5216–5224, 2017, doi: 10.1021/jacs.7b01547.

[104] C. Zhang *et al.*, "Sn2+-doped double-shelled TiO2 Hollow nanospheres with minimal Pt content for significantly enhanced solar H2 production," *ACS Sustain. Chem. Eng.*, vol. 6, no. 5, pp. 7128–7137, 2018, doi: 10.1021/acssuschemeng.8b01122.

[105] H. Zhu *et al.*, "Catalysts Prepared by a Dry Mixing Method for Oxidative Dehydrogenation of Ethane," *ACS Catal.*, vol. 6, no. 5, pp. 2852–2866, 2016, doi: 10.1021/acscatal.6b00044.

[106] F. Dong, "Flower-like hydrogen titanate nanosheets: preparation, characterization and their photocatalytic hydrogen production performance in the presence of Pt cocatalyst," *RSC Adv.*, 2020.

[107] M. Nagyházi, G. Turczel, P. T. Anastas, and R. Tuba, "Highly efficient ammonia borane hydrolytic dehydrogenation in neat water using phase-labeled CAAC-Ru catalysts," *ACS Sustain. Chem. Eng.*, vol. 8, no. 43, pp. 16097–16103, 2020, doi: 10.1021/acssuschemeng.0c06696.

[108] A. Naldoni *et al.*, “Photocatalysis with reduced TiO2: from black TiO2 to cocatalyst-free hydrogen production,” *ACS Catal.*, vol. 9, no. 1, pp. 345–364, 2019, doi: 10.1021/acscatal.8b04068.
[109] U. Sanyal and B. R. Jagirdar, “Metal and alloy nanoparticles by amine-borane reduction of metal salts by solid-phase synthesis: atom economy and green process,” *Inorg. Chem.*, vol. 51, no. 23, pp. 13023–13033, 2012, doi: 10.1021/ic3021436.
[110] L. J. Minggu, W. R. Wan Daud, and M. B. Kassim, “An overview of photocells and photoreactors for photoelectrochemical water splitting,” *Int. J. Hydrog. Energy*, vol. 35, no. 11, pp. 5233–5244, Jun. 2010, doi: 10.1016/j.ijhydene.2010.02.133.
[111] T. A. Pham, Y. Ping, and G. Galli, “Modelling heterogeneous interfaces for solar water splitting,” *Nat. Mater.*, vol. 16, no. 4, Art. no. 4, Apr. 2017, doi: 10.1038/nmat4803.
[112] J. Ran, J. Zhang, J. Yu, M. Jaroniec, and S. Zhang Qiao, “Earth-abundant cocatalysts for semiconductor-based photocatalytic water splitting,” *Chem. Soc. Rev.*, vol. 43, no. 22, pp. 7787–7812, 2014, doi: 10.1039/C3CS60425J.
[113] J. Jian and J. Sun, “A Review of Recent Progress on Silicon Carbide for Photoelectrochemical Water Splitting,” *Sol. RRL*, vol. 4, no. 7, p. 2000111, 2020, doi: 10.1002/solr.202000111.
[114] C.-F. Fu, X. Wu, and J. Yang, “Material Design for Photocatalytic Water Splitting from a Theoretical Perspective,” *Adv. Mater.*, vol. 30, no. 48, p. 1802106, 2018, doi: 10.1002/adma.201802106.
[115] G. Wang *et al.*, “Hydrogen-Treated TiO2 Nanowire Arrays for Photoelectrochemical Water Splitting,” *Nano Lett.*, vol. 11, no. 7, pp. 3026–3033, Jul. 2011, doi: 10.1021/nl201766h.
[116] S. Ivanova *et al.*, “Synthesis and application of layered titanates in the photocatalytic degradation of phenol,” *Appl. Catal. B Environ.*, vol. 163, pp. 23–29, Feb. 2015, doi: 10.1016/j.apcatb.2014.07.048.
[117] T. Guo, L. Wang, D. G. Evans, and W. Yang, “Synthesis and Photocatalytic Properties of a Polyaniline-Intercalated Layered Protonic Titanate Nanocomposite with a p−n Heterojunction Structure,” *J. Phys. Chem. C*, vol. 114, no. 11, pp. 4765–4772, Mar. 2010, doi: 10.1021/jp9055413.
[118] “Preparation, characterization, and photocatalytic study of solvothermally grown CTAB-capped Bi2WO6 photocatalyst toward photodegradation of Rhodamine B dye,” *Opt. Mater.*, vol. 117, p. 111183, Jul. 2021, doi: 10.1016/j.optmat.2021.111183.
[119] Y. Ide and M. Ogawa, “Interlayer Modification of a Layered Titanate with Two Kinds of Organic Functional Units for Molecule-Specific Adsorption,” *Angew. Chem. Int. Ed.*, vol. 46, no. 44, pp. 8449–8451, 2007, doi: 10.1002/anie.200702360.
[120] B. Yang, A. G. Tamirat, D. Bin, Y. Yao, H. Lu, and Y. Xia, “Regulating Intercalation of Layered Compounds for Electrochemical Energy Storage and Electrocatalysis,” *Adv. Funct. Mater.*, vol. 31, no. 52, p. 2104543, 2021, doi: 10.1002/adfm.202104543.
[121] Z.-J. Chen *et al.*, “Preparation and characterization of mesoporous TiO2-pillared titanate photocatalyst,” *J. Porous Mater.*, vol. 18, no. 2, pp. 185–193, Apr. 2011, doi: 10.1007/s10934-010-9369-1.

[122] F. Ogawa, T. Ban, and Y. Ohya, “Preparation of lamellar hybrid inorganic–organic films of layered titanate and cationic or anionic surfactants,” *Thin Solid Films*, vol. 516, no. 15, pp. 4863–4867, Jun. 2008, doi: 10.1016/j.tsf.2007.09.007.
[123] J. Goworek, A. Kierys, W. Gac, A. Borówka, and R. Kusak, “Thermal degradation of CTAB in as-synthesized MCM-41,” *J. Therm. Anal. Calorim.*, vol. 96, no. 2, pp. 375–382, May 2009, doi: 10.1007/s10973-008-9055-6.
[124] G. A. Marking, J. A. Hanko, and M. G. Kanatzidis, “New Quaternary Thiostannates and Thiogermanates A2Hg3M2S8 (A = Cs, Rb; M = Sn, Ge) through Molten A2Sx. Reversible Glass Formation in Cs2Hg3M2S8,” *Chem. Mater.*, vol. 10, no. 4, pp. 1191–1199, Apr. 1998, doi: 10.1021/cm970804m.
[125] K. H. Rahman and A. K. Kar, “Influence of catalyst loading on photocatalytic degradation efficiency of CTAB-assisted TiO2 photocatalyst towards methylene blue dye solution,” *Bull. Mater. Sci.*, vol. 45, no. 1, p. 18, Jan. 2022, doi: 10.1007/s12034-021-02600-5.
[126] H. Li *et al.*, “Rationally designed 2D/2D highly reduced graphene oxide modified wide band gap semiconductor photocatalysts for hydrogen production,” *Surf. Sci.*, vol. 734, p. 122316, Aug. 2023, doi: 10.1016/j.susc.2023.122316.
[127] Z. Li, S. Wang, J. Wu, and W. Zhou, “Recent progress in defective TiO2 photocatalysts for energy and environmental applications,” *Renew. Sustain. Energy Rev.*, vol. 156, p. 111980, Mar. 2022, doi: 10.1016/j.rser.2021.111980.
[128] D. Gong *et al.*, “Silver decorated titanate/titania nanostructures for efficient solar driven photocatalysis,” *J. Solid State Chem.*, vol. 189, pp. 117–122, May 2012, doi: 10.1016/j.jssc.2011.11.036.
[129] H. Park, T. Goto, S. Cho, H. Nishida, and T. Sekino, “Enhancing Visible Light Absorption of Yellow-Colored Peroxo-Titanate Nanotubes Prepared Using Peroxo Titanium Complex Ions,” *ACS Omega*, vol. 5, no. 34, pp. 21753–21761, Sep. 2020, doi: 10.1021/acsomega.0c02734.
[130] T. Maluangnont *et al.*, “An Unusually Acidic and Thermally Stable Cesium Titanate CsxTi2–yMyO4 (x = 0.67 or 0.70; M = vacancy or Zn),” *Inorg. Chem.*, vol. 58, no. 10, pp. 6885–6892, May 2019, doi: 10.1021/acs.inorgchem.9b00369.
[131] T. Maluangnont *et al.*, “Electrochemical and electrical characteristics of ball milled Cs 2 Ti 6 O 13 modified by the surface-to-bulk migration of hydroxyl groups,” *Dalton Trans.*, 2023, doi: 10.1039/D3DT01437A.
[132] L. Qian, Z.-L. Du, S.-Y. Yang, and Z.-S. Jin, “Raman study of titania nanotube by soft chemical process,” *J. Mol. Struct.*, vol. 749, no. 1, pp. 103–107, Jul. 2005, doi: 10.1016/j.molstruc.2005.04.002.
[133] Y. Li, S. Ji, Y. Gao, H. Luo, and M. Kanehira, “Core-shell VO2@TiO2 nanorods that combine thermochromic and photocatalytic properties for application as energy-saving smart coatings,” *Sci. Rep.*, vol. 3, no. 1, Art. no. 1, Apr. 2013, doi: 10.1038/srep01370.
[134] J. Surmacki, P. Wroński, M. Szadkowska-Nicze, and H. Abramczyk, “Raman spectroscopy of visible-light photocatalyst – Nitrogen-doped titanium dioxide generated by irradiation with electron beam,” *Chem. Phys. Lett.*, vol. 566, pp. 54–59, Apr. 2013, doi: 10.1016/j.cplett.2013.02.066.
[135] K.-R. Zhu, M.-S. Zhang, Q. Chen, and Z. Yin, “Size and phonon-confinement effects on low-frequency Raman mode of anatase TiO2 nanocrystal,” *Phys. Lett. A*, vol. 340, no. 1, pp. 220–227, Jun. 2005, doi: 10.1016/j.physleta.2005.04.008.

[136] A. Gajović, I. Friščić, M. Plodinec, and D. Iveković, “High temperature Raman spectroscopy of titanate nanotubes,” *J. Mol. Struct.*, vol. 924–926, pp. 183–191, Apr. 2009, doi: 10.1016/j.molstruc.2008.12.072.
[137] G. Tian, H. Fu, L. Jing, and C. Tian, “Synthesis and photocatalytic activity of stable nanocrystalline TiO2 with high crystallinity and large surface area,” *J. Hazard. Mater.*, vol. 161, no. 2, pp. 1122–1130, Jan. 2009, doi: 10.1016/j.jhazmat.2008.04.065.
[138] P. Gonzalez Rodriguez, H. Yuan, K. J. H. van den Nieuwenhuizen, W. Lette, D. J. Schipper, and J. E. ten Elshof, “Hybrid n-Alkylamine Intercalated Layered Titanates for Solid Lubrication,” *ACS Appl. Mater. Interfaces*, vol. 8, no. 42, pp. 28926–28934, Oct. 2016, doi: 10.1021/acsami.6b12716.
[139] M. Piao *et al.*, “Critical Role of the Chemical Environment of Interlayer Na Sites: An Effective Way To Improve the Na Ion Electrode Activity of Layered Titanate,” *ACS Appl. Mater. Interfaces*, vol. 10, no. 39, pp. 33112–33123, Oct. 2018, doi: 10.1021/acsami.8b07031.
[140] Mohd. A. Siddiqui, V. S. Chandel, M. Shariq, and A. Azam, “FTIR and dielectric studies of nickel doped potassium hexa-titanate (K2Ti6O13) fine ceramics,” *J. Mater. Sci. Mater. Electron.*, vol. 24, no. 12, pp. 4725–4731, Dec. 2013, doi: 10.1007/s10854-013-1466-x.
[141] W. Geng *et al.*, “Preparation of layered titanate nanosheets and the application for Cs+ adsorption from wastewater, effluents and a simulated brine,” *Hydrometallurgy*, vol. 216, p. 105999, Feb. 2023, doi: 10.1016/j.hydromet.2022.105999.
[142] R. A. Campbell, S. R. W. Parker, J. P. R. Day, and C. D. Bain, “External Reflection FTIR Spectroscopy of the Cationic Surfactant Hexadecyltrimethylammonium Bromide (CTAB) on an Overflowing Cylinder,” *Langmuir*, vol. 20, no. 20, pp. 8740–8753, Sep. 2004, doi: 10.1021/la048680x.
[143] L. Huang, X. Chen, and Q. Li, “Synthesis of microporous molecular sieves bysurfactant decomposition,” *J. Mater. Chem.*, vol. 11, no. 2, pp. 610–615, Jan. 2001, doi: 10.1039/B005770N.
[144] X. Xi, A. Pizzi, and L. Delmotte, “Isocyanate-Free Polyurethane Coatings and Adhesives from Mono- and Di-Saccharides,” *Polymers*, vol. 10, no. 4, Art. no. 4, Apr. 2018, doi: 10.3390/polym10040402.
[145] H. N. Kim, T. W. Kim, I. Y. Kim, and S.-J. Hwang, “Cocatalyst-Free Photocatalysts for Efficient Visible-Light-Induced H2 Production: Porous Assemblies of CdS Quantum Dots and Layered Titanate Nanosheets,” *Adv. Funct. Mater.*, vol. 21, no. 16, pp. 3111–3118, 2011, doi: 10.1002/adfm.201100453.
[146] B. Bharti, S. Kumar, H.-N. Lee, and R. Kumar, “Formation of oxygen vacancies and Ti3+ state in TiO2 thin film and enhanced optical properties by air plasma treatment,” *Sci. Rep.*, vol. 6, no. 1, Art. no. 1, Aug. 2016, doi: 10.1038/srep32355.
[147] N. Zhong, H. Shima, and H. Akinaga, “Mechanism of the performance improvement of TiO2-x-based field-effect transistor using SiO2 as gate insulator,” *AIP Adv.*, vol. 1, no. 3, p. 032167, Sep. 2011, doi: 10.1063/1.3646525.
[148] K. Artyushkova, “Misconceptions in interpretation of nitrogen chemistry from x-ray photoelectron spectra,” *J. Vac. Sci. Technol. A*, vol. 38, no. 3, p. 031002, Mar. 2020, doi: 10.1116/1.5135923.
[149] M. Ayiania, M. Smith, A. J. R. Hensley, L. Scudiero, J.-S. McEwen, and M. Garcia-Perez, “Deconvoluting the XPS spectra for nitrogen-doped chars: An

analysis from first principles," *Carbon*, vol. 162, pp. 528–544, Jun. 2020, doi: 10.1016/j.carbon.2020.02.065.

[150] R. Hao, G. Wang, C. Jiang, H. Tang, and Q. Xu, "In situ hydrothermal synthesis of g-C3N4/TiO2 heterojunction photocatalysts with high specific surface area for Rhodamine B degradation," *Appl. Surf. Sci.*, vol. 411, pp. 400–410, Jul. 2017, doi: 10.1016/j.apsusc.2017.03.197.

[151] S. Chabri, A. Dhara, B. Show, D. Adak, A. Sinha, and N. Mukherjee, "Mesoporous CuO–ZnO p–n heterojunction based nanocomposites with high specific surface area for enhanced photocatalysis and electrochemical sensing," *Catal. Sci. Technol.*, vol. 6, no. 9, pp. 3238–3252, May 2016, doi: 10.1039/C5CY01573A.

Chapter 7:
APPENDIX

7.1 Appendix A: Supporting Information for Chapter 3.

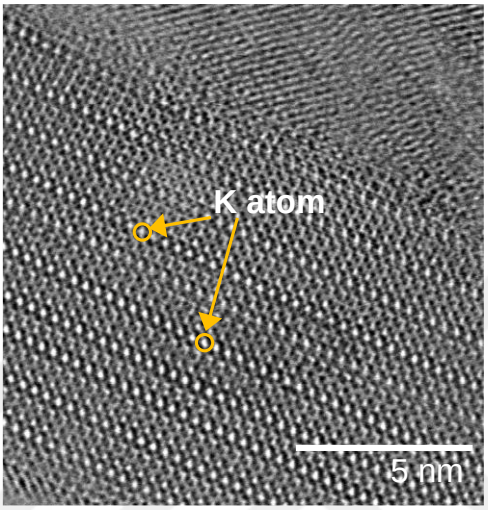

Figure A1.1 HRTEM image of K^+-unexchanged layered titanate (KTLO).

Preparation of Sn^{4+} loaded exf-HTO

Sn^{4+}-loaded exf-HTO was prepared by deposition of Sn^{4+} from 20 ppm of SnI_4 solution on exf-HTO. 10 mg of exf-HTO was dispersed in 20 mL of 20 ppm SnI_4 solution in a test tube, and the mixture was stirred at 400 ppm for three hours. After the solution was centrifuged at 3000 rpm for 20 minutes and washed with distilled water, it was put in a vacuum oven for 24 hours to dry at room temperature.

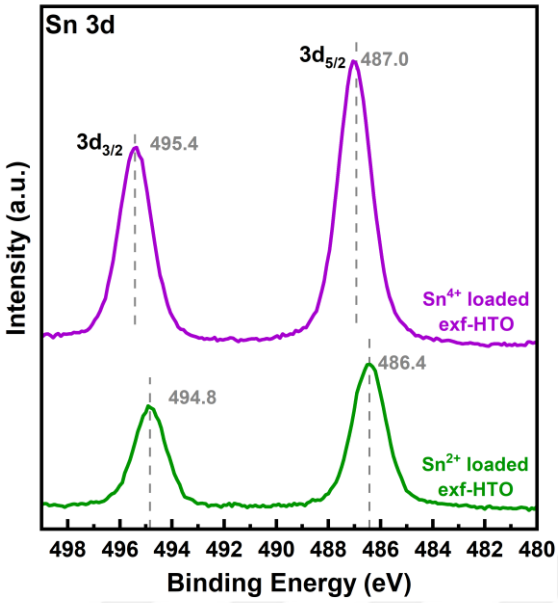

Figure A1.2 Sn 3d XPS spectra of Sn^{4+} and Sn^{2+} loaded on exf-HTO.

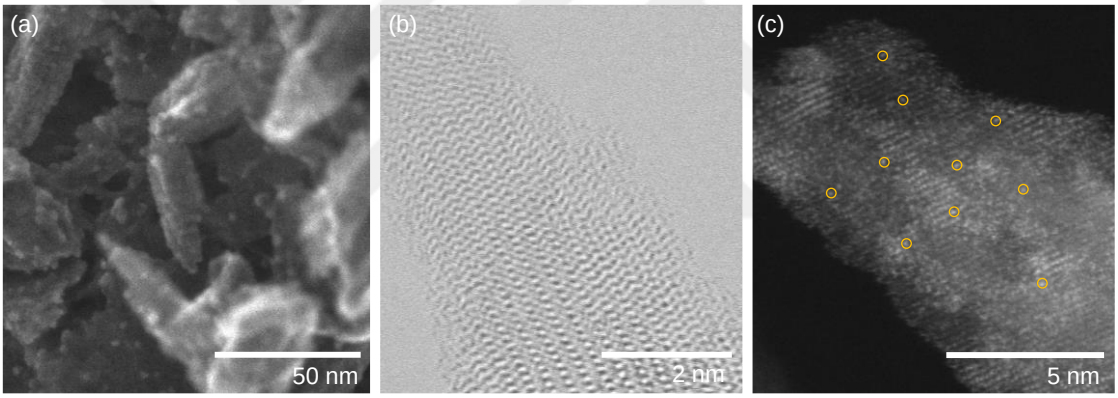

Figure A1.3 SEM (a), TEM (b), and HAADF-STEM (c) of Sn loaded exfoliated HTO (Sn/exf-HTO) with 50 ppm of Sn salt solution.

Photocatalytic activity tests at specific wavelengths

To make the photocatalytic H_2 evolution test by illuminating the light at specific wavelengths (320, 340, 360, and 380 nm), a Xe lamp (300 W) was used with a monochromator. The same procedure was followed to prepare the sample in a Pyrex test tube. After 5 mg of Sn/exf-HTO was dispersed in 4.5 mL distilled water and purged with N_2, 0.5 mL of 40mM AB was added and put under illumination for 30 minutes. A new sample was prepared at the same conditions for each measurement of different wavelengths. The hydrogen amount was quantified with the gas chromatograph by taking injections.

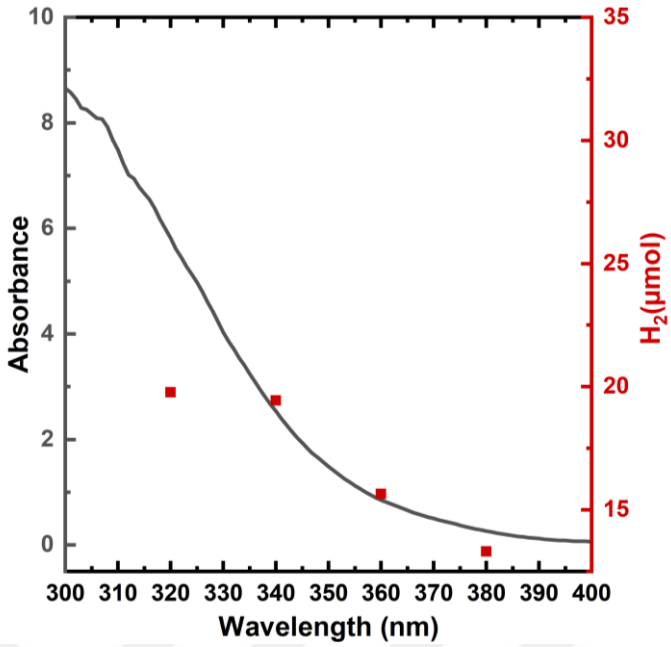

Figure A1.4 Hydrogen evolution from AB dehydrogenation with the absorbance at specific wavelengths.

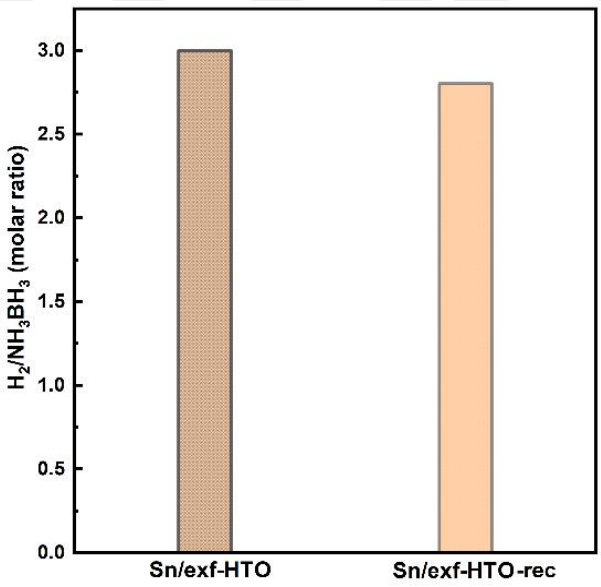

Figure A1.5 Photocatalytic activity of Sn-loaded exfoliated HTO and the recovered Sn/exf-HTO in ammonia borane dehydrogenation.

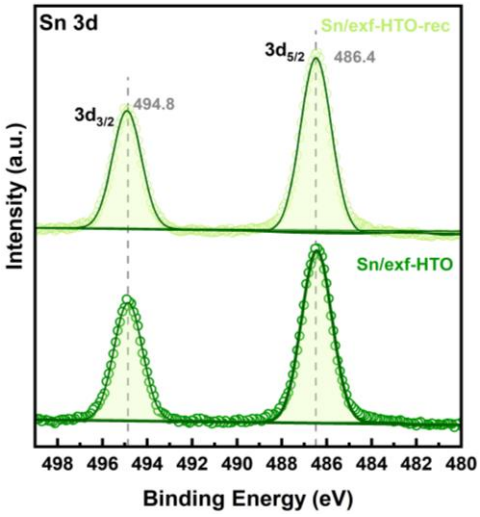

Figure A1.6 Sn 3d XPS spectra of Sn/exf-HTO and recovered Sn/exf-HTO-rec.

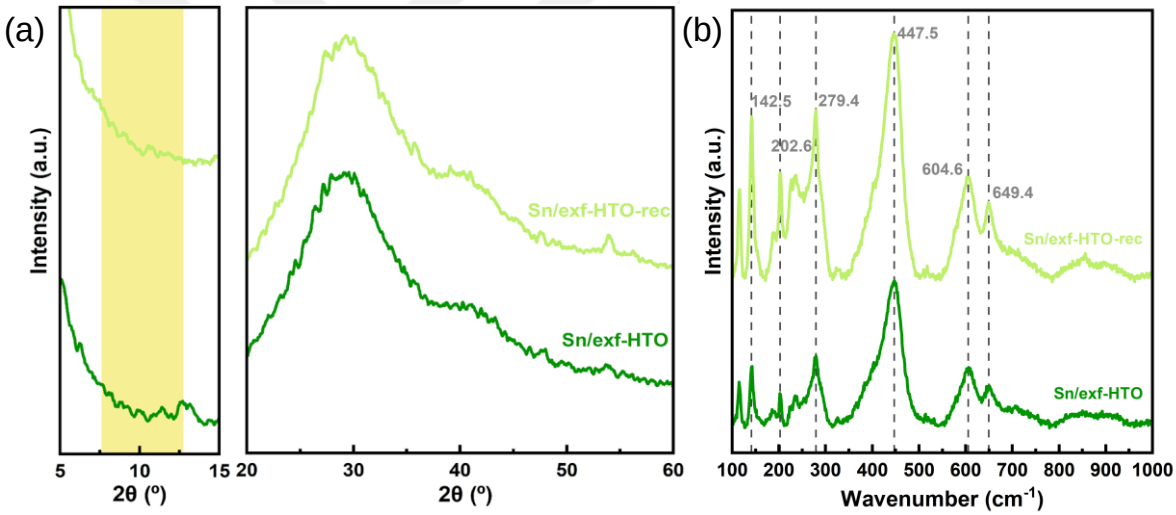

Figure A1.7 The XRD patterns (a) and Raman spectra (b) of Sn/exf-HTO and the recovered Sn/exf-HTO-rec.